Mixed proton electron conducting oxides as hydrogen transport membranes in electrochemical potential gradients.

Einar Vøllestad

Dissertation for the degree of Philosophiae Doctor

Department of Chemistry
Faculty of Mathematics and Natural Sciences

UNIVERSITY OF OSLO

November 2013

© Einar Vøllestad, 2014

Series of dissertations submitted to the
Faculty of Mathematics and Natural Sciences, University of Oslo
No. 1449

ISSN 1501-7710

All rights reserved. No part of this publication may be
reproduced or transmitted, in any form or by any means, without permission.

Cover: Inger Sandved Anfinsen.
Printed in Norway: AIT Oslo AS.

Produced in co-operation with Akademika Publishing.
The thesis is produced by Akademika Publishing merely in connection with the
thesis defence. Kindly direct all inquiries regarding the thesis to the copyright
holder or the unit which grants the doctorate.

Preface

This dissertation represents part of the required work for the degree of Philosophiae Doctor (PhD) at the Department of Chemistry, Faculty of Mathematics and Natural Science, University of Oslo. The doctoral scholarship has been funded by the BIGCCS Centre, performed under the Norwegian research program Centres for Environment-friendly Energy Research (FME). The work was carried out the group of Solid State Electrochemistry during the period from September 2010 to November 2013 under the supervision of Assoc. Professor Reidar Haugsrud and Professor Truls Norby.

I would like to thank my main supervisor, Reidar Haugsrud, for stimulating discussions, helpful advice, and most of all his positive and encouraging spirit which has been extremely helpful in periods where things were going slowly. I am also grateful for the constructive and inspiring discussions with Truls Norby, as his quest for asking and answering new questions helped bring this work further. I would also like to thank my fellow colleagues for all the help you provided and for making our lab an enjoyable place to work – also socially. A special mention goes to my fellow BIGCCS partner, Camilla Vigen, who has contributed in countless way to help in my daily struggles. I would like to acknowledge Prof. Robert J. Kee for his guidance and assistance during my stay at the Colorado School of Mines.

I am very grateful to my family for being supportive and understanding throughout this process, and providing constructive and helpful advice when needed. Finally, I would like to thank my friends for reminding me constantly that there is a life outside of the lab as well.

Oslo, November 2013

Einar Vøllestad

Summary

Mixed proton electron conducting oxides are candidate materials for future energy technologies such as hydrogen separation, water electrolysis, and intermediate temperature fuel cells. The functional performance of proton conducting membranes is, in large, determined by the transport properties of the mobile protonic and electronic species in electrochemical gradients. Transport of cations, although much slower, often determines the lifetime of functional oxides, as it can result in kinetic demixing or decomposition, and morphological instabilities on the membrane surfaces. Fundamental understanding of the processes governing transport in electrochemical potential gradients is therefore of great importance for proton conducting oxides. The mixed proton electron conductor lanthanum tungsten oxide, $La_{28-x}W_{4+x}O_{54+\delta}$ (LWO), is chosen as a model system for the experimental studies in this work. Investigations of film deposition, hydrogen permeation, cation diffusion and kinetic stability are all implemented to evaluate the potential of LWO-based materials as hydrogen transport membranes. Finally, a partial differential model for transport of mobile defects in mixed conductors is developed and compared to conventional integral formulations.

Films of lanthanum tungsten oxide are successfully deposited on metal and oxide substrates by pulsed laser deposition (PLD). The films crystallize in the defective fluorite LWO structure with slightly larger cell parameter, and a proton conductivity resembling the bulk properties of LWO. The hydrogen permeation characteristics of 30 % Mo-substituted lanthanum tungsten oxide, $La_{27}Mo_{1.5}W_{3.5}O_{55.5}$ (LWMo), are investigated as a function of temperature, hydrogen partial pressure gradient, and water vapour pressure in the sweep gas. Transport of hydrogen by means of ambipolar proton-electron conductivity and – with wet sweep gas – water dissociation contribute to the measured hydrogen content in the permeate. At 700 °C under dry sweep conditions, the H_2 permeability in LWMo is 6×10^{-4} $mL \cdot min^{-1} \cdot cm^{-1}$, significantly higher than state-of-the-art acceptor doped $SrCeO_3$-based membranes. Proton conductivity is identified as rate limiting for ambipolar bulk transport across the membrane, even at temperatures as low as 600 °C, contrary to most mixed proton electron conducting oxides. On these bases it is evident that Mo-substitution is a successful doping strategy to increase the n-type conductivity – and H_2 permeability – compared to nominally undoped lanthanum tungsten oxide.

The cation diffusion properties of LWO are investigated by means of interdiffusion and chemical tracer diffusion studies in the temperature range 1000-1350 °C in both oxidizing and reducing atmospheres. The bulk diffusivities for La and W site diffusion are similar within the experimental error at all temperatures investigated. Considering the large difference in ionic radii and valence state of the two cations, the similar diffusivities indicate that both species migrate via the same mechanism. In LWO, 1/5 of the W atoms reside on the La2 sublattice, and a diffusion mechanism involving vacant La2 sites is therefore proposed.

The La site cations also exhibit enhanced diffusion along the grain boundaries of LWO, 10^3-10^4 times faster than bulk diffusion. In contrast, there are no indications of W site transport along the grain boundaries, which we attribute to a depletion of W^{6+} near the positively charged grain boundary core. Consequently, one may expect accumulation of La on the high p_{O_2}-side of LWO based membranes exposed to an electrochemical potential gradient and elevated temperature. However, the estimated time to reach steady state demixing at 900 °C is far longer than the proposed lifetime of components in hydrogen based technologies. Still, degradation may occur during the transient demixing or due to decomposition and secondary phase formation on the membrane surfaces.

The characterizations of LWO reveal that the lanthanum tungsten oxides comprise an interesting and promising class of materials with tuneable transport properties for various applications and relatively slow cation diffusivities. One may envision that continued studies on the optimal cation ratios for operation in reducing conditions and high temperatures may lead to further improvements in both the performance and the stability of the membrane, and further studies on these topics are called upon.

Development of robust and complete mathematical models that can predict defect and gas phase fluxes in oxides with three or more mobile species is necessary when moving hydrogen technologies from the laboratory bench towards commercial realization. A partial differential model based on Nernst-Planck-Poisson formulations is developed to describe defect profiles in – and transport phenomena through – a mixed conductor exposed to an electrochemical potential gradient. The model is compared to a conventional integral formulation for a model system in which two or three mobile species are participating in charge transport. The models are in good agreement when the membrane is exposed to only one gas phase gradient; however, the fluxes depart once the situation becomes more complex. The latter is attributed to inherent assumptions in the integral model that allows for analytic solutions to the integrals.

Altogether, this work highlights and investigates many of the most important aspects of mixed proton electron conducting oxides in electrochemical gradients. The system is more complex than for mixed oxide ion electron conductors due to the added proton species into the thermodynamic situation. As a consequence, analysis of experimental data is a challenge unless the defect chemistry or transport parameters are individually determined.

The state of the art hydrogen permeabilities for single phase proton conducting membranes are still far below Pd-based metallic alloys. Still, the ceramic membranes may offer advantages in terms of chemical and thermal stability that facilitates integration in high temperature processes. A promising route for further improvement is the development of ceramic-ceramic composites if the challenges related to mechanical and chemical compatibility and cation interdiffusion are addressed.

Table of contents

Preface i

Summary iii

1. Introduction 1
    - 1.1. Motivation 1
    - 1.2. Hydrogen transport membranes 3
    - 1.3. Proton conducting oxides – Current status and remaining challenges 10
    - 1.4. Aim and contents of this thesis 12
2. Transport in ionic solids 15
    - 2.1. Defects in oxides 15
    - 2.2. Defect chemistry of lanthanum tungsten oxide 18
    - 2.3. Diffusion theory 19
        - 2.3.1 Random diffusion 19
        - 2.3.2 Vacancy mechanism 21
        - 2.3.3 Interstitial mechanism 22
        - 2.3.4 Proton diffusion 23
    - 2.4. Macroscopic diffusion 25
    - 2.5. Phenomenological diffusion coefficients 27
        - 2.5.1 Self-diffusion coefficient 27
        - 2.5.2 Tracer diffusion 28
        - 2.5.3 Chemical diffusion 29
        - 2.5.4 Chemical inter-diffusion 31
3. Oxides in electrochemical potential gradients 33
    - 3.1. Binary oxides exposed to an oxygen potential gradient 33
    - 3.2. Kinetic demixing 35
    - 3.3. Kinetic decomposition 39

3.4. Morphological instability....42

3.5. Proton conducting oxides exposed to a hydrogen potential gradient....43

4. Methodology....47

4.1. Pulsed Laser Deposition....47

4.2. Time-of-Flight Secondary Ion Mass Spectroscopy....50

4.3. Electron MicroProbe Analysis....51

4.4. Hydrogen permeation measurements....52

4.5. Cation diffusion measurements....54

4.5.1 Inter-diffusion....55

4.5.2 Chemical tracer diffusion....56

4.6. Mathematical treatment of diffusion profiles....57

4.6.1 Inter-diffusion with constant diffusivity....58

4.6.2 Chemical tracer diffusion with constant diffusivity....59

4.6.3 Inter-diffusion with composition-dependent diffusivity....61

4.6.4 Grain boundary diffusion....62

5. Manuscripts....65

6. Discussion....149

6.1. LnWO-system as a hydrogen transport membrane....149

6.1.1 Bulk transport of majority charge carriers....149

6.1.2 Surface kinetics....153

6.1.3 Cation diffusion and kinetic stability....154

6.2. Mathematical modelling of mixed ionic-electronic conductors under chemical potential gradients....157

6.3. Functional dependencies and interpretation of hydrogen permeation measurements....160

6.4. Proton conducting membranes – applicability and challenges....169

7. Conclusions....177

References for Chapters 1-4 and 6....181

Appendix 189

1. Introduction

1.1. Motivation

The world is in a state of unprecedented growth in population and welfare causing an ever increasing energy demand. Considering the limited fossil fuel reserves and the potential climate consequences of continued CO_2 emissions, it seems clear that a transition to a new energy system based on a clean energy vector is essential. In order to meet these immediate issues, all measures must be made from a perspective of sustainable development, as defined by the Brundtland commission presented to the United Nations in 1987 as a "*development that meets the needs of the present without compromising the ability of future generations to meet their own needs*" [1]. Thus, it is essential to develop clean and durable energy technologies that do not suffer from the disadvantages of fossil fuels in terms of greenhouse gas emissions and depletion of resources, but still guarantee a sufficient and cost-efficient supply of energy. Based on present technologies, it is extremely challenging to meet the rising energy demand in the immediate future without utilizing fossil fuels. Parallel development of short term technologies that minimize climate gas emission and increase the carbon efficiency from fossil fuels and long term development of technologies based on entirely renewable and clean energy sources is therefore essential to achieve a clean energy transition.

Wind and solar power are promising renewable energy technologies which are rapidly increasing in efficiency and decreasing in cost. However, the intermittent nature of wind and solar energy remains a challenge, and development of technologies for conversion and storage of the surplus energy during peak hours is vital for obtaining high energy efficiencies. Electrolyser cells which can convert electricity and water (or steam) into hydrogen gas is a promising technology, as hydrogen can be stored in high-pressure tanks and re-converted to electricity in fuel cells at low output hours, or used for transportation purposes such as fuel cell driven cars. There are also large activities on developing technologies that can produce hydrogen directly from water and sunlight, without the intermediate conversion of solar to electric energy, thus potentially minimizing the energy losses and reducing system complexity and cost.

On a short-term basis, the transition towards a cleaner utilization of fossil fuels is also based on hydrogen technologies. Hydrogen gas may be extracted from natural gas via steam-reforming and water gas shift reactions, which can be coupled with continuous hydrogen removal through a hydrogen transport membrane. This process enables hydrogen production from natural gas with simultaneous CO_2 capture and storage. In a similar process, hydrogen transport membranes may be incorporated in catalytic membrane reactors for conversion of so-called stranded and associated natural gas[1] into liquid fuels to shift the thermodynamics towards higher product yields, increasing the utilization of the available energy resources which are currently wasted.

Materials science will play an indispensable role in developing environment friendly cost-efficient energy technologies. One class of materials which may prove essential in many stages of development is proton conducting oxides. Solid oxide fuel cells (SOFCs), where the electrolyte is exclusively proton conducting – named proton ceramic fuel cells (PCFCs) – are interesting alternatives, also to today’s polymer based fuel cells. PCFCs can operate at intermediate temperatures, typically 400-700 °C, and have the potential of running on non-purified hydrogen or reformed fossil fuels. Oxides that display both protonic and electronic conductivity may find applications as hydrogen transport membranes with virtually 100% selectivity, and can be used for hydrogen production and natural gas processing. Such oxides typically display lower permeation rates than palladium-based metal alloys, but offer advantages such as lower material cost, higher resistance towards surface poisoning by H_2S and CO and can stand higher operating temperatures. This allows for thermal integration in high temperature processes such as methane reforming. However, there are many remaining challenges in developing the optimal proton conducting oxide in terms of bulk transport, surface kinetics and thermodynamic stability.

---

[1] Associated gas is natural gas that is pumped up together with oil in oil-fields. As this is low in concentration it is not feasible to build up infrastructure that allows storage and transport, and the gas is rather burned on site. This is typically seen by a flame on the top of the oil platforms in the North Sea.

Development of better membrane materials and improved understanding of the fundamental properties governing hydrogen permeation and long term stability lies at the heart of this thesis. Before we turn our attention towards ceramic proton conducting membranes, the reader will be introduced to some general aspects of high temperature hydrogen transport membranes and the different materials classes to provide a deeper understanding of the state of hydrogen membranes technologies.

1.2. Hydrogen transport membranes

Hydrogen transport membranes are physical barriers that selectively allow transport of hydrogen from one gas atmosphere to another, as illustrated in Figure 1.1. The hydrogen may be transported as gaseous hydrogen molecules through mesoporous membranes such as zeolites and porous carbon, dissociated hydrogen through dense metal alloys or protons and electrons through dense mixed protonic electronic conducting ceramics [2].

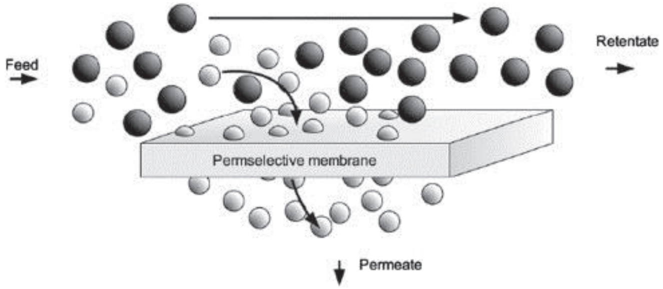

Figure 1.1. Conceptual illustration of a gas separation membrane [2]

Figure 1.2 presents two potential applications for hydrogen transport membranes; combined methane reforming and water gas shift for hydrogen production and CO_2 capture and sequestration (a), and non-oxidative methane de-hydrogenation to produce liquid fuels (b). For methane reforming, hydrogen removal through the hydrogen transport membrane serves two purposes; i) hydrogen extraction shifts the thermodynamics towards higher conversion rates and ii) allows for instant separation of H_2 from the CO_2 such that high purity hydrogen gas is formed in the permeate exhaust. The catalytic membrane reactor (b) implements a hydrogen transport membrane in combination with a catalyst to selectively convert methane to benzene or higher aromatics, which can be further converted to other liquid fuels [3, 4]. Also here, removal of hydrogen shifts the thermodynamics of the endothermic reaction towards higher product yields. By introducing oxygen in the sweep gas, the separated hydrogen is oxidized to form water and maintain energy balance for endothermic de-hydrogenation reaction. In both applications, it is evident that the membrane material must be stable towards CO_2 and impurities typically present in the natural gas mixture, e.g. H_2S. In the non-oxidative methane conversion reaction coking is a critical issue, and the membrane surface should not be catalytically active towards coke formation to obtain higher efficiencies.

In general, hydrogen transport membranes should have the following characteristics:

- high flux
- high selectivity towards hydrogen
- high mechanical and chemical stability
- low cost

Among the candidate materials, dense alloys and ceramic mixed conductors exhibit the highest selectivities, while the highest fluxes are generally achieved for microporous ceramics and palladium-based metal alloys. Dense ceramics have in principle the best stabilities and lifetime predictions. The materials costs for the metallic membranes are higher than for the other alternatives, due to the high cost of palladium. Before we turn our focus towards dense ceramic mixed conducting oxides, the reader will be introduced to the current technological status and remaining challenges for microporous and metallic membranes.

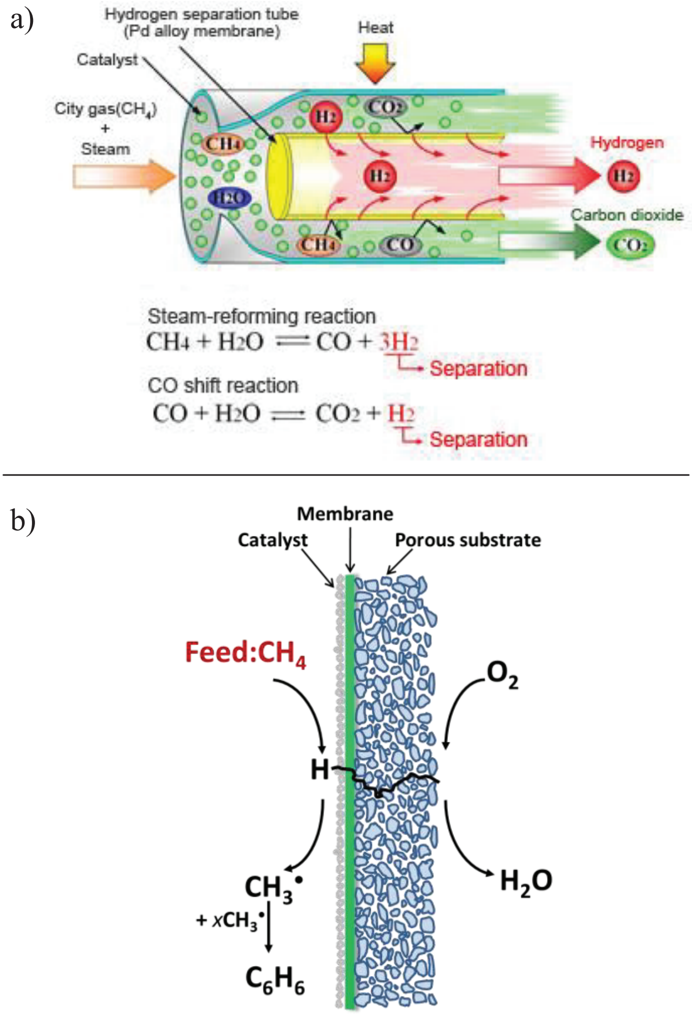
a)
Hydrogen separation tube
(Pd alloy membrane)
Heat
Catalyst
City gas(CH_4)
+
Steam
H_2
CO_2
CH_4
H_2O
CO
Hydrogen
Carbon dioxide
Steam-reforming reaction
$CH_4 + H_2O \rightleftharpoons CO + 3H_2$
Separation
CO shift reaction
$CO + H_2O \rightleftharpoons CO_2 + H_2$
Separation
b)
Membrane
Catalyst
Porous substrate
Feed:CH_4
O_2
H
H_2O
$CH_3^\bullet$
$+ xCH_3^\bullet$
C_6H_6

Figure 1.2 – Schematics of two potential applications for hydrogen transport membranes: (a) Hydrogen production from steam reformed natural gas with coupled CO_2 sequestration, as suggested by Tokyo Gas [5]. (b) Catalytic membrane reactor for non-oxidative methane conversion under development by Protia [6] based on the principle first suggested by Hamakawa *et al*. [7, 8]

Microporous membranes

Microporous materials are defined by the International Union of Pure and Applied Chemistry (IUPAC) as materials with pore sizes smaller than 2 nm [9]. As membranes, these materials essentially function as molecular sieves due to size exclusion, determined by the kinetic diameter of the gas molecules. The efficiency of these membranes is determined by the pore size and distribution relative to the size of the molecules. In the case of pre-combustion hydrogen separation, the membranes must be able to separate hydrogen from a CO_2 containing mixture, which means that the pore size should be in the range of the kinetic diameter of hydrogen (2.89 Å), while still being small enough to limit permeation of CO_2 with a kinetic diameter of 3.3 Å. Consequently, a major challenge is the preparation of defect-free, thin membranes with defined pore structure to enable a sufficiently high separation factor [10]. Among the most important microporous ceramics are porous amorphous carbon and silicates, zeolites and metal-organic frameworks (MOFs).

Porous amorphous carbon has the advantage of a relatively easy, flexible and cheap manufacturing route of thin films (~1 µm) with pore diameters close to the kinetic diameter of hydrogen gas, combined with excellent chemical and thermal stability under reducing conditions [2]. Thus, porous carbon based membranes have been shown to be viable as a membrane for hydrogen separation from refiner gas streams with a fairly high permeability and selectivity [11]. However, they are not considered ideal for membrane reactors due to the complex surface chemistry and the oxidative nature of the carbon surface. Amorphous silica membranes also display high permeability and selectivity, but suffer from hydrothermal degradation and pore closure in the presence of high steam concentrations [2].

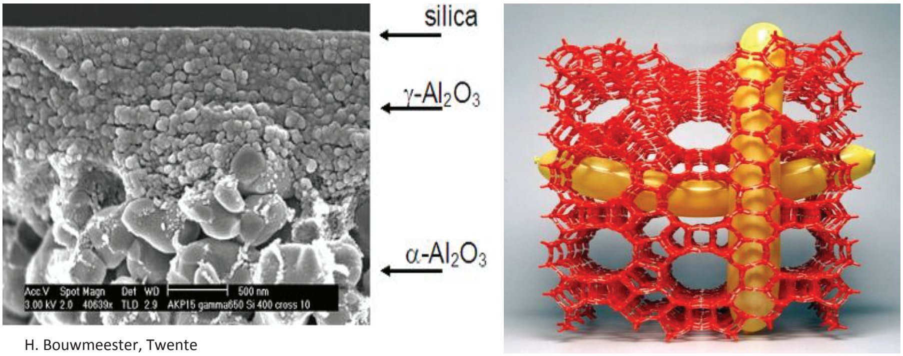
silica
γ-Al2O3
α-Al2O3
Acc.V Spot Magn Det WD 500 nm
3.00 kV 2.0 40639x TLD 2.9 AKP15 gamma650 Si 400 cross 10

H. Bouwmeester, Twente

K. Ståhl, DTU

Figure 1.3. Illustrations of microporous silica (a) and zeolite membranes (b) taken from the websites of University of Twente [12] and DTU [13], respectively.

Among the crystalline porous membranes, zeolites and MOFs have been the subject of most attention as of late. This is due to their ordered and uniform pores with diameters close to molecular dimensions (3-10 Å) [14]. An added benefit from these types of membranes is the tuneable catalytic behaviour of the active functional sites, which could contribute positively in, for instance, a catalytic membrane reactor [10]. Until recently, zeolites were by far the most studied between the two materials, due to the maturity of the research field. However, it seems that MOFs have a greater potential as hydrogen transport membranes due to a higher tolerability towards thermal cycling, a less energy-intensive synthesis procedure, and they are also more flexible and less brittle than their zeolite counterparts [15]. However, there are still major challenges related to fabrication of stable and dense thin films of MOF membranes and the development of materials which can withstand temperatures above 600 °C.

Dense metallic membranes

Dense metal membranes comprise the class of material which is, by far, closest to commercialization as hydrogen transport membranes on a large scale [2, 10]. They are already implemented to some degree in high purity hydrogen production, and massive efforts in both industry and academia are currently focused on making large-scale metallic membranes for hydrogen separation. In these membranes, hydrogen permeation occurs via a solution-diffusion mechanism [16]. In short, hydrogen gas dissociates on the metal surface, dissolves into the bulk structure where it diffuses towards the low hydrogen partial pressure (p_{H_2}) side. Once the hydrogen atoms reach the permeate surface, association and desorption occur, and hydrogen gas molecules can diffuse away from the surface. Surface dissociation and/or association may become rate limiting for hydrogen permeation if the membranes are made sufficiently thin (< 1-2 µm).

Among the many metals tested, Pd-based membranes are the most promising candidates. They show superior permeability, selectivity and stability at intermediate temperatures (400-500 °C). However, pure Pd membranes suffer from some critical challenges, such as hydrogen embrittlement, surface poisoning and high material cost. Pd goes through a phase transition from α- to β-hydride phase when operating below 300 °C and 2 MPa, which results in severe lattice strains and the membrane becomes brittle after only a few cycles between the two phases. Surface poisoning, especially due to sulphide layer formation from H_2S and active sites covered by CO, have been shown to have detrimental effects on the hydrogen permeation through Pd membranes [17, 18]. Today, most interest is in ternary Pd-based alloys where Cu, Ag and Au are the most common alloying metals [19, 20]. Au and Ag increase the hydrogen permeation rate and the temperature at which the membrane can operate without going through the hydride phase transition [21, 22]. Cu-alloying greatly reduces the amount of sulphide formation in the presence of H_2S, thus increasing the surface poisoning resistance [23].

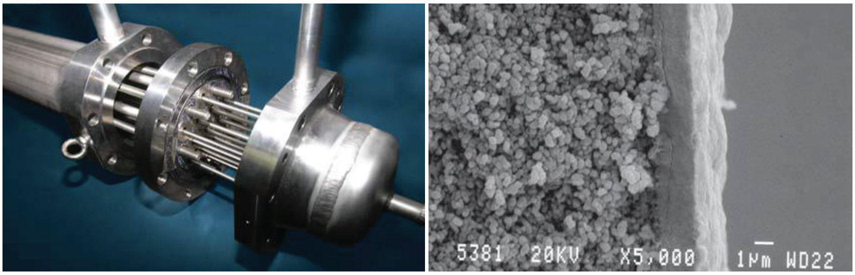

Figure 1.4. a) ECN Hydrogen Separation Module Hysep® 1308; b) SEM cross-section of the Pd-based membrane on a porous ceramic support [24].

Thin membranes (5-15 µm) based on the above Pd-alloys deposited on a range of porous substrates are under commercial development, as exemplified in Figure 1.4 [24]. Geometries where the metallic membranes are used as pore fillers in alumina substrates have also been implemented [25], and have shown to alleviate some of the internal strains and stresses from hydrogen embrittlement. Many companies are currently testing their membranes in pilot-scale installations, where hydrogen fluxes of around 0.1-0.6 $mol \cdot m^{-2} \cdot s^{-1}$ at temperatures around 400 °C with Δp of about 7 bar are displayed [26, 27]. Some of these membranes have also been proven stable in gas mixtures with some amounts of H_2S and CO over long durations. However, there are still very few reports of metal-based membranes which are stable at the ideal operating conditions for methane steam reforming [27].

Dense ceramic membranes

In dense mixed proton electron conducting ceramic membranes, hydrogen migrates by means of coupled transport of protons and charge compensating electrons or electron holes, in contrast to metals and porous membranes where hydrogen is considered to diffuse through atomic or molecular hydrogen. Thus, the permeability of hydrogen through a dense mixed proton electron conducting ceramic membrane is dependent on the conductivity of both the protons and the electronic species. These membranes potentially offer systems with excellent permselectivity[2] towards hydrogen, chemical and mechanical stability at high temperatures and low manufacturing cost [28]. The operating temperature of proton conducting membranes is typically within the range of 500 – 900 °C, which opens for thermal integration in power cycles as compared to the low temperature membranes previously described. Moreover, the oxidic nature of these membranes makes them less catalytically active towards coking, which is a detrimental issue in non-oxidative de-hydrogenation of natural gas (cf. Fig 1.2b).

Still, the hydrogen permeability of proton conducting membranes is still far inferior to the best metal and porous membranes [2, 10]. Despite on-going research in this field over the last decade, it has proven quite challenging to discover and develop materials which combine sufficient electronic and proton conductivity. Thus, an alternative approach involving composite ceramic metal (cermet) membranes has been investigated to circumvent this issue. In cermets, electrons are conducted through the metallic phase and protons through the ceramic phase, thus alleviating the need for a mixed proton electron conductor. The ceramic phase also serves to improve the mechanical properties of the membrane as compared with a thin metallic alloy membrane. However, it has proven difficult to develop materials which are compatible over a wide range of temperatures and atmospheres, without creating defects in the membrane that deteriorate the selectivity.

1.3. Proton conducting oxides – Current status and remaining challenges

The most commonly studied high temperature proton conducting oxides comprise acceptor-doped alkaline-earth based perovskites. Yttrium-doped barium cerate and zirconate exhibit the highest bulk proton conductivities, in the range of 0.01 $\mathrm{Scm^{-1}}$ at 600 °C in wet atmospheres [29]. These are essentially pure proton conductors also under wet reducing conditions (i.e. negligible n-type conductivity), such that hydrogen permeation from a hydrogen-rich feed gas is limited by the electronic conductivity. Acceptor-doped strontium cerate displays proton conductivities about a factor of two lower than the barium based perovskites, but the n-type conductivity is significantly higher. At present, hydrogen permeation in $SrCeO_3$ based systems is far superior to any other single phase perovskite-based proton conductor, and represents the benchmark for hydrogen permeability [28, 30-33]. The highest reported hydrogen flux to date was for a 2 μm thin Eu-doped $SrCeO_3$ membrane, with a flux density of 15 mL min^{-1} cm^{-2} operated at 950 K and 0.2 atm of H_2 on the feed side and He as the sweep gas [3]. The electronic conductivity was limiting hydrogen permeation for these membranes, despite the higher n-type conductivity compared to the barium-based perovskites. Although strontium cerate represents the state-of-the-art in terms of hydrogen permeability, its applicability as a hydrogen transport membrane may prove difficult due to low chemical stability towards acidic gases such as CO_2 [34] and high steam concentrations under reducing conditions [35]. Thus, an important challenge to dense ceramic hydrogen membranes is to discover and develop alternative materials that display high chemical stability combined with excellent transport properties.

---

[2] Permselectivity is the preferential permeation of certain species through a membrane. Thus, for porous materials with large pores, the permselectivity between hydrogen and oxygen is poor, as both gas molecules can permeate easily through the membrane.

Recently, the lanthanide tungsten oxides have emerged as a novel class of mixed proton electron conducting oxides with better chemical stability than the alkaline earth based perovskites [36-38]. Lanthanum tungsten oxide with the composition $La_{27}W_5O_{55.5}$ presents the highest proton conductivity among the tested materials, e.g. in the order of 0.001 $S \cdot cm^{-1}$ at 600 °C under wet conditions. Hydrogen permeation has been measured for some of the lanthanide tungsten oxides, with permeation rates close to the benchmark strontium cerate [39-41]. However, hydrogen permeation below 800 °C was limited by electronic conductivity also for these materials. Increased n-type electronic conductivity in lanthanum tungsten oxide has been achieved by partial substitution of W^{6+} with Mo^{6+}, without significantly affecting the ionic and protonic conductivity [42, 43]. These characteristics demonstrated that the lanthanum tungsten oxides are interesting candidate materials for hydrogen technologies, and Mo-substituted lanthanum tungstate as particularly interesting for hydrogen transport membranes.

The technologies based on proton conducting ceramics are still in their infancy, and there are many challenges that lie ahead when moving towards large scale commercialization. Firstly, controlled manufacturing of dense, thin, and defect-free films is necessary to reduce the ohmic resistance through the bulk material. Application of thin films may, however, lead to additional challenges related to the long-term stability under realistic operating conditions (i.e. large chemical potential gradients and elevated temperatures) [3]. Cation diffusion related degradation such as kinetic demixing and decomposition as well as chemical creep (“membrane walkout”) can severely influence the operational stability of a thin membrane exposed to large chemical potential gradients [44, 45]. Moreover, as the membrane thickness is decreased, the surface chemistry becomes increasingly important to the membrane performance. Slow surface kinetics can limit hydrogen permeation through the membrane and result in non-linear chemical potential profiles and transport phenomena for thin film proton conducting membranes. Thus, understanding the cation diffusion and surface kinetic properties of proton conducting oxides is vital to evaluate their prospects for long-term operation under large chemical potential gradients at high temperatures. These challenges further underline the importance of developing consistent mathematical models that can describe and predict both the concentration profiles and transport properties within the bulk interior itself, and the chemical reactions occurring at the membrane surfaces. This is especially important in materials with three or more mobile species, typical for proton conductors at high temperatures.

1.4. Aim and contents of this thesis

This thesis aims to improve the descriptive, qualitative, and quantitative understanding of the underlying processes within a proton conducting oxide under chemical potential gradients. These comprise not only the transport of protons, electrons and oxide ions, but also the less mobile constituent cations. The latter is of major importance to the long-term stability of ceramic membranes under chemical gradients, as relatively fast transport of the cations may lead to degradation of the membrane performance. Central in this work is also the development and evaluation of predictive mathematical models for transport in oxides with three or more charge-carrying defects under chemical potential gradients.

The main part of this thesis consists of 6 manuscripts. A brief description of their content is provided:

Manuscript I, "*Fabrication, structural and electrical characterization of lanthanum tungstate films by pulsed laser deposition*", focuses on the deposition of thin (1-4 µm) films of lanthanum tungsten oxide and subsequent characterization. Optimal deposition parameters were sought-after, and characterization by XRD, XPS, SEM, EPMA and electrical measurements were conducted to verify that the deposited films retained the properties of lanthanum tungsten oxide.

In Manuscript II, "*Hydrogen permeation characteristics of* $La_{27}W_{3.5}Mo_{1.5}O_{55.5}$", the hydrogen permeation and competing oxygen permeation (water splitting effect) in Mo-substituted LWO was characterized to evaluate its potential as a hydrogen transport membrane.

Manuscripts III and IV, "*Inter-diffusion in lanthanum tungsten oxide"* and "*Chemical tracer diffusivity of cations in lanthanum tungsten oxide*", investigate the cation diffusion properties of lanthanum tungsten oxide by means of inter-diffusion and chemical tracer diffusion studies. Cation diffusion coefficients for both La- and W-site diffusivity were obtained as a function of temperature under both oxidizing and reducing conditions, and the mechanism for bulk transport of cations in LWO was established. In the latter manuscript, the grain boundary diffusion characteristics are described in further detail.

Manuscript V, "*Interpretation of defect and gas phase fluxes through mixed-conducting ceramics using Nernst-Planck-Poisson and Integral formulations*", focuses on mathematical predictive models for defect and gas phase transport through mixed ionic-electronic conductors under electrochemical potential gradients. The model theory is compared to the more common integral solution to Wagner transport theory, in order to evaluate the applicability of both models under for different applications. Supporting information on transient modelling can be found in Appendix.

Before I present the six manuscripts in Chapter 5, I will first introduce the reader to some of the fundamentals of defect chemistry and transport in Chapter 2, and present the concept of oxides exposed to electrochemical gradients in Chapter 3. Chapter 4 will comprise experimental descriptions supplementary to what is provided in the manuscripts. In Chapter 6, I discuss the most important findings from the individual manuscripts collectively, aiming to bring further insight into the presented results.

2. Transport in ionic solids

In this chapter, the processes and physics that govern transport in ionic solids will be described. The aim is to provide supplementary background for the theoretical and experimental work presented in the attached manuscripts. Manuscripts II, V and VI describe both Nernst-Planck and Wagner transport theory in rigorous detail, which will thus not be treated here. Emphasis will rather be put on defect chemistry, micro- and macroscopic aspects of diffusion in ionic solids and the phenomenological diffusion coefficients. Mathematical derivations and interpretations specific to the diffusion experiments conducted in this thesis will be presented in Chapter 4.

2.1. Defects in oxides

Transport in ionic materials is facilitated by the presence of defects, i.e. deviations from the perfect crystalline lattice. In this treatment we will focus primarily on non-dimensional defects, also called point defects (e.g. electrons, vacancies or interstitials). Point defects may be formed by internal reactions within the material (intrinsic defect formation) or through interaction with external phases, such as surrounding gases (extrinsic defects). Schottky defect formation (Eq. 2.1) is an example of the former, while creation of oxygen vacancies through the release of oxygen gas is an external defect reaction (Eq. 2.2). Here the equations are written in Kröger-Vink notation for barium zirconate, $BaZrO_3$.

$$0 \rightleftarrows \mathrm{v}_{\mathrm{Ba}}^{//} + \mathrm{v}_{\mathrm{Zr}}^{////} + 3\mathrm{v}_{\mathrm{O}}^{\bullet\bullet} \ . \qquad (2.1)$$

$$\mathrm{O}_{\mathrm{O}}^{\mathrm{x}} \rightleftarrows \mathrm{v}_{\mathrm{O}}^{\bullet\bullet} + 2\mathrm{e}^{/} + \tfrac{1}{2}\mathrm{O}_2(\mathrm{g}) \ . \qquad (2.2)$$

In functional oxides, it is common to deliberately introduce an aliovalent dopant to promote additional defect formation. For example, barium zirconate is typically doped with Y forming an acceptor; $\mathrm{Y}_{\mathrm{Zr}}^{/}$. Conversely, if yttrium rather substituted barium it would act as a donor ($\mathrm{Y}_{\mathrm{Ba}}^{\bullet}$). Under ideal conditions (i.e. dilute concentrations), the equilibrium concentrations can be expressed through the mass action law and related to the equilibrium constant, exemplified for the Schottky equilibrium in Equation 2.1:

$$\mathrm{K}_{Sc} = X_{\mathrm{v}_{\mathrm{Ba}}^{//}} X_{\mathrm{v}_{\mathrm{Zr}}^{////}} X_{\mathrm{v}_{\mathrm{O}}^{\bullet\bullet}} = \frac{\left[\mathrm{v}_{\mathrm{Ba}}^{//}\right]}{[\mathrm{Ba}]} \frac{\left[\mathrm{v}_{\mathrm{Zr}}^{////}\right]}{[\mathrm{Zr}]} \frac{\left[\mathrm{v}_{\mathrm{O}}^{\bullet\bullet}\right]^{3}}{[\mathrm{O}]^{3}} = \exp\left(\frac{\Delta S_{\mathrm{Sc}}^{0}}{R}\right) \exp\left(-\frac{\Delta H_{\mathrm{Sc}}^{0}}{RT}\right) \quad . \qquad (2.3)$$

Here, *X* denotes site fractions of related defects, and the square brackets represent mole fractions. The concentrations in the denominators (i.e. [Ba]) comprise the standard state mole fractions for the site the defect is occupying. $\Delta S_{\mathrm{Sc}}^{0}$ and $\Delta H_{\mathrm{Sc}}^{0}$ denote the standard changes in entropy and enthalpy of the Schottky reaction, respectively. Similarly, an equilibrium constant for the reverse oxidation reaction (Eq. 2.2) may be expressed as

$$\mathrm{K'}_{\mathrm{ox}} = \frac{\left[\mathrm{v}_{\mathrm{O}}^{\bullet\bullet}\right]\left[\mathrm{e}^{/}\right]^{2}}{\left[\mathrm{O}_{\mathrm{O}}^{\mathrm{x}}\right]} p_{\mathrm{O}_2(\mathrm{g})}^{1/2} = \mathrm{K'}_{\mathrm{ox}}^{0} \exp\left(-\frac{\Delta H_{\mathrm{ox}}^{0}}{RT}\right). \qquad (2.4)$$

From Equation 2.4, the concentration of oxygen vacancies and electrons is directly linked to the partial pressure of oxygen. The equilibrium constant is marked with a prime to illustrate that the definition of standard state (e.g. standard-state occupancy of delocalized electron sites) is not straightforward. The consequence on entropy is then rather included in a pre-exponential replacement constant $\mathrm{K'}_{\mathrm{ox}}^{0}$. However, in highly ionic materials with large band gaps, electronic defects are more commonly present as localized small polarons. As such, it is common to define the standard-state occupancy of small polarons as unity per unit cell.

In proton conducting oxides, oxygen vacancies hydrate in the presence of water vapour to form protons, as described by the hydration reaction

$$\mathrm{H_2O(g)} + \mathrm{v_O^{\bullet\bullet}} + \mathrm{O_O^x} \rightleftarrows 2\mathrm{OH_O^{\bullet}} \quad , \tag{2.5}$$

with the corresponding equilibrium constant

$$K_{\mathrm{hydr}} = \frac{[\mathrm{OH_O^{\bullet}}]^2}{[\mathrm{O_O^x}][\mathrm{v_O^{\bullet\bullet}}]p_{\mathrm{H_2O}}} = \exp\left(\frac{\Delta_{\mathrm{hydr}}S^0}{R}\right)\exp\left(-\frac{\Delta_{\mathrm{hydr}}H^0}{RT}\right) \quad . \tag{2.6}$$

Following similar procedures, the concentrations of all relevant defects present in an oxide can be expressed in terms of thermodynamic parameters and partial pressures of surrounding gases. By introducing the following two relations that govern the defect concentrations – charge neutrality and site balance – a full defect chemical model for a given material can be derived. For example, oxygen site balance for barium zirconate requires that

$$[\mathrm{O_O^x}] + [\mathrm{v_O^{\bullet\bullet}}] + [\mathrm{OH_O^{\bullet}}] = 3 \,, \tag{2.7}$$

and the electroneutrality requires that the net effective charge be zero

$$[\mathrm{e}^{/}] + [\mathrm{Y_{Zr}^{/}}] = [\mathrm{h^{\bullet}}] + 2[\mathrm{v_O^{\bullet\bullet}}] + [\mathrm{OH_O^{\bullet}}] \quad . \tag{2.8}$$

In principle, all defects that carry an effective charge should be implemented in the electroneutrality conditions. However, the concentration of cation interstitials and vacancies are generally considered negligible in the oxides studied in this work, and are thus omitted from the simplified electroneutrality condition.

2.2. Defect chemistry of lanthanum tungsten oxide

The experimental work that comprises the majority of this thesis has focused on the novel proton conducting oxide lanthanum tungsten oxide (LWO). Recent work has shown that the defect chemistry differs from the traditional systems described above, and in this section the crystal structure and defect chemistry of LWO will be described in further detail based on the work by Erdal *et al.* [46].

In order to accurately describe defects in an oxide, the perfect standard state of the parent structure must be properly defined. For LWO one formula unit is written as $La_{28-x}W_{4+x}O_{54+3x/2}v_{2-3x/2}$, where x denotes the amount of W on La sites and v refers to vacant oxygen sites [47, 48]. In the perfect structure x = 0 and the La/W-ratio is 7, henceforth referred to as LWO70 (where the number refers to the La/W-ratio multiplied by 10). The oxygen sublattice is considered to be defective (partially occupied) so that the perfect oxygen sites are statistically occupied by 54/56 oxide ions and 2/56 vacancies. This yields an ideal charge of the standard state oxygen site as $\frac{-108}{56}$, which is not carried by any real species. As a consequence, both oxide ions and oxygen vacancies are effectively charged defects in the LWO structure, denoted as $O_{\frac{54}{56}O}^{\frac{4}{56}/}$ and $v_{\frac{54}{56}O}^{\frac{108}{56}\bullet}$, respectively.

Experimental work has shown that LWO can be synthesized only when the La/W-ratio is between 5.3 and 5.7 [48], which results in a considerable concentration of tungsten atoms residing on lanthanum sites [46]. It has been proposed that the amount of oxygen vacancies is too large in the perfect parent structure, and excess tungsten is incorporated to lower the concentration of oxygen vacancies. Both experimental and theoretical work has confirmed that tungsten resides on the lanthanum sites in the 6+ oxidation state, effectively acting as a triply charged donor ($W_{La}^{\bullet\bullet\bullet}$) [47].

The experimental work in this thesis is mainly on the LWO54 composition (La/W-ratio of 5.4). Here, x = 1 and the formula unit can be written as $La_{27}W_5O_{55.5}v_{0.5}$. Thus, 1.5 out of the 2 native oxygen vacancies are occupied by oxide ions in order to charge compensate the tungsten donors on lanthanum site. If we consider electrons and electron holes as minority defects and that protons may hydrate the oxygen vacancies under wet conditions, the electroneutrality condition can be written as

$$\frac{4}{56}\left[\mathrm{O}_{\frac{54}{56}\mathrm{O}}^{\frac{4}{56}/}\right] = \frac{108}{56}\left[\mathrm{v}_{\frac{54}{56}\mathrm{O}}^{\frac{108}{56}\bullet}\right] + \frac{52}{56}\left[\mathrm{OH}_{\frac{54}{56}\mathrm{O}}^{\frac{52}{56}\bullet}\right] + [\mathrm{W}_{\mathrm{La}}^{\bullet\bullet\bullet}] \ . \qquad (2.9)$$

2.3. Diffusion theory

The concept of diffusion can be considered from two different perspectives; the *phenomenological* description (macroscopic) which starts with Fick's laws, and the *atomistic* description (microscopic) which considers random walk of the diffusing species. In this chapter, I will first introduce the atomistic description of random diffusion, with examples for various diffusion mechanisms. Thereafter, Fickian diffusion and the different *phenomenological* diffusion coefficients will be introduced in light of the experimental work that comprises this thesis.

2.3.1 Random diffusion

The random diffusion coefficient in a cubic structure can be expressed as a function of the jump distance between two adjacent sites, a, the jump frequency, ω, and the number of available sites to which the particle can jump, N_d, as

$$D_r = \alpha a_0^2 \, \omega N_{\mathrm{d}} \ . \qquad (2.10)$$

α is the geometrical factor which involves the number of adjacent sites and the relation between the jump distance and the lattice parameter. The jump frequency, ω, is an activated process, related to the vibrational attempt frequency, ν, and the entropy and enthalpy of mobility (ΔS_m and ΔH_m, respectively) as

$$\omega = \nu \exp\left(\frac{\Delta S_\mathrm{m}}{R}\right) \exp\left(-\frac{\Delta H_\mathrm{m}}{RT}\right) \quad . \tag{2.11}$$

The vibration frequency is often assumed to be in the order of the Debye frequency, i.e. 10^{13} Hz. The entropy change is assumed to be a small, positive term, below 10 Jmol^{-1}K^{-1}. The probability of a neighbouring site being unoccupied, N_d, is dependent on the diffusion mechanism and the crystal lattice in which the jump takes place. For transport of a constituent in an elemental solid, N_d can be expressed simply by the formation thermodynamics of the facilitating defect (i.e. vacant lattice sites) as

$$N_\mathrm{d} = \exp\left(\frac{\Delta S_f}{R}\right) \exp\left(-\frac{\Delta H_f}{RT}\right) \quad . \tag{2.12}$$

Insertion of Equations 2.11 and 2.12 into Eq. 2.10 leads to a final expression for the random diffusion coefficient:

$$D_r = \alpha a_0^2 \nu \exp\left(\frac{\Delta S_\mathrm{m} + \Delta S_f}{R}\right) \exp\left(-\frac{\Delta H_\mathrm{m} + \Delta H_f}{RT}\right) \quad . \tag{2.13}$$

Here, $\alpha a_0^2 \nu \exp\left(\frac{\Delta S_\mathrm{m} + \Delta S_f}{R}\right)$ is commonly referred to as the pre-exponential term of diffusion coefficient, D_r^0. $\Delta H_\mathrm{m} + \Delta H_f$ is the activation energy, E_a, for diffusion. The vibrational attempt frequency can generally be estimated from the enthalpy of defect migration and the species' reduced mass, M[3]:

$$\nu = \frac{2}{\pi a}\sqrt{\frac{\Delta H_{\mathrm{m}}}{M}} \quad . \tag{2.14}$$

Having properly established an atomistic perspective on random diffusion in solids, I will now turn to describe in further detail the principles of the major diffusion mechanisms in polycrystalline oxides.

2.3.2 Vacancy mechanism

Diffusion occurs via the vacancy mechanism when an atom on a normal site jumps to an adjacent and unoccupied (vacant) site in the lattice. Thus, the concentration of available neighbouring sites (N_{d}) is given by the concentration of vacant lattice sites. As an example, we consider oxide ion diffusion via the vacancy mechanism in a binary oxide (AO) dominated by anion Frenkel disorder ($\mathrm{O}_{\mathrm{O}}^{\mathrm{x}} \rightleftharpoons \mathrm{v}_{\mathrm{O}}^{\bullet\bullet} + \mathrm{O}_{\mathrm{i}}^{//}$). The concentration of oxygen vacancies can be expressed as a function of the standard change in entropy and enthalpy of the anion Frenkel reaction as

$$[\mathrm{v}_{\mathrm{O}}^{\bullet\bullet}] = [\mathrm{O}_{\mathrm{i}}^{//}] = \exp\left(\frac{\Delta S_{\mathrm{F}}^{0}}{2R}\right)\exp\left(-\frac{\Delta H_{\mathrm{F}}^{0}}{2RT}\right) \quad . \tag{2.15}$$

Thus, the self-diffusion coefficient for oxide ions can be expressed as

---

[3] The reduced mass refers to both species involved in the assumed harmonic motion. Thus, the reduced mass is expressed as: $\frac{1}{M} = \frac{1}{m_1} + \frac{1}{m_2}$, where m_1 and m_2 denotes the mass of species 1 and 2 involved in the motion.

$$
\begin{aligned}
D_{\mathrm{O}^{2-}} &= [\mathrm{v}_{\mathrm{O}}^{\bullet\bullet}]\,\alpha a_0^2 \omega \\
&= \alpha a_0^2 \nu \exp\left(\frac{\Delta S_{\mathrm{m,v}_{\mathrm{O}}^{\bullet\bullet}} + \frac{\Delta S_{\mathrm{F}}^0}{2}}{R}\right) \exp\left(-\frac{\Delta H_{\mathrm{m,v}_{\mathrm{O}}^{\bullet\bullet}} + \frac{\Delta H_{\mathrm{F}}^0}{2}}{RT}\right). \qquad (2.16)
\end{aligned}
$$

In cubic structures, the geometrical factor, α, is typically assumed to be unity for vacancy diffusion. The activation energy, E_a, for oxide ion diffusivity contains both the enthalpy of migration and formation of oxygen vacancies.

In oxygen-deficient oxides where oxygen vacancies and electrons are the dominating defects, the vacancy concentration – and thus also the diffusion coefficient – would contain an additional dependency on the partial pressure of oxygen as

$$
D_{\mathrm{O}^{2-}} = \alpha a_0^2 \nu \exp\left(\frac{\Delta S_{\mathrm{m,v}_{\mathrm{O}}^{\bullet\bullet}} + \frac{\Delta S_{\mathrm{ox}}^0}{3}}{R}\right) \exp\left(-\frac{\Delta H_{\mathrm{m,v}_{\mathrm{O}}^{\bullet\bullet}} + \frac{\Delta H_{\mathrm{ox}}^0}{3}}{RT}\right) p_{\mathrm{O}_2}^{-1/6} \ . \qquad (2.17)
$$

Here, ΔS_{ox}^0 and ΔH_{ox}^0 are the standard change in entropy and enthalpy for the reaction described in Equation 2.2[4]. For typical acceptor doped oxides where the vacancy concentration is constant and determined by the acceptor concentration ($2[\mathrm{v}_{\mathrm{O}}^{\bullet\bullet}] = [Acc^{/}]$), the activation energy would only comprise the migration enthalpy.

2.3.3 Interstitial mechanism

When an atom residing on an interstitial lattice site moves from one interstitial site to another, the diffusion occurs via the interstitial mechanism. In a dilute system, the probability of a neighbouring site being unoccupied (N_d) is close to unity. Thus, the diffusion coefficient of interstitial oxide ions can be expressed as

---

[4] Here, we have assumed that the electrons are highly localized such that the standard state for electrons is properly established, and we are able to express the entropy term of the reaction.

$$D_{\mathrm{O}_\mathrm{i}^{//}} = \alpha a_0^2 \nu \exp\left(\frac{\Delta S_{\mathrm{m},\mathrm{O}_\mathrm{i}^{//}}}{R}\right) \exp\left(-\frac{\Delta H_{\mathrm{m},\mathrm{O}_\mathrm{i}^{//}}}{RT}\right) \quad . \tag{2.18}$$

Now, if we want to express the oxide ion diffusion coefficients (i.e. averaged over all oxide ions in the structure), the probability of any particular oxide ion being at an interstitial site – i.e. the concentration of oxygen interstitials – must be included. Thus, for the same anion-Frenkel dominated oxide described in the previous treatment (cf., Eq. 2.15), the formation thermodynamics of oxygen interstitials must be included:

$$\begin{aligned} D_{\mathrm{O}^{2-}} &= X_{\mathrm{O}_\mathrm{i}^{//}} D_{\mathrm{O}_\mathrm{i}^{//}} \\ &= \alpha a_0^2 \nu \exp\left(\frac{\Delta S_{\mathrm{m},\mathrm{O}_\mathrm{i}^{//}} + \frac{\Delta S_\mathrm{F}^0}{2}}{R}\right) \exp\left(-\frac{\Delta H_{\mathrm{m},\mathrm{O}_\mathrm{i}^{//}} + \frac{\Delta H_\mathrm{F}^0}{2}}{RT}\right) \quad . \end{aligned} \tag{2.19}$$

For interstitial diffusion the geometrical factor, α, depends strongly on both the crystal structure of the host lattice and which interstitial sites are occupied by the diffusing species. By way of example, it can be shown that $\alpha = 1/6$ for interstitial atoms occupying the octahedral interstitial sites in a bcc lattice.

So far I have described diffusion in metal oxides from an atomistic perspective and established the general theory for the two major diffusion mechanisms. I have chosen oxide ions as my primary example of a mobile species, but the same principles are valid for diffusion of other species such as host cations and lattice impurities. I will now turn to discuss the diffusion mechanism of protons in more detail, as proton migration does not follow the mechanisms described above.

2.3.4 Proton diffusion

Protons dissolve in oxides and form associates with oxide ions (hydroxide ions), where the protons are embedded in the valence electron cloud of the oxide ions. Thus, the protonic defect is highly localized next to an oxide ion in the lattice, and has two potential diffusion mechanisms: i) Grotthuss mechanism (rotation and hopping) or ii) the vehicle mechanism.

The Grotthuss mechanism is the principal method of proton transport in ionic oxides. For transport via this mechanism, a proton must first align its orientation in the electron cloud towards a nearest neighbour oxide ion (rotation) before it can complete a jump onto the electron cloud of the adjacent oxide ion (hopping). The energy barrier associated with the hopping step is believed to be highest, and thus rate-determining for transport. Although the proton hopping is described as an independent motion of the protonic species, it is in fact the vibrational modes of the oxide and hydroxide ions that determine the jump rates for protons.

The Grotthuss mechanism can be considered very similar as the interstitial mechanism, with one "interstitial proton site" next to each oxide ion in the structure. Thus, essentially all nearest neighbour oxide ions have an "unoccupied" interstitial site to which the proton can jump ($N_\mathrm{d} = 1$). The specification of the geometrical factor and the jump rate is not as straightforward. The dynamics is complicated by the multistep process, the dependency on the oxygen sublattice dynamics and the quantum-like behaviour of light particles such as protons. However, the migration enthalpy and entropy is generally considered to be related to the jump from one oxygen atom to another. An empirical relation between the enthalpy of migration for vacancies and protons has been proposed and expressed as

$$\Delta H_{\mathrm{m,OH}_\mathrm{O}^\bullet} \approx \frac{2}{3}\Delta H_{\mathrm{m,v}_\mathrm{O}^{\bullet\bullet}} \quad . \tag{2.20}$$

In the vehicle mechanism, the proton is considered as a passenger on a mobile hydroxide ion moving through the lattice. For example, the hydroxide ion may diffuse via the vacancy mechanism, effectively transporting both an oxide ion and a proton. In relatively open structures, water molecules and hydronium ions may also serve as vehicles for proton diffusion.

2.4. Macroscopic diffusion

Fick's laws describe diffusion as a phenomenological process where the diffusion coefficient acts as a proportionality factor. Fick's first law relates the diffusive flux of a species i to its concentration gradient as

$$\boldsymbol{J}_{i,\mathrm{d}} = -D_i \nabla c_i \quad . \tag{2.21}$$

D_i is the diffusion coefficient of species i, which can be related to the charge carrier mobility, u_i, conductivity, σ_i, charge, z_i, and concentration, c_i, according to the Nernst-Einstein relation:

$$D_i = u_i \frac{RT}{zF} = \frac{\sigma_i}{c_i} \frac{RT}{(z_i F)^2} \quad . \tag{2.22}$$

R denotes the gas constant, F the Faraday constant and T the temperature in Kelvin. Fick's first law is a steady-state expression, where neither the diffusivity nor the concentration gradient varies with position x and time t, and is thus applied to steady-state experiments such as permeation measurements. In non-steady state situations, a balance equation is required. If no reactions occur (i.e. no production or consumption of the participating species), the continuity equation is applied:

$$\frac{\mathrm{d}c_i}{\mathrm{d}t} + \nabla \boldsymbol{J}_{i,\mathrm{d}} = 0 \quad . \tag{2.23}$$

Combining Equations 2.21 and 2.23 yields Fick's second law (also called the diffusion equation):

$$\frac{\mathrm{d}c_i}{\mathrm{d}t} = \nabla(D_i \nabla c_i) \qquad (2.24)$$

Fick's second law forms the basis for all solutions to transient diffusion problems such as solid state reaction, inter-diffusion and conductivity relaxation experiments. However, we note that it is a partial differential equation which cannot be solved without introducing boundary conditions to the diffusion problem. Analytical solutions relevant for the cation diffusion measurements in this work are presented in Chapter 4.6.

Fick's equations are not strictly correct for transport in non-ideal solids where multiple species are present. Firstly, the influence of other species on the transport parameters for species i are neglected, *i.e.* the cross-coefficients in the Onsager matrix[5]. Secondly, the driving force for the diffusional flux is more accurately represented in terms of the chemical potential gradient, $\nabla\mu_i = \frac{RT\nabla c_i}{c_i}$;

$$\boldsymbol{J}_{i,\mathrm{d}} = -\frac{D_i c_i}{RT}\nabla\mu_i \ . \qquad (2.25)$$

So far, I have only considered diffusional flux due to a gradient in concentration. For charged species, an additional contribution from migration ($J_{i,\mathrm{m}}$) due to an electrostatic potential gradient, $\nabla\Phi$, may contribute to the total flux density

---

[5] A proper treatment would replace the single diffusion coefficient and concentration gradient with cross-coefficients in the Onsager matrix for all species k in the: $J_i = \sum_k D_{i,k}\nabla c_k$, where $D_{i,k}$ denotes the diffusion coefficient for species i associated with species k. If all cross-coefficients are discarded, we are left with the single contribution $J_i = D_{i,i}\nabla c_i$.

$$\boldsymbol{J}_i = \boldsymbol{J}_{i,\mathrm{d}} + \boldsymbol{J}_{i,\mathrm{m}} = -\frac{D_i c_i}{RT}[\nabla\mu_i + z_i F \nabla\Phi] \quad , \tag{2.26}$$

where $\nabla\mu_i + z_i F\nabla\Phi$ is defined as the electrochemical potential gradient acting on species i ($\nabla\eta_i$). Equation 2.26 can be recognized as the Nernst-Planck equation used in Manuscripts V and VI, and forms the basis for detailed description of defect fluxes through mixed ionic electronic conducting oxides under electrochemical potential gradients.

2.5. Phenomenological diffusion coefficients

Having defined the random diffusion coefficient from a microscopic perspective and described macroscopic diffusion based on Fick's laws, I will now turn to describe the *phenomenological* diffusion coefficients – what we are able to measure macroscopically. The macroscopic diffusion coefficients are specific to the method by which they were obtained, and can all be related to the random self-diffusion coefficient.

2.5.1 Self-diffusion coefficient

The most general phenomenological diffusion coefficient is termed the charge diffusion coefficient, which is obtained by steady-state conductivity experiments. Here, the electrons are passed through an external circuit and there is no concentration gradient of the mobile ionic species within the solid. Thus, the driving force for transport is only the electric field (cf. Eq. 2.26). Let us consider a metal oxide which exclusively conducts oxide ions. Based on the Nernst-Einstein relation (cf., Eq. 2.22), we can formally relate the measured conductivity to a diffusion coefficient [49];

$$D^{Q}_{\mathrm{O}^{2-}} \equiv \frac{RT}{4F^2}\frac{\sigma_{\mathrm{O}^{2-}}}{c_{\mathrm{O}^{2-}}} \quad . \tag{2.27}$$

From Equation 2.27 we can see that the diffusion coefficient corresponds to the random self-diffusion coefficient of the oxide ions[6]. If oxide ions diffuse exclusively via vacant oxygen sites, we can simply obtain a relation between the macroscopic diffusion coefficient of the ions and the microscopic defect diffusion coefficient for oxygen vacancies:

$$D^{Q}_{\mathrm{O}^{2-}} = \frac{c_{\mathrm{v}_\mathrm{O}^{\bullet\bullet}}}{c_{\mathrm{O}^{2-}}} D_{\mathrm{v}_\mathrm{O}^{\bullet\bullet}}, \tag{2.28}$$

2.5.2 Tracer diffusion

Tracer diffusion is a common tool to obtain measurable diffusion profiles of a constituent element without altering the chemical composition of the solid. A fundamental example is the oxygen exchange experiment, where the ambient oxygen surrounding an oxide (primarily consisting of $^{16}O_2$ isotopes) is exchanged with a gas enriched in $^{18}O_2$. This leads to a tracer exchange in the solid due to counter-diffusion of the two isotopes ($j_{^{16}\mathrm{O}^{2-}} = -j_{^{18}\mathrm{O}^{2-}}$). Based on this, it can be shown that the flux of the tracer oxide ion (tracer elements are hereafter marked with an asterisk) is given by

$$j^{*}_{\mathrm{O}^{2-}} = \frac{\sigma_{\mathrm{O}^{2-}} RT}{4F^2 c_{\mathrm{O}^{2-}}} \nabla c^{*}_{\mathrm{O}^{2-}} \quad . \tag{2.29}$$

From here, the tracer diffusion coefficient can be recognized as

$$D^{*}_{\mathrm{O}^{2-}} = \frac{RT}{4F^2} \frac{\sigma_{\mathrm{O}^{2-}}}{c_{\mathrm{O}^{2-}}} \quad , \tag{2.30}$$

---

[6] The index *Q* is to indicate that the diffusion coefficient refers to the transport of charge.

which reflects the self-diffusion coefficient of oxide ions. However, tracer diffusion jumps are not completely random, but rather correlated with previous jumps to some extent. This deviation is represented by a correlation factor, *f*, which for vacancy diffusion in fcc crystals is approximated to 0.78, while it is unity for interstitial diffusion

$$D^{*} = Df^{*} \quad . \tag{2.31}$$

In cation tracer diffusion experiments such as the one presented in manuscript IV, it is generally difficult and expensive to obtain stable cation tracer isotopes of the same element. In such instances, a different element with similar chemical properties can instead be chosen as the tracer. For example, Nd was chosen as the chemical tracer for La diffusion in Manuscript IV.

2.5.3 Chemical diffusion

The final – and perhaps the most important – diffusion coefficient that will be covered here is the chemical diffusion coefficient; D^{δ}. Chemical diffusion describes transport kinetics under a chemical potential gradient under non-equilibrium conditions. In the following, chemical diffusion will be discussed in light of hydrogen transport due to a hydrogen potential gradient. In the one-dimensional case, the chemical diffusion of hydrogen can be described by Fick's first law (cf., Eq. 2.21) as

$$j_{\mathrm{H}_2} = \frac{1}{2} j_{\mathrm{H}} = D_{\mathrm{H}}^{\delta} \frac{\mathrm{d}c_{\mathrm{H}}}{\mathrm{d}x} \quad . \tag{2.32}$$

The net transport of hydrogen comprises transport of protons and electrons to maintain charge neutrality, which is termed ambipolar transport. By introducing the ambipolar conductivity of neutral hydrogen, $\sigma_{\mathrm{H}}^{\delta}$, the flux of hydrogen may be expressed as

$$j_{H_2} = \frac{1}{F^2} \sigma_H^{\delta} \frac{d\mu_H}{dx} = \frac{1}{F^2} \frac{\sigma_{OH_O^{\bullet}} \sigma_{e^{/}}}{\sigma_{OH_O^{\bullet}} + \sigma_{e^{/}}} \frac{d\mu_H}{dx} , \qquad (2.33)$$

where $d\mu_H/dx$ is the chemical potential gradient of neutral hydrogen. Comparing Eq. 2.33 to Eq. 2.32 and using the Nernst-Einstein relation, the chemical diffusion coefficient for hydrogen can be recognized as

$$D_H^{\delta} = \frac{1}{F^2} \sigma_H^{\delta} \frac{d\mu_H}{dc_H} = \frac{RT}{F^2} \frac{\sigma_H^{\delta}}{c_H} \frac{d\ln a_H}{d\ln c_H} , \qquad (2.34)$$

The thermodynamic factor ($w_H \equiv d\ln a_H / d\ln c_H$) in the above equation is difficult to determine, as hydrogen is not present in oxides as neutral hydrogen, nor is it randomly distributed. It is, however, possible to express Equation 2.34 at the level of the individual defects as [49]

$$D_H^{\delta} = \frac{RT}{F^2} \frac{\sigma_{OH_O^{\bullet}} \sigma_{e^{/}}}{\sigma_{OH_O^{\bullet}} + \sigma_{e^{/}}} \left(\frac{1}{c_{OH_O^{\bullet}}} \frac{d\ln a_{OH_O^{\bullet}}}{d\ln c_{OH_O^{\bullet}}} + \frac{1}{c_{e^{/}}} \frac{d\ln a_{e^{/}}}{d\ln c_{e^{/}}} \right) . \qquad (2.35)$$

In this way, the thermodynamic factors of the defects can be considered close to unity for weak disorder, and the chemical diffusion coefficient reduces to

$$D_H^{\delta} = \frac{RT}{F^2} \frac{\sigma_{OH_O^{\bullet}} \sigma_{e^{/}}}{\sigma_{OH_O^{\bullet}} + \sigma_{e^{/}}} \frac{1}{c_H^{\delta}} , \qquad (2.36)$$

where $\frac{1}{c_H^{\delta}} = \frac{1}{c_{OH_O^{\bullet}}} + \frac{1}{c_{e^{/}}}$ relates the ambipolar concentration of neutral hydrogen, c_H^{δ}, to the individual defect concentrations. By introducing the transference number $t_k = \frac{\sigma_k}{\sigma_{tot}}$, and assuming that the total conductivity is dominated by protonic and electronic conductivity, the chemical diffusion coefficient can be expressed as a weighted mean of the individual defect diffusion coefficients:

$$D_{\mathrm{H}}^{\delta} = t_{\mathrm{e}'} D_{\mathrm{OH}_{\mathrm{O}}^{\bullet}} + t_{\mathrm{OH}_{\mathrm{O}}^{\bullet}} D_{\mathrm{e}'} \quad . \tag{2.37}$$

Two major conclusions can be drawn from Equation 2.37; i) the chemical diffusion coefficient will be dominated by the slowest species and ii) the magnitude is in the order of the defect diffusivities, i.e. much faster than the ionic self-diffusion coefficients. Also, the chemical diffusion coefficient will experience an acceleration effect from the fastest species, and a braking effect from the slowest, effectively resulting in a chemical diffusivity between the two defect diffusivities.

2.5.4 Chemical inter-diffusion

Inter-diffusion is defined as the process of diffusing and mixing freely so as to approach a homogeneous mixture. In solid state science, the term is generally applied for the study of inter-diffusion between compounds with different composition. The first theoretical analysis of inter-diffusion was reported by Darken in 1948 for diffusion in binary alloys [50]. He showed that the inter-diffusion coefficient could be related to the individual tracer diffusion coefficients as

$$\widetilde{D}_{Darken} = (N_{\mathrm{A}} D_{\mathrm{B}} + N_{\mathrm{B}} D_{\mathrm{A}}) \Phi \quad . \tag{2.38}$$

Here, D_{A} and D_{B} are the diffusion coefficients of elements A and B (in compound B and A, respectively). N_{A} and N_{B} are the molar fractions of the compounds. Φ is the thermodynamic factor ($\Phi = \mathrm{dln}\, a_i / \mathrm{dln} N_i$). From Equation 2.38, it is clear that if the two tracer diffusion coefficients differ ($D_{\mathrm{A}} \neq D_{\mathrm{B}}$), the inter-diffusion coefficient will vary across the diffusion couple as the composition is changing. On the other hand, if the individual tracer diffusion coefficients are similar or identical, the inter-diffusion coefficient will remain essentially constant across the diffusion couple.

For systems where the individual tracer diffusion coefficients differ, the inter-diffusion problem becomes more complex. One phenomenon which is widely observed for inter-diffusion in substitutional alloys is the Kirkendall effect. The Kirkendall effect describes the net mass transport of the faster diffusing species, and thus a displacement of the contacting interface (Kirkendall plane) relative to a frame fixed in the local crystal lattice. The *Kirkendall velocity* of the Kirkendall plane is given by

$$v_{\mathrm{Kirkendall}} = V_{\mathrm{B}}(D_{\mathrm{B}} - D_{\mathrm{A}})\frac{\mathrm{d}c_{\mathrm{B}}}{\mathrm{d}x} \quad , \tag{2.39}$$

where V_{B} is the partial molar volume of compound B. For vacancy mediated diffusion, cation vacancies must be annihilated on one side and created on the other side of the inter-diffusion zone so that a vacancy flux is created to maintain local equilibrium. Over time, this can lead to *vacancy supersaturation* and pore formation (Kirkendall porosity). Thus, enhanced pore formation on one side of the diffusion couple and displacement of the contacting interface are two major indications for vacancy mediated inter-diffusion with different diffusion coefficients in the two phases.

3. Oxides in electrochemical potential gradients

So far, I have described and derived the important parameters which govern diffusion in oxides from microscopic and macroscopic perspectives. The driving force for transport was recognized as an electrochemical potential gradient acting on the mobile species. In the following, I will introduce the fundamental concepts of oxides exposed to external potential gradients, and their potential impact on proton conducting oxides under operating conditions for a range of applications. For the sake of simplicity, the derivations will be based on simple binary oxides. In most cases, the results are easily transferable to higher order oxides.

3.1. Binary oxides exposed to an oxygen potential gradient

In this treatment we shall consider an ideal solid solution of a binary oxide, $(A_{1-x}B_x)O$, with an immobile oxygen sublattice[7] exposed to an oxygen potential gradient. The Gibbs-Duhem relation states that chemical potential gradients of components A and B will be induced according to

$$x_{\mathrm{A}}\nabla\mu_{\mathrm{A}} + x_{\mathrm{B}}\nabla\mu_{\mathrm{B}} + x_{\mathrm{O}}\nabla\mu_{\mathrm{O}} = 0 \quad . \tag{3.1}$$

These thermodynamic forces generate fluxes of all mobile components, which for this oxide are cations A^{2+} and B^{2+}, and electronic species, which we assume is predominantly electron holes, h^+. We further assume that the oxide is cation deficient, such that the cations are moving by means of cation vacancies (V), and the flux of vacancies and cations are coupled as $j_{\mathrm{A}^{2+}} + j_{\mathrm{B}^{2+}} + j_{\mathrm{V}} = 0$. The induced chemical potential gradients and partial fluxes are depicted schematically in Figure 3.1. The cation fluxes are directed towards the high p_{O_2} side, and balanced by an opposite flux of electron holes [44, 45]. Thus, there is a net transport of mass towards the high p_{O_2} side. When the cation species and vacancies reach the oxide surfaces, chemical reactions must take place. At the high p_{O_2} side, the cations are oxidized by the surrounding oxygen atmosphere to produce cation vacancies, electron holes and new lattice molecules of the oxide (Eq. 3.2). The reverse reaction (reduction) takes place on the low p_{O_2} side, where vacancies and holes are annihilated together with an oxide molecule to produce cations and oxygen gas.

---

[7] Although oxide ions are generally highly mobile in oxygen deficient oxides such as acceptor doped perovskites, the oxygen sublattice can still be considered immobile in itself as oxide ions interact with the surrounding gases at both surfaces to produce and consume oxygen gas. Thus, the sublattice as a whole does not “move” in reference to the laboratory framework as such.

$$(\mathrm{A,B})^{2+} + \frac{1}{2}\,\mathrm{O_2(g)} \leftrightharpoons \mathrm{V} + 2\mathrm{h}^{+} + \ (\mathrm{A,B})\mathrm{O}\ . \qquad (3.2)$$

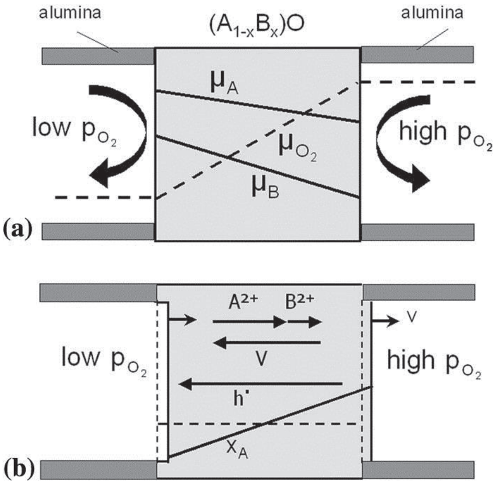

Figure 3.1. Schematic illustration of chemical potential distribution (a) and individual fluxes of the mobile species in a binary oxide ($A_{1-x}B_xO$) under an oxygen potential gradient [45].

One immediate consequence is that both oxide surfaces shift towards the high p_{O_2} side of the material, disrupting the morphology on both surfaces, commonly referred to as morphological instability [51, 52]. Secondly, the originally homogeneous oxide will become inhomogeneous if the cations have different diffusivities, with accumulation of the faster moving species towards higher oxygen potential side, and a corresponding accumulation of the slower species at the low p_{O_2} side. In solid solution oxides, as depicted here, this effect leads to so-called kinetic demixing of the oxide, shown in Figure 3.1b. If the demixing profile exceeds the solid solubility limit of the oxide, decomposition and formation of new phases may occur on the surfaces. The latter effect is termed kinetic decomposition, and is typically observed in line compounds of higher oxides (i.e. perovskites with narrow range of solid solubility). It should be emphasized that all three phenomena have a strictly kinetic origin, as it is assumed that the oxide is thermodynamically stable under both oxygen environments. Thus, if the applied potential gradient is removed, the directed fluxes will disappear and the material will become homogeneous again due to diffusion processes [45]. Further, it is important to note that these effects are not limited to oxides under oxygen potential gradients. The same processes may occur under an electric potential gradient, such as a semiconducting oxide under a voltage load. I will continue using an oxygen potential gradient as the working example, but the general discussion is also transferrable to other driving forces for cation transport.

3.2. Kinetic demixing

As we recall from chapter 2.3, the flux of the charged cations A^{z_A+} and B^{z_B+} can be expressed as a function of the diffusion coefficients and the electrochemical potentials as[8]

$$J_{\mathrm{A}^{z_\mathrm{A}+}} = \frac{D_\mathrm{A} c_\mathrm{A}}{RT} \nabla \eta_{\mathrm{A}^{z_\mathrm{A}+}} \,. \tag{3.3}$$

$$J_{\mathrm{B}^{z_\mathrm{B}+}} = \frac{D_\mathrm{B} c_\mathrm{B}}{RT} \nabla \eta_{\mathrm{B}^{z_\mathrm{B}+}} \,. \tag{3.4}$$

Again, all cross-coefficients of the Onsager matrix have been neglected, assuming an ideal solid solution with no defect-defect interactions. After an initial demixing period, the system will eventually reach a steady-state where both cations are moving with the same velocity, v_stat, relative to the immobile oxygen sublattice. Thus, the steady state condition can be written as[9]

$$v_\mathrm{stat} = \frac{J_{\mathrm{A}^{z_\mathrm{A}+}}}{c_\mathrm{A}} = \frac{J_{\mathrm{B}^{z_\mathrm{B}+}}}{c_\mathrm{B}} \quad . \tag{3.5}$$

By utilizing the equilibrium between the charged cations and their complementary elemental compounds and electrons ($\mathrm{A}^{z_\mathrm{A}+} + z_\mathrm{A}\mathrm{e}^- = \mathrm{A}$) and the flux expressions (Eqs. 3.3 and 3.4), we can obtain the demixing equation which relates the chemical potentials of the neutral constituent elements A and B and the electrochemical potential gradient of the electrons [53]:

$$\nabla \mu_\mathrm{B} = \gamma \nabla \mu_\mathrm{A} - (z_\mathrm{A}\,\gamma - z_\mathrm{B}) \nabla \eta_{\mathrm{e}^-} \quad . \tag{3.6}$$

---

[8] Here, I have permitted different charge states for the cations, to generalize for the case of ternary oxides and heterovalently doped binary oxides.

[9] Here, use have been made of the general relation; j = v*c

$\gamma \equiv D_A/D_B$ defines the ratio of the diffusion coefficients. The electrochemical potential gradient of electrons is determined by the transport properties of the membrane material and the experimental setup. Let us consider an oxide ion conducting electrolyte ($t_{O^{2-}} \cong 1$), with both sides of the membrane connected by an external circuit as in a typical fuel cell setup[10]. Assuming local equilibrium at the electrodes, the difference in electrochemical potential of the electrons between the two surfaces can be calculated as [54]

$$\Delta\eta_e = -F \cdot U = -\frac{\rho}{1+\rho}\frac{RT}{4}\ln\left(\frac{p_{O_2}^{(2)}}{p_{O_2}^{(1)}}\right) \quad . \tag{3.7}$$

Here, $\rho = R_{ext}/R_O$ is the ratio of the resistance in the external circuit and the internal oxide ion conductor. For an infinetely fast electronically conducting circuit (i.e. short circuit conditions), $\Delta\eta_e$ reduces to zero. Conversely, if the the external circuit has infinitely high resistance ($R_{ext} \gg R_O$), $\Delta\eta_e$ is represented by the open circuit voltage of the system. If the oxygen potential gradient was replaced by an applied voltage over the sample ($U_{applied}$), then $\Delta\eta_e = -F \cdot U_{applied}$. When Equations 3.5 to 3.7 are coupled with proper defect chemistry, the demixing equation may be analytically integrated to yield the cation distribution. For the sake of simplicity, I will use an acceptor doped binary oxide AO_2 (+ B_2O_3)[11] to derive the distribution of dopants (B^{3+}) at steady state for a membrane exposed to an oxygen potential gradient. Firstly, let us examine the chemical potential gradient for element B, as shown by Martin [53]:

$$\nabla\mu_B = RT\frac{3}{2}\frac{4-2x_B}{4-x_B}\nabla\ln x_B - \frac{3}{4}RT\nabla\ln(p_{O_2}) \quad . \tag{3.8}$$

---

[10] This, in a first approximation, could also be generalized for a pure membrane setup where both electrons and oxide ions are transported through the membrane interior, if we approximate that the two conduction paths are independent (which they in reality are not).

[11] Typical example here is yttrium stabilized zirconia.

From Equation 3.8, it is clear that there are two driving forces for mass transport. Initially, the oxide is homogeneous ($\nabla \ln \mathrm{x_B} = 0$) and only the oxygen potential gradient induces mass transport. However, if there is a difference in mobility between the cations, an additional driving force due to the induced concentration gradient is introduced. The steady state distribution of element *B* can be obtained from proper integration of the demixing equation after Equations 3.7 and 3.8 are incorporated [54]:

$$\begin{aligned} 2\left(\frac{3}{4}-\gamma\right)\ln\left(\frac{4-x_B^{(2)}}{4-x_B^{(1)}}\right)-\gamma\ \ln\left(\frac{1-x_B^{(2)}}{1-x_B^{(1)}}\right)+\frac{3}{2}\ln\left(\frac{x_B^{(2)}}{x_B^{(1)}}\right) \\ =\left(\frac{3}{4}-\gamma\right)\frac{1}{1+\rho}\ln\left(\frac{p_{\mathrm{O_2}}^{(2)}}{p_{\mathrm{O_2}}^{(1)}}\right)\ . \end{aligned} \tag{3.9}$$

From Equation 3.9 we can deduce that there will be an accumulation of B on the high $p_{\mathrm{O_2}}$ side when $\gamma = \frac{D_\mathrm{A}}{D_\mathrm{B}} > \frac{3}{4}$, and a corresponding depletion if the ratio is below ¾. The critical value of $\gamma = \frac{3}{4}$ can be recognized as the charge ratio $z_\mathrm{B}/z_\mathrm{A}$, which underlines the fact that kinetic demixing is an electrotransport phenomenon. In Figure 3.2, steady state demixing profiles for the example oxide calculated by Martin [54] are presented for different external oxygen partial pressures. As can be seen, even for a slight difference in cation diffusivity ($\gamma = 0.5$), there is a pronounced steady-state demixing profile. The distribution of B elements is asymmetric, which yields a narrow and highly B-enriched zone towards the high $p_{\mathrm{O_2}}$ side, with a broad slightly B-depleted zone towards the low oxygen potential side. It is important to remember that profiles such as the ones depicted in Figure 3.2 are steady-state profiles. In oxide-ion (and proton) conducting oxides, cation diffusion is typically very slow, and steady state is only reached in reasonable times, τ, for very thin membranes. For instance, if the diffusion coefficient for the slowest species is taken as $D = 10^{-14}$ cm^{2}s^{-1}, steady state is reached at $\tau = 15\,000$ years for a 1 mm thick membrane, but only $\tau = 1.5$ years for a 10 µm thick membrane. The latter is in the order of the desired operating times for commercial oxide ion conducting membranes. However, it should be emphasized that demixing and performance degradation during the transient time towards the steady state may also have large impact on the membrane performance and durability.

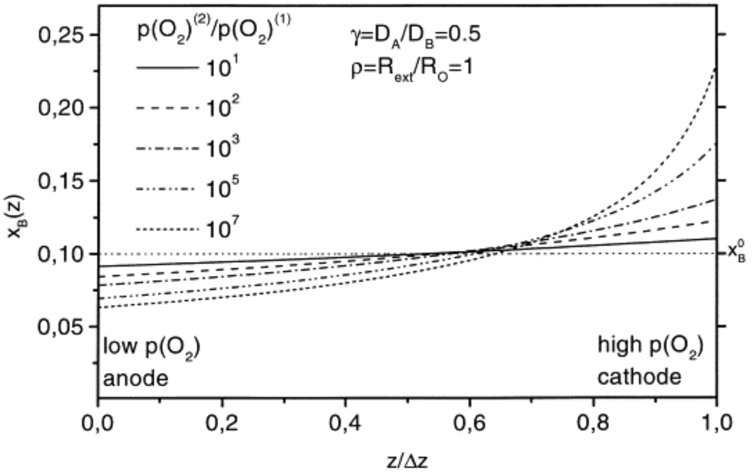

Figure 3.2. Calculated demixing profile for an acceptor doped binary oxide AO_2 ($+B_2O_3$) for different values of oxygen partial pressure ratios from [54]. Initial dopant fraction was set at $x_B = 0.1$.

3.3. Kinetic decomposition

As shown in the previous section, accumulation of the faster moving cation species will occur if there is a substantial difference between the cation diffusivities. In compounds with a narrow range of homogeneity (e.g. line compounds of ternary oxides), no demixing can take place even though the activity of one of the constituents increases at the high oxygen potential side. However, the single phase oxide may decompose into its binary oxides on either surface if the activity of a reactant exceeds unity, which leads to kinetic decomposition [52]. In the following treatment I will consider kinetic decomposition in a ternary oxide, ABO_3, where both cations are trivalent. By introducing the steady state flux equations and assuming local equilibrium, the chemical potential gradients of the reactant binary oxides and oxygen gas can be related, similarly as in the previous section:

$$D_{\mathrm{B}} \nabla \mu_{\mathrm{B_2O_3}} = D_{\mathrm{A}} \nabla \mu_{\mathrm{A_2O_3}} + \frac{3}{4} (D_{\mathrm{B}} - D_{\mathrm{A}}) \nabla \mu_{\mathrm{O_2}} \qquad (3.10)$$

By further introducing the Gibbs-Duhem relation for the binary A_2O_3- B_2O_3 system, and assuming that there is no gradient in the chemical potential of the parent ternary oxide, we obtain

$$\nabla \mu_{\mathrm{B_2O_3}} = -\nabla \mu_{\mathrm{A_2O_3}} \quad . \qquad (3.11)$$

With this relation, Equation 3.10 can be integrated and transformed to

$$\Delta \mu_{\mathrm{B_2O_3}} = \frac{3}{4} \cdot \frac{1-\gamma}{1+\gamma} \Delta \mu_{\mathrm{O_2}} \ , \qquad (3.12)$$

where γ still represents the ratio of the cation diffusivities ($\gamma = \frac{D_{\mathrm{A}}}{D_{\mathrm{B}}}$). Schmalzried [52] showed that the maximum difference $\Delta \mu_{\mathrm{B_2O_3}}$ that the original ABO_3 oxide could tolerate without decomposing could be estimated as

$$\Delta \mu_{\mathrm{B_2O_3}}^{\max} = -\Delta G_{\mathrm{T}}^{0} (\mathrm{ABO_3}) \quad , \qquad (3.13)$$

where $\Delta G_{\mathrm{T}}^{0} (\mathrm{ABO_3})$ is the standard Gibbs energy change at the experimental temperature (T) for the reaction $A_2O_3 + B_2O_3 = 2ABO_3$. Inserting Equation 3.13 into Equation 3.12, and introducing oxygen partial pressures, we obtain an expression for the critical partial pressure difference for kinetic decomposition

$$\ln\left(\frac{p_{\mathrm{O}_2}^{(2)}}{p_{\mathrm{O}_2}^{(1)}}\right)^{\mathrm{critical}} = -\frac{4}{3}\cdot\frac{1+\gamma}{1-\gamma}\times\frac{\Delta G_{\mathrm{T}}^{0}\,(\mathrm{ABO_3})}{\mathrm{RT}} \quad , \qquad (3.14)$$

where $p_{\mathrm{O}_2}^{(2)}$ and $p_{\mathrm{O}_2}^{(1)}$ again represent the high and low oxygen partial pressures, respectively. Firstly we can note that kinetic decomposition can occur even though ABO_3 is stable under both oxygen environments. Thus, decomposition is neither an oxidation nor reduction reaction. Both kinetic (cation diffusivities) and thermodynamic parameters ($\Delta G_{\mathrm{T}}^{0}$) influence the critical oxygen potential ratio the oxide can withstand without decomposition. For this oxide we can recognize that no decomposition can occur if γ is unity, which once again reflects the ratio of the cation charges, similarly as for kinetic demixing. For $\gamma < 1$ (B faster than A), accumulation and formation of B_2O_3 may occur on the higher oxygen potential side if the applied oxygen potential gradient is high enough.

Cebasek *et al*. [55] derived a decomposition diagram for the Ruddlesden Popper phase La_2NiO_4 to illustrate the correlation between the critical oxygen potential gradient and the diffusivity ratio, as shown in Figure 3.3. We can immediately recognize the critical diffusivity ratio 2/3 as the ratio between the cation charges of Ni^{2+} and La^{3+}.

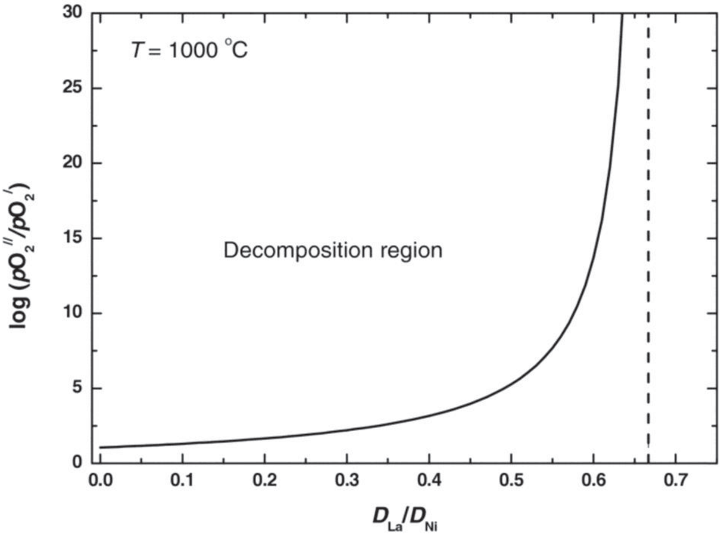

Figure 3.3. Decomposition diagram for the Ruddlesden-Popper phase La_2NiO_4 from [55]

3.4. Morphological instability

So far, the treatment of degradation phenomena in oxides exposed to oxygen potential gradients have been restricted to strictly one-dimensional transport under the assumption that the initial planar and parallel surfaces are morphologically stable. However, as there is a net mass transport towards the high oxygen potential side, the morphology on the surfaces may change during operation. Martin and Schmalzried [56] have shown that the low oxygen potential side of a CoO single crystal becomes unstable due to pore formation during exposure to an oxygen potential gradient. The high oxygen potential side was found to remain relatively stable. These findings were confirmed by linear stability analysis which showed that the oxidizing surface is always morphologically stable, while the reducing surface should eventually transform to a non-planar wavelike surface. These effects also explain why true steady state situations for demixing are difficult to achieve experimentally, as the diffusion problem departs from the one-dimensional situation assumed in the derivation.

The assumption of a perfectly stable oxidizing surface is also based on strict assumptions regarding the model oxide [52]. If there are pores already present in the bulk of the oxide, these will act as short-circuits for oxygen if we assume that they contain small amounts of oxygen gas. Thus, the oxidation and reduction reactions in Equation 3.2 formulated for the oxide surfaces can also take place on the pore surfaces. Now considering that the pore essentially is a negative crystal, reduction will occur on the pore surface pointing towards the high p_{O_2} side, while oxidation will take place on the pore surface closer to the more reducing side. Accordingly, the pore will drift towards the more oxidizing side. It has been shown for spherical pores that the pore velocity is independent of pore volume and three times larger than the crystal velocity. As a consequence, pores should over time reach the high p_{O_2} surface and destroy the morphologically stable planar surface.

3.5. Proton conducting oxides exposed to a hydrogen potential gradient

Until now, the theoretical treatment has been restricted to oxides exposed to an oxygen potential gradient, which is directly relevant for electrolytes in fuel cell applications and oxygen transport membrane for oxygen separation. With the introduction of the hydrogen species into the system, present in the hydrogen transport membrane material as protons, we are introducing an additional thermodynamic variable; the chemical potential of hydrogen. Thus, our model oxide system is now described as ABO_3+H, and the Gibbs-Duhem equation expands to

$$x_{\mathrm{A}}\nabla\mu_{\mathrm{A}} + x_{\mathrm{B}}\nabla\mu_{\mathrm{B}} + x_{\mathrm{O}}\nabla\mu_{\mathrm{O}} + x_{\mathrm{H}}\nabla\mu_{\mathrm{H}} = 0 \quad . \qquad (3.15)$$

Proton conductors are in their applications typically exposed to gradients in the chemical potential of hydrogen, in the form of different hydrogen partial pressures on the membrane surfaces. Such a gradient will, in most cases, induce a gradient in the oxygen partial pressure as well. In the previous treatment for oxides exposed to an oxygen potential gradient, opposite gradients in the cation potentials were induced as a result of the Gibbs-Duhem relation. In the case for hydrogen potential gradients over proton conducting membranes, the situation is slightly more complex.

Re-arrangement of Equation 3.15 shows that a net gradient in the cation potentials will only occur if the summation of the hydrogen and oxygen term is non-zero:

$$x_{\mathrm{A}}\nabla\mu_{\mathrm{A}} + x_{\mathrm{B}}\nabla\mu_{\mathrm{B}} = -(x_{\mathrm{O}}\nabla\mu_{\mathrm{O}} + x_{\mathrm{H}}\nabla\mu_{\mathrm{H}}) \ . \tag{3.16}$$

Let us expand this discussion to discover under what circumstances the net cation potential gradient will indeed be zero, i.e. $x_{\mathrm{O}}\nabla\mu_{\mathrm{O}} + x_{\mathrm{H}}\nabla\mu_{\mathrm{H}} = 0$. Now we start by expressing the chemical potentials in terms of their gaseous species:

$$\frac{1}{2}x_{\mathrm{O}}\nabla\mu_{\mathrm{O}_2} + \frac{1}{2}x_{\mathrm{H}}\nabla\mu_{\mathrm{H}_2} = 0 \tag{3.17}$$

This may still seem a bit elusive as to the input conditions for an operating proton conducting membrane, where it is more common to have preset water vapour partial pressures rather than oxygen partial pressures. Thus, we introduce the equilibrium reaction between water vapour, hydrogen and oxygen, and the relation between the chemical potential gradients:

$$\frac{1}{2}\nabla\mu_{\mathrm{O}_2(\mathrm{g})} = \nabla\mu_{\mathrm{H}_2\mathrm{O}(\mathrm{g})} - \nabla\mu_{\mathrm{H}_2(\mathrm{g})} \tag{3.18}$$

The zero cation potential gradient condition in Equation 3.17 may now be expressed in terms of hydrogen and water vapour gradients:

$$2x_{\mathrm{O}}\left(\nabla\mu_{\mathrm{H_2O(g)}} - \nabla\mu_{\mathrm{H_2(g)}}\right) + x_{\mathrm{H}}\nabla\mu_{\mathrm{H_2(g)}} = 0 \tag{3.19}$$

Further rearrangement yields an expression for the zero cation gradient condition in terms of the water vapour gradient and the molar fractions of hydrogen and oxygen atoms:

$$\nabla\mu_{\mathrm{H_2O(g)}} = \left(1 - \frac{x_{\mathrm{H}}}{2x_{\mathrm{O}}}\right)\nabla\mu_{\mathrm{H_2(g)}} \tag{3.20}$$

A strict thermodynamic treatment of this relation requires correct determination of the thermodynamic factors for hydrogen and oxygen site fractions, which will not be covered here. However, in general, the site fraction of hydrogen in proton conducting oxides is much lower than for oxygen. Thus, Equation 3.20 states that if the imposed water vapour gradient is equal to the hydrogen gradient over an oxide with dilute concentrations of protons, no net cation gradient is expected. Or formulated conversely; there are only a few particular cases in which an imposed hydrogen partial pressure gradient *does not* induce a gradient in the cation chemical potentials.

4. Methodology

In this chapter, I will provide supplementary descriptions of the experimental methods used in Manuscripts I-IV. I will first describe some of the more advanced instrumentation before an in-depth description of the hydrogen permeation measurement setup is provided. Finally, I will present the mathematical interpretations of cation diffusion data used in Manuscripts III and IV.

4.1. Pulsed Laser Deposition

Pulsed Laser Deposition (PLD) was used to deposit thin films of LWO and NWO (Manuscripts I and IV, respectively). In the following, a more detailed description of the deposition process and the involved parameters is provided.

PLD is, in essence, a physical vapour deposition method where the energy source is located outside of the deposition chamber. As the name indicates, a high-power pulsed laser beam is focused inside a deposition chamber to strike a target material with the desired composition of the film [57]. The high energy laser focused on a small area (< 1 cm^2) vaporizes parts of the material from the target into a plasma plume, which subsequently deposits on the substrate typically located parallel to the target within a distance of 4-10 cm. The deposition chamber can be either ultra-high vacuum (for elemental and alloy compounds) or containing a background gas such as oxygen to fully oxygenate an oxide film.

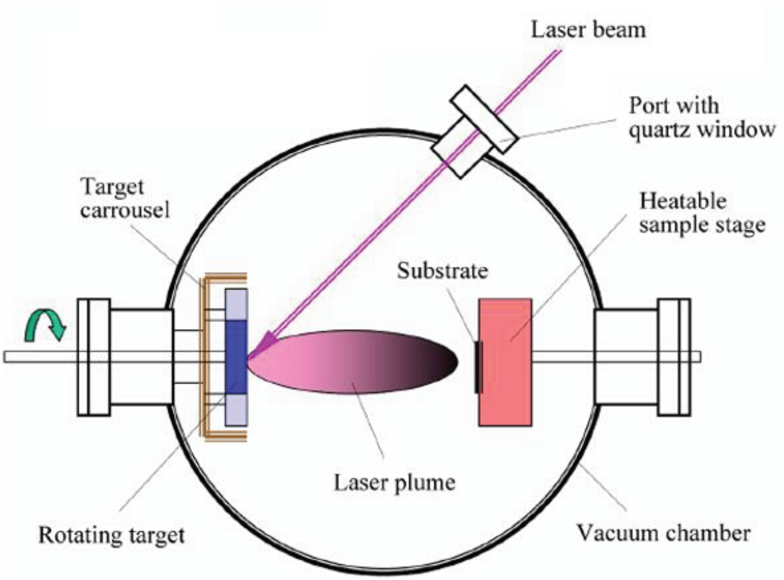
Laser beam
Port with quartz window
Target carrousel
Heatable sample stage
Substrate
Laser plume
Rotating target
Vacuum chamber

Figure 4.1. Schematic of the PLD instrumentation taken from [57].

The PLD process is simple in its design and setup, but the physical phenomena governing the deposition process are quite complex. Firstly, the laser ablation and the development of the plasma plume is a high energy process that occurs at and near the target surface at non-equilibrium. The bulk material at the target surface (10 nm penetration depth is typical) is vaporized simultaneously due to the high electric field generated by the focused beam. Thus, all target components evaporate at the same time, irrespective of their individual binding energies. The evaporated components form a dynamic plasma plume with a velocity normal to the target surface directed towards the substrate. The plume shape and density may influence the morphology and sputtering rate of the deposited film, and depend heavily on the background pressure. Increased background pressure increases the scattering of the high energy particles effectively decreasing the deposition rate, whereas almost all particles reach the substrate in ultra-high vacuum [58].

The quality and microstructure of the deposited film is strongly influenced by the nucleation process and growth kinetics on the substrate surface. These processes may be controlled by manipulating the energies of the incoming particles, the density of the plasma plume, substrate temperature and surface morphology as well as background pressure. Thus, it is possible to obtain a wide variety of different nucleation and growth characteristics of the deposited film, leading to large variations in morphology and strain in the films. Moreover, the varied background pressure allows for deposition of both stoichiometric and non-stoichiometric oxides by varying the oxygen pressure during deposition.

A main advantage of the PLD technique is the high inherent density of the deposited films, making it possible to deposit dense, uniform and thin films on porous substrates. This is due to an effect called *supersaturation*, which occurs on the substrate during the pulse duration [58]. Supersaturation causes large nucleation densities on the surface, which increase the smoothness of the film compared to other physical vapour deposition methods.

In manuscripts I and V, PLD was used to deposit thin films (0.2-5 μm) of lanthanide tungsten oxides. Figure 4.2 presents some examples of deposited lanthanum tungsten oxide films on various substrates: Columnar-like structures, typical of so-called *3D growth kinetics* in which a nucleation island forms on top of a previously formed island, yielding columnar growth. Figure 4.2 b and c are examples of dense films deposited on a porous substrate. The presence of particulates formed during the deposition process is visible on the surface of the films. These large particles are difficult to avoid in a PLD process, and tend to disrupt the uniform and dense film. Shadowing effects along the edges of these particles are major sources of pinholes and defects in the films.

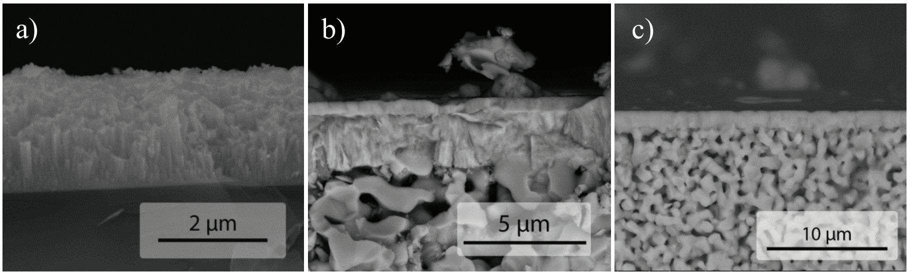

Figure 4.2. Example SEM images of LWO thin films deposited by PLD onto (a) Si and (b, c) porous LWO substrates.

4.2. Time-of-Flight Secondary Ion Mass Spectroscopy

The chemical tracer diffusion profiles in manuscript IV were obtained by Time-of-Flight Secondary Ion Mass Spectroscopy, ToF-SIMS (ION-TOF GmbH, Münster, Germany). The instrument was described in detail by De Souza *et al*. [59] and consists of five main components, illustrated in Figure 4.3: The sputtering ion gun is used exclusively for removal of sample material, and is a high current, low energy dual source column with a Cs^+ thermal ionization source and an electron impact source used to create O_2^+ and Xe^+ beams. The Ga^+ Liquid Metal Ion Gun (LMIG) is used to create secondary ions for analysis. For poorly conducting samples, the surface is flooded with >20 eV electrons to avoid charging effects during ion bombardment. The generated secondary ions are extracted perpendicular to the sample surface via the extraction electrode and into the ToF column. Here, the secondary ions are separated based on their velocity, which is given by the mass/charge ratio. However, the emitted ions can have different energies even if they have the same mass, which would lead to a range of velocities for ions with the same mass. The reflectron, an electrostatic mirror, corrects for the spread in velocities and ensures that ions of the same mass but different energies arrive at the detector simultaneously. Depth profiling with a ToF-SIMS is obtained by interlacing the cycles of sputtering and analysis bombardment, and recording complete mass spectra continuously.

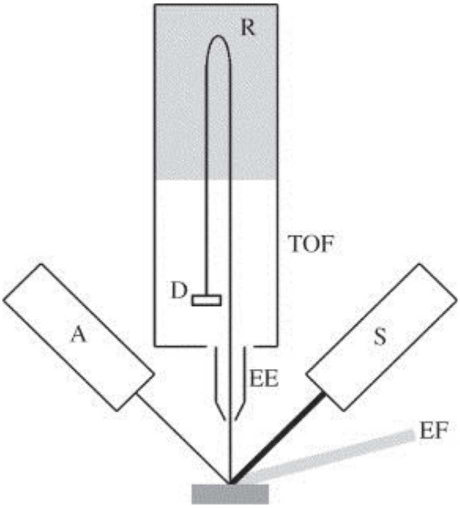

Figure 4.3. Schematic illustration of ToF-SIMS instrumentation [59]. Two ion guns, Ga^+ for analysis (A) and low energy for sputtering (S), are directed at the sample, with an extraction electrode (EE) leading the secondary ions into the time of flight mass spectrometer (TOF) which contains a reflectron (R) and a detector (D). An electron flood (EF) is provided to counteract charging effects [59].

4.3. Electron MicroProbe Analysis

An electron microprobe (EMP) is essentially an electron microscope designed for non-destructive x-ray microanalysis and imaging, typically used to determine the chemical composition of small volumes of a solid material. It functions similarly to a scanning electron microscope; the sample is bombarded with an electron beam, and the emitted x-rays characteristic of the compound elements are analysed. The electron microprobe is typically equipped with both energy-dispersive (EDS) and wavelength-dispersive (WDS) spectrometers, where the former is good for quick qualitative analysis. WDS, on the other hand, may provide proper quantitative elemental analysis of almost all chemical elements. In this work, a Cameca SX100 with 5 WDS detectors individually calibrated to one particular element was used, allowing simultaneous analysis of up to five elements at a time. The detection limit for this instrument is in the order of 100-1000 ppm, and the analytical sensitivity is <0.5 % for major matrix elements. Typical analysis volumes are in the order of 1 μm^3.

4.4. Hydrogen permeation measurements

Manuscript II presents hydrogen flux measurements on LWMo membranes as a function of temperature, Δp_{H_2} and Δp_{H_2O}. Figure 4.4 illustrates schematically the experimental setup for the hydrogen flux measurements, conducted in a Probostat^{TM} (NorECs, Norway) measurement cell. The membrane was mounted on top of an alumina support tube, held in place with an alumina spring load. A gold gasket was placed between the alumina support tube and the sample for sealing purposes. A platinum ring with the same diameter as the gold gasket was inserted between the membrane and the spring load, to ensure that the spring force was evenly distributed towards the gold gasket. Sealing was achieved by gradual heating towards the melting temperature of gold, while monitoring the leak rate of helium into the permeate exhaust from a helium-rich feed gas composition. The gas compositions in the permeate gas stream was analysed by a 3000 plus Agilent Micro-Gas Chromatograph (μGC), calibrated specifically for H_2 and He at low concentrations.

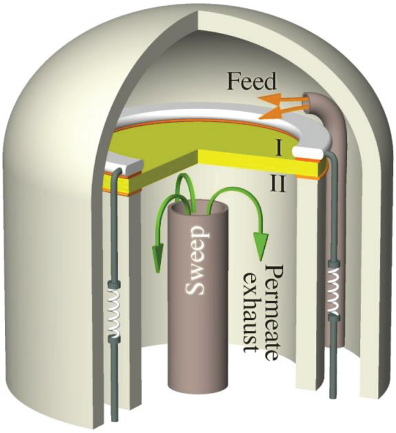

Figure 4.4. Schematic illustration of the experimental setup for hydrogen permeation measurements

Hydrogen permeation experiments were conducted by setting up a gradient in hydrogen partial pressure and measuring the amount of hydrogen in the permeate exhaust. Potential leaks through the sealing gasket, support tube and potential pores in the sample were determined by supplying a known amount of helium in the feed gas composition and monitoring the He concentrations in the permeate exhaust. The sweep inlet gas was wet ($p_{\mathrm{H_2O}} = 0.028$ atm) or dry ($p_{\mathrm{H_2O}} \approx 3 \times 10^{-5}$ atm [60]) argon. Thus, assuming macroscopic leakage, the measured amounts of hydrogen and helium can be converted to hydrogen fluxes as

$$j_{\mathrm{H_2}} = \frac{c_{\mathrm{H_2}} - \frac{p_{\mathrm{H_2}}}{p_{\mathrm{He}}} c_{\mathrm{He}}}{A} \times Q \ . \tag{4.1}$$

$c_{\mathrm{H_2}}$ and c_{He} are concentrations obtained from the µGC, and can be considered equivalents to partial pressures in the permeate exhaust. The ratio $\frac{p_{\mathrm{H_2}}}{p_{\mathrm{He}}}$ reflects the inlet partial pressure ratio in the feed gas stream. A is the active membrane area given by the inner diameter of the gold gasket, and *Q* is the volumetric flow rate of the permeate exhaust gas. Herein, it is assumed that the leak rates of He and H_2 are directly proportional to feed side partial pressures. It is essential to keep the leakage at a minimum to avoid errors in the calculation, as these assumptions are based on a pure macroscopic leakage mechanism.

It is important to maintain a controlled and constant feed gas composition that is not influenced by the permeation through the membrane. Thus, it is common to use relatively high flow rates on the feed side, and ensure that the measured hydrogen permeation is independent on the feed side flow rate. In the measurements on LWMo, the feed flow rate was kept at 25 mL min^{-1}. Similarly, it is important to verify that the measured hydrogen flux is independent of sweep side flow rate. If the flow rate is kept too low, build-up of double layers near the permeate side surface of the membrane will influence both the effective driving force and the surface kinetics at the solid-gas interface. Conversely, if the sweep flow rate is too high, the hydrogen permeated through the membrane may yield concentrations in the sweep gas below the detection limit of the μGC.

4.5. Cation diffusion measurements

Two types of cation diffusion measurements have been implemented in this work; cation inter-diffusion and chemical tracer diffusion. Specific experimental details are provided in manuscripts III and IV. In this section, I will thus focus on the fundamental principles of the two experimental methods and mathematical interpretations of the obtained concentration profiles for both bulk and grain boundary diffusion.

4.5.1 Inter-diffusion

In an inter-diffusion study, two single crystal or polycrystalline samples with different composition are placed in contact with each other and annealed for a specific time long enough to obtain a measurable compositional profile across the original phase boundary. In inter-diffusion studies such as for LWO, where the primary aim is to obtain a fundamental insight into the diffusion properties of the slow cation species, it is common to choose diffusion couples of the form ABO_3-$A'BO_3$, where ABO_3 and $A'BO_3$ retain a similar crystal structure and defect chemistry. For the studies of lanthanum site diffusion in LWO, $Nd_{27}W_{1.5}O_{55.5}$ (NWO) was chosen as the second part of the diffusion couple, as NWO crystallizes in the same fluorite-related cubic structure as LWO. Moreover, Nd^{3+} and La^{3+} have similar chemical properties and should as such diffuse similarly through the same crystal lattice.

When the inter-diffusion coefficient can be considered composition-independent, the concentration profiles will be symmetrical around the original phase boundary. Figure 4.5 presents a typical concentration profile for the LWO-NWO inter-diffusion couple.

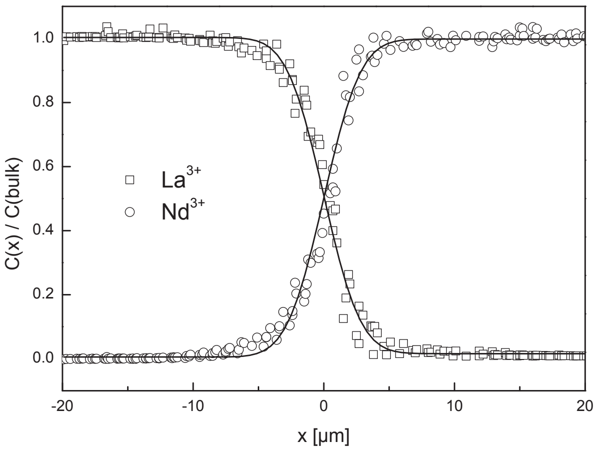

Figure 4.5. Normalized inter-diffusion concentration profiles for LWO-NWO annealed at 1300 °C for 300 hours in pressurized air.

4.5.2 Chemical tracer diffusion

Chemical tracer diffusion experiments were conducted on LWO with Nd^{3+} and Mo^{6+} as tracer cations for La^{3+} and W^{6+}, respectively. Thin films (~60-100 nm) of NWO were deposited on dense polished pellets of LWO using PLD and subsequently annealed at various temperatures and annealing times in air and 5 % H_2 95 % Ar. The complete experimental procedure was conducted in the following manner:

1. High density LWO pellets (> 97 % rel. density) were prepared and polished using SiC grit paper and diamond dispersion to a surface roughness of 20-40 nm, as inspected by light interference microscopy.

2. The prepared pellets were subsequently subjected to a pre-annealing procedure under the same p_{O_2} and temperature as the planned diffusion anneal for twice as long.
3. A thin film of NWMO was deposited on the highly polished side of the specimen by PLD, with a substrate temperature of 600 °C.
4. The coated specimen was then sectioned in two. One part was kept as a "zero-time" reference, whereas the second part was used for the diffusion annealing procedure.
5. Both sections of the sample were then investigated by ToF-SIMS analysis to obtain zero-time and diffusion profiles.

4.6. Mathematical treatment of diffusion profiles

The mathematical treatment of the experimentally obtained diffusion profiles consists of solving the diffusion equation for the appropriate boundary conditions of the specific experimental design. If the diffusion coefficient can be considered constant, analytical solutions are available, as described by Crank [61], while more rigorous mathematical treatments are necessary if the diffusion coefficient varies with time and position in the diffusion zone.

Both the chemical tracer diffusion and inter-diffusion experiments represent, in principle, chemical diffusion and should, as such, have composition-dependent diffusion coefficients. However, as the diffusion profile of interest in the tracer diffusion experiment is only within the diffusion medium itself, with only minor relative composition changes, it is common to assume constant diffusivity through the entire diffusion zone. For inter-diffusion, the diffusion profile extends over two phases. The chemical inter-diffusion coefficient will reflect a weighted sum of the individual tracer diffusion coefficient, as represented by the Darken equation (Eq. 2.38). If the two phases display significantly different diffusivities, the chemical inter-diffusion coefficient will have a composition-dependence. Thus, it is common to design inter-diffusion experiments such that both phases in the diffusion couple are similar in regards to both crystal structure and defect chemistry, such that both tracer diffusion coefficients can be assumed similar.

4.6.1 Inter-diffusion with constant diffusivity

The mathematical treatment of the experimentally obtained diffusion profiles consists of solving the diffusion equation for the appropriate boundary conditions of the specific experimental setup. The inter-diffusion experiments have initial boundary conditions as

$$\begin{aligned} c = c_{\mathrm{I}} \quad &\text{for} \quad (x < 0,\ t = 0) \\ c = c_{\mathrm{II}} \quad &\text{for} \quad (x > 0,\ t = 0)\,. \end{aligned} \tag{4.2}$$

Here, $x = 0$ at the initial phase boundary, and c_{I} and c_{II} represent the initial concentrations of the diffusing species in the two phases that comprise the diffusion couple. For the inter-diffusion experiments, the diffusion couple can be considered as consisting of two semi-infinite media where at $t > 0$ there is always a limiting value x_∞ for which

$$\begin{aligned} c = c_{\mathrm{I}} \quad &\text{for} \quad (x < x_\infty,\ t > 0) \\ c = c_{\mathrm{II}} \quad &\text{for} \quad (x > x_\infty,\ t > 0)\,. \end{aligned} \tag{4.3}$$

These boundary conditions imply that the diffusion profile does not penetrate the outer surfaces of the diffusion couple. Given these boundary conditions, the solution to the diffusion equation can be found analytically, as shown in the theoretical review by Crank [61]:

$$c(x,t) = \frac{c_{\mathrm{I}} - c_{\mathrm{II}}}{2}\,\mathrm{erfc}\left(\frac{x}{2\sqrt{\widetilde{D}t}}\right) + c_{\mathrm{II}} \quad , \tag{4.4}$$

where ‘erfc’ is the error function complement ($\mathrm{erfc}\, z = 1 - \mathrm{erf}\ z$).

Figure 4.6 shows schematically the evolution of the diffusion profiles of La and Nd during inter-diffusion between LWO and NWO assuming a constant inter-diffusion coefficient. As can be seen, the concentration profiles are symmetric around the initial phase boundary ($x = 0$).

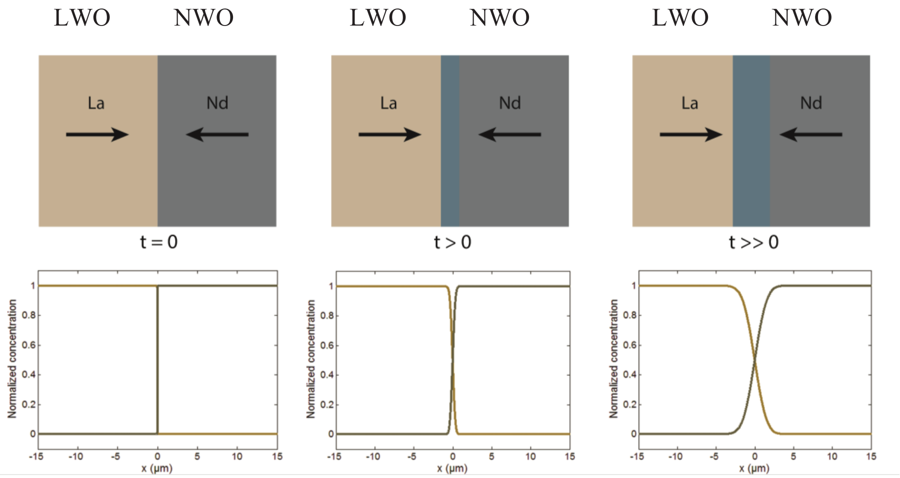

Figure 4.6. Schematic illustration of the evolution of concentration profiles during inter-diffusion for a composition-independent diffusion coefficient.

4.6.2 Chemical tracer diffusion with constant diffusivity

For the chemical tracer diffusion experiments, a finite tracer source (thin film of thickness h) was deposited on the surface of an essentially infinite diffusion medium (bulk polycrystalline pellet). Thus, at time $t = 0$, the initial boundary conditions are

$$\begin{aligned} c^* &= c^*_{\mathrm{I}} \quad \text{for} \quad (h \geq x > 0,\ t = 0) \\ c^* &= c^*_{\mathrm{II}} \quad \text{for} \quad (x > h,\ t = 0)\,. \end{aligned} \tag{4.5}$$

Here, c^*_{I} and c^*_{II} denote the initial tracer concentrations in the source and in the diffusion medium, respectively. Given these initial conditions, the diffusion equation can be solved analytically as

$$c^*(x,t) = \frac{c^*_{\mathrm{I}} - c^*_{\mathrm{II}}}{2}\left\{\mathrm{erf}\left(\frac{x+h}{2\sqrt{D^*t}}\right) - \mathrm{erf}\left(\frac{x-h}{2\sqrt{D^*t}}\right)\right\} + c^*_{\mathrm{II}} \quad , \tag{4.6}$$

commonly referred to as the *thick-film solution* to Fick’s second law. If the amount of tracer which diffuses into the diffusion medium is relatively small as compared to the concentration in the tracer source, the surface concentration can be considered constant ($c^* = c^*_{\mathrm{I}},\ x = h,\ t > 0$), and the analytical solution reduces to

$$c^*(x,t) = (c^*_{\mathrm{I}} - c^*_{\mathrm{II}})\ \mathrm{erfc}\left(\frac{x-h}{2\sqrt{D^*t}}\right) + c^*_{\mathrm{II}} \quad , \tag{4.7}$$

for $x \geq h$.

In many instances the thick-film solution cannot accurately describe the observed diffusion profiles of typical radiotracer experiments. If the boundary conditions

$$\begin{aligned} c^* &= c^*_{\mathrm{I}} \quad \text{for} \quad (x = 0,\ t > 0) \\ c^* &= 0 \quad \text{for} \quad (x > 0,\ t = 0)\,. \end{aligned} \tag{4.8}$$

are met, the semi-infinite medium solution is applied. Here, $x = 0$ at the phase boundary between the tracer source and the semi-infinite medium. Thus the concentration profile can be described similarly as the inter-diffusion profiles:

$$c^*(x,t) = c_{\mathrm{I}}^* \operatorname{erfc}\left(\frac{x}{2\sqrt{D^* t}}\right) , \tag{4.9}$$

If none of these boundary conditions are met when examining the diffusion profiles, the diffusion problem can be solved by implementing the *plane source* solution to the diffusion equation

$$c^*(x,t) = K \exp\left(-\frac{x^2}{4D^* t}\right) . \tag{4.10}$$

4.6.3 Inter-diffusion with composition-dependent diffusivity

The most common approach for solving the concentration dependent inter-diffusion problem is called the *Boltzmann-Matano* method. One important prerequisite for solving the *Boltzmann-Matano* equation is to determine the *Matano* plane, x_M, defined as the plane across which an equal number of atoms have crossed in both directions;

$$\int_{-\infty}^{x_M} [c(\mathrm{x}) - c_{\mathrm{L}}]\mathrm{d}x = \int_{x_M}^{\infty} [c_{\mathrm{R}} - c(\mathrm{x})]\mathrm{d}x \quad . \tag{4.11}$$

The *Matano-plane* is not possible to determine *a priori*, but must rather be determined from experimental concentration-distance profiles using Equation 4.11 [62]

Having established the *Matano-plane* properly, the *Boltzmann-Matano equation* can be solved as

$$\widetilde{D}(c_x) = \frac{1}{2t} \frac{\int_{c_\mathrm{L}}^{c_x} (x - x_\mathrm{M}) \mathrm{d}C}{(\mathrm{d}C/\mathrm{d}x)_{C_x}} \ . \tag{4.12}$$

From Equation 4.12, the chemical inter-diffusion coefficient can be determined for any concentration c_x from an experimental concentration-distance profile. However, it can be difficult to accurately determine the integral and derivative in the *Boltzmann-Matano* equation in inter-diffusion systems with narrow diffusion profiles and limited data points due to space-resolution limitations of the EPMA analysis. Thus, it is common to fit the experimental data to a non-physical mathematical function that reproduces the data accurately [63]. In Manuscript III, a cubic spline function was implemented and fitted to the experimental data. Using this function, the concentration profiles can be repopulated with a higher point density, allowing for easier analysis of the integral and derivative in Equation 4.12. It should be mentioned that both the determination of the *Matano*-plane and the repopulation of the concentration profile can introduce additional errors in the analysis.

4.6.4 Grain boundary diffusion

Cation diffusion in polycrystalline oxides can be transported through the bulk grains of the material and along the grain boundaries. Grain boundary transport is a two-dimensional diffusion problem, involving enhanced diffusion along the interphase and lateral diffusion into the adjoining bulk material. The diffusion problem does not have an analytical solution for the boundary conditions in inter-diffusion and tracer diffusion studies. However, Whipple derived an exact solution in integral form [64] which was later transformed to an approximate analytical solution by Le Claire [65]. It is based on defining two dimensionless parameters β and η as

$$\beta = \frac{\omega \cdot D_{\mathrm{gb}}}{D_{\mathrm{bulk}}^{3/2} \cdot t^{1/2}} \quad , \tag{4.13}$$

$$\eta = \frac{x}{\sqrt{D_{\mathrm{bulk}} t}} \quad . \tag{4.14}$$

Here D_{gb} and D_{bulk} are the grain boundary and bulk diffusion coefficients, respectively, ω is the grain boundary width and t is the diffusion time. In the analysis it is assumed that $D_{\mathrm{gb}}/D_{\mathrm{bulk}} \gg 1$. Empirical analysis revealed a relation between the concentration profile and the two diffusion coefficients as

$$s \cdot \omega \cdot D_{\mathrm{gb}} = 1.322 \sqrt{\frac{D_{\mathrm{bulk}}}{t}} \left(-\frac{\mathrm{d} \ln \bar{c}}{\mathrm{d}\eta^{6/5}} \right)^{-5/3} \quad . \tag{4.15}$$

s represents the segregation factor which is commonly assumed unity. Thus, the grain boundary diffusion coefficient can be obtained by the slope in a plot of logarithmic concentration versus $\eta^{6/5}$, when the bulk diffusion coefficient is established. The Whipple-Le Claire solution is only valid for $\beta \geq 10$ and $\eta/\sqrt{\beta} \geq 2$, which in practice means the deeper parts of a diffusion profile. Thus, for shorter penetration depths typical for high resolution analysis instrumentation such as SIMS, Chung and Wuensch developed an improved analytical solution [66]:

$$s \cdot \omega \cdot D_{\mathrm{gb}} = D_{\mathrm{bulk}}^{3/2} \cdot t^{1/2} \left[10^{A} \left(-\frac{\mathrm{d} \ln \bar{c}}{\mathrm{d}\eta^{6/5}} \right)^{B} \right] \quad . \tag{4.16}$$

Here, the fitting parameters A and B are tabulated values from Chung and Wuensch [66] for specific ranges of the slope $\frac{\mathrm{d} \ln \bar{c}}{\mathrm{d}\eta^{6/5}}$. Equation 4.16 is valid for $6 \geq \eta \geq 10$, and $1 \geq \beta \geq 10^5$, and can therefore be used for shorter diffusion times than the Whipple-

Le Claire solution. The Chueng Wuensch approach was used in Manuscript IV to describe grain boundary diffusion of Nd in LWO determined by SIMS analysis.

5. Manuscripts

Manuscript I

Fabrication, structural and electrical characterization of lanthanum tungstate films by pulsed laser deposition

Einar Vøllestad, Agnieszka Gorzkowska-Sobas and Reidar Haugsrud

Thin Solid Films, 520 (2012), 6531-6534

Manuscript II

Hydrogen permeation characteristics of $La_{27}Mo_{1.5}W_{3.5}O_{55}$.

Einar Vøllestad, Camilla Vigen, Anna Magrasó and Reidar Haugsrud

Manuscript III

Inter-diffusion in lanthanum tungsten oxide

Einar Vøllestad, Truls Norby and Reidar Haugsrud

Solid State Ionics, 244 (2012), 57-62

Manuscript IV

Chemical tracer diffusion of Nd and Mo in lanthanum tungsten oxide

Einar Vøllestad

Manuscript V

Interpretation of defect and gas-phase fluxes through mixed-conducting ceramics using Nernst-Planck-Poisson and Integral formulations

Einar Vøllestad, Huayang Zhu and Robert J. Kee

Accepted for publication in the Journal of the Electrochemical Society

Interpretation of defect and gas-phase fluxes through mixed-conducting ceramics using Nernst–Planck–Poisson and Integral formulations

Einar Vøllestad[a], **Huayang Zhu**[b], **Robert J. Kee**[b,*]

[a]Department of Chemistry, University of Oslo, Oslo, Norway
[b]Mechanical Engineering, Colorado School of Mines, Golden, CO 80401, USA

Abstract

This paper derives and demonstrates two models to represent defect transport through mixed-conducting ceramic membranes. The Nernst–Planck–Poisson (NPP) model is more general, but requires the computational solution of a boundary-value problem on a mesh network. The Integral method relies on more assumptions, but defect fluxes can be evaluated analytically based upon material properties and gas-phase composition at the membrane surfaces. Using examples based upon yttrium-doped barium zirconate, the two approaches are compared quantitatively. Under many circumstances the models deliver quantitatively similar results, but for situations where the membrane is exposed to large and/or multiple partial-pressure gradients, the predicted fluxes can deviate. The variations are the result of different physical assumptions and mathematical simplifications that are being used in the two models.

Keywords:
Mixed-conducting ceramics, Nernst–Planck–Poisson, Nernst–Planck integrals, Charged-defect transport, Barium zirconate

1. Introduction

The primary objective of this paper is to explore and interpret the quantitative relationships between alternative approaches to model defect fluxes within, and effective gas fluxes through, mixed conducting ceramic membranes. Modeling transport processes within mixed ionic-electronic conducting (MIEC) ceramics has primarily followed two approaches. One is based upon Ambipolar diffusion, which permits analytic solutions for the steady-state and transient conditions [1, 2]. However, the approach is limited to two mobile charge carriers. The second is based upon integrals of the Nernst-Planck equations [3–6]. This approach permits analytic solutions, but is also limited by assumptions. A third approach is based upon a Nernst-Planck-Poisson (NPP) formulation, which is more general than the other two. However, the NPP models do not permit analytic solutions and must be solved computationally. Although the general NPP formulation is well established and used in other settings [7–16], it has found only infrequent application in proton- and mixed-conducting ceramic membranes [17].

All the approaches share a common starting point – the Nernst–Planck equation, expressing the flux of charged defects as functions of concentration and electrostatic–potential gradients. As implemented here, the approaches also share some common assumptions. The most significant assumption is that the defect chemistry at the gas-membrane interfaces remains in chemical equilibrium. By summarizing the derivations, the particular assumptions and points of departure are made clear. Although the derivations can be found in prior literature, showing and discussing them in a comparative context provides new insight. The present paper is particularly focused on materials that have three or more charge carriers. Thus, the Ambipolar formulation is not directly relevant, but its derivation is included in the appendix.

There are pros and cons associated with the alternative modeling approaches. An advantage of the Integral model is that it is formulated in terms of physical parameters that are independently measurable (e.g., conductivities). The Integral model can be evaluated analytically, and hence the computational cost is significantly lower than solving differential equations. On the other hand, the Integral model demands more assumptions and physical approximations than are required for

---

[*] Corresponding author. Tel: +1-303-273-3379.
Email address: `rjkee@mines.edu` (Robert J. Kee)

the NPP approach. The NPP model is more easily extended. For example, heterogeneous chemical kinetics (i.e., non-equilibrium) can be considered at the membrane surfaces.

The illustrative results in this paper are based upon published thermodynamic and transport properties for $BaZr_{0.8}Y_{0.2}O_{3-\delta}$ (BZY20), which is a doped perovskite material [17–28]. In moist atmospheres and at elevated temperature BZY20 is a mixed proton, oxide ion, and electronic (p-type) conductor. The model includes electrons as a possible charge carrier, but for all conditions studied the electron concentrations are negligible small. Also, for illustrative purposes, results are presented in the context of a particular button-cell configuration. However, it is important to note that the theoretical foundations and conclusions are much broader than the particular illustrative results presented.

Depending on the technology application, MIEC membranes can be used in many different physical configurations, including planar or tubular cells in different gas environments. Although the models are more general, the results and discussion in the present paper are in the context of button cells. Button-cell experiments, such as the one illustrated in Fig. 1, are often configured to measure membrane performance. As illustrated, the membrane is attached to the ceramic tube using spring compression and metal seals. The membrane may be relatively thick (order 1 mm) and self supporting. Alternatively, a thin (order tens of microns) dense membrane may be supported in a porous ceramic or ceramic-metallic (cermet) composite structure. In a typical experiment, the gas phase composition on the top side of the membrane is controlled by a flow of a particular composition (e.g., a hydrogen-rich mixture). The lower chamber is fed with an inert sweep gas (e.g., argon). Measuring the gas-phase composition in the permeate exhaust gas provides a quantitative measure of the effective permeation through the membrane. The examples and model-comparisons in this paper are based on a button-cell configuration.

The paper uses several examples to compare flux predictions from the Integral and NPP approaches. Under many circumstances, the two approaches provide essentially the same results. However, such direct comparisons also show circumstances where the two approaches yield different predictions. The discussion identifies the causes for the departures in the context of assumptions in the theoretical formulations. Thus, the paper provides new insight concerning the ranges of applicability for alternative models. Finally, the influence of gas phase composition at the membrane surfaces on defect concentration profiles and fluxes within the solid is discussed in light of the modeled results.

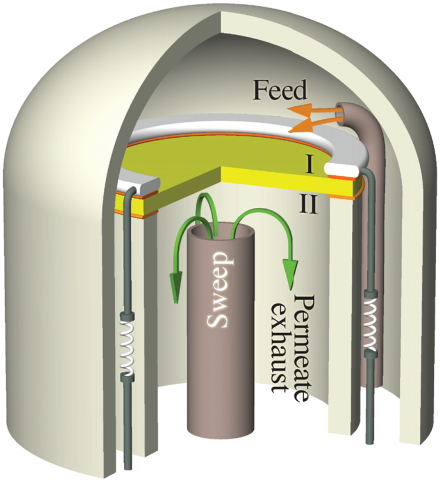

Figure 1: Cartoon representation of a button-cell reactor with a ceramic membrane being exposed to different gas-phase environments on each side of the membrane. Typically, the flow rates on the feed side are very high relative to fluxes through the membrane, establishing a fixed feed-gas composition. The sweep flow rates are typically low and use an inert carrier gas, thus enabling the measurement of apparent permeation fluxes through the membrane.

2. Naming conventions

Prior literature uses alternative conventions for identifying the mobile species. Although alternative naming conventions are equivalent, different representations are more natural or convenient in different contexts. In the present paper, the NPP model is formulated using Kröger–Vink notation for defects, while the Integral model uses the ionic species directly. The ionic species are used when directly comparing flux predictions from the two models. The electronic species, electrons and electron holes, are understood to be small polarons.

Using Kröger–Vink notation, the four defects in the present study are oxygen vacancies $V_O^{\bullet\bullet}$, protons in the form of hydroxide ions $OH_O^{\bullet}$, electrons e', and electron holes $h^{\bullet}$. The associated effective charges of the defects are $z_{V_O^{\bullet\bullet}} = +2$, $z_{OH_O^{\bullet}} = +1$, $z_{e'} = -1$, and $z_{h^{\bullet}} = +1$. The nomenclature $OH_O^{\bullet}$ is meant to indicate that mobile protons are associated with oxygen sites. The flux of protons may be represented as $\mathbf{J}_{H^+}$ or $\mathbf{J}_{OH_O^{\bullet}}$, and $\mathbf{J}_{H^+} = \mathbf{J}_{OH_O^{\bullet}}$. In BZY20, the flux of oxygen vacancies is opposite the flux of oxide ions, $\mathbf{J}_{V_O^{\bullet\bullet}} = -\mathbf{J}_{O^{2-}}$.

3. Defect equilibrium at gas-membrane interfaces

The defect concentrations at the gas-membrane interfaces are established to maintain equilibrium. In the case of materials such as doped barium zirconates (e.g., BZY20), the defect reactions considered are (in Kröger–Vink notation):

$$\frac{1}{2}\mathrm{H_2} + \mathrm{O_O^\times} \rightleftharpoons \mathrm{OH_O^\bullet} + \mathrm{e'}, \tag{1}$$

$$\frac{1}{2}\mathrm{O_2} + \mathrm{V_O^{\bullet\bullet}} \rightleftharpoons \mathrm{O_O^\times} + 2\mathrm{h^\bullet}, \tag{2}$$

$$\mathrm{H_2O} + \mathrm{V_O^{\bullet\bullet}} + \mathrm{O_O^\times} \rightleftharpoons 2\mathrm{OH_O^\bullet}, \tag{3}$$

$$\mathrm{null} \rightleftharpoons \mathrm{h^\bullet} + \mathrm{e'}. \tag{4}$$

In addition to the reactions, evaluating the defect concentrations depends also on maintaining charge neutrality, which requires that

$$2[\mathrm{V_O^{\bullet\bullet}}]_\mathrm{L} + [\mathrm{OH_O^\bullet}]_\mathrm{L} + [\mathrm{h^\bullet}]_\mathrm{L} - [\mathrm{e'}]_\mathrm{L} - [\mathrm{Y'_{Zr}}]_\mathrm{L} = 0. \tag{5}$$

Perovskite doping concentration in the present study is 20%, in which case $\left[\mathrm{Y'_{Zr}}\right]_\mathrm{L} \approx 0.2$. The number of oxygen-ion sites in a perovskite lattice (per formula unit, as indicated by the subscript "L") must be maintained as 3. Thus,

$$[\mathrm{V_O^{\bullet\bullet}}]_\mathrm{L} + [\mathrm{OH_O^\bullet}]_\mathrm{L} + [\mathrm{O_O^\times}]_\mathrm{L} = 3. \tag{6}$$

The equilibrium relationship for the defect reactions (Equations 1-4) may be expressed as

$$K_{p,\mathrm{H_2}} = \frac{\left[\mathrm{OH_O^\bullet}\right]_\mathrm{L}[\mathrm{e'}]_\mathrm{L}}{\left[\mathrm{O_O^\times}\right]_\mathrm{L} p_{\mathrm{H_2}}^{1/2}}, \tag{7}$$

$$K_{p,\mathrm{O_2}} = \frac{\left[\mathrm{O_O^\times}\right]_\mathrm{L}[\mathrm{h^\bullet}]_\mathrm{L}^2}{\left[\mathrm{V_O^{\bullet\bullet}}\right]_\mathrm{L} p_{\mathrm{O_2}}^{1/2}}, \tag{8}$$

$$K_{p,\mathrm{H_2O}} = \frac{\left[\mathrm{OH_O^\bullet}\right]_\mathrm{L}^2}{\left[\mathrm{O_O^\times}\right]_\mathrm{L}\left[\mathrm{V_O^{\bullet\bullet}}\right]_\mathrm{L} p_{\mathrm{H_2O}}}, \tag{9}$$

$$K_{p,\mathrm{eh}} = [\mathrm{h^\bullet}]_\mathrm{L}[\mathrm{e'}]_\mathrm{L}, \tag{10}$$

where the gas phase concentrations are expressed as partial pressures. The four equilibrium constants K_p are not independent, but are related through the gas-phase equilibrium as

$$K_{p,\mathrm{gas}} = \frac{K_{p,\mathrm{O_2}}K_{p,\mathrm{H_2}}^2}{K_{p,\mathrm{H_2O}}K_{p,\mathrm{eh}}^2} = \frac{p_{\mathrm{H_2O}}}{p_{\mathrm{H_2}}p_{\mathrm{O_2}}^{1/2}}. \tag{11}$$

Table 1: Thermodynamics for defect reactions [17]

	ΔH° (kJ mol^{-1})	ΔS° (J mol^{-1} K^{-1})	K_p (750°C)
$\frac{1}{2}\mathrm{H_2} + \mathrm{O_O^\times} \rightleftharpoons \mathrm{OH_O^\bullet} + \mathrm{e'}$	164.35	-17.85	4.74×10^{-10}
$\frac{1}{2}\mathrm{O_2} + \mathrm{V_O^{\bullet\bullet}} \rightleftharpoons \mathrm{O_O^\times} + 2\mathrm{h^\bullet}$	-135.0	-130.0	1.26×10^{00}
$\mathrm{H_2O} + \mathrm{V_O^{\bullet\bullet}} + \mathrm{O_O^\times} \rightleftharpoons 2\mathrm{OH_O^\bullet}$	-93.3	-113.2	7.09×10^{-02}
$\mathrm{null} \rightleftharpoons \mathrm{h^\bullet} + \mathrm{e'}$	266.2	0.0	2.55×10^{-14}
$\mathrm{H_2} + \frac{1}{2}\mathrm{O_2} \rightleftharpoons \mathrm{H_2O}$	-245.45	-52.51	6.13×10^{09}

The variables appearing in the K_p expressions above must be dimensionless. The defect concentrations are evaluated on the lattice scale while the partial pressures are normalized by the standard-state pressure (bar/bar). The standard state for the electronic defects are defined as unity per formula unit. The equilibrium constants may be evaluated as

$$K_p = \exp\left(-\frac{\Delta G^\circ}{RT}\right), \tag{12}$$

where $\Delta G^\circ = \Delta H^\circ - T\Delta S^\circ$ is the standard change in Gibbs free energy for the reaction.

Assuming that the gas-phase partial pressures and the equilibrium constants are known, Eqs. 7-11, constrained by Eqs. 5 and 6, form a system of equations that can be solved iteratively to determine the defect concentrations at the membrane surface $[X_k]_\mathrm{L}$. To be concrete in the examples that follow, Table 1 provides thermodynamic properties for $\mathrm{BaZr_{0.8}Y_{0.2}O_{3-\delta}}$ (BZY20) [17]. Although the model includes electrons (i.e., small polarons), the $[\mathrm{e'}]$ concentrations are negligibly small for all conditions studied.

4. Nernst–Planck fluxes

The flux of a particular defect k may be represented in terms of its mechanical mobility B_k, concentration $[X_k]$, and electrochemical-potential gradient $\nabla\tilde{\mu}_k$ as

$$\mathbf{J}_k = -B_k[X_k]\nabla\tilde{\mu}_k. \tag{13}$$

Here, the concentrations are represented in molar units, which are related to the lattice concentrations by the molar volume as

$$[X_k] = \frac{[X_k]_\mathrm{L}}{V_\mathrm{m}}. \tag{14}$$

For BZY20, $V_\mathrm{m} = 4.55 \times 10^{-5}$ m^3 mol^{-1}.

The Nernst-Einstein relation provides the relationship between diffusion coefficients D_k and mobilities as

$$B_k = \frac{D_k}{RT}, \tag{15}$$

where R is the gas constant and T is temperature. The electrochemical potential gradients $\nabla\tilde{\mu}_k$ are related to chemical potential $\nabla\mu_k$ and electrostatic potential gradients $\nabla\Phi$ as

$$\nabla\tilde{\mu}_k = \nabla\mu_k + z_k F \nabla\Phi, \tag{16}$$

where F is the Faraday constant and z_k is the effective charge associated with the kth defect. Assuming dilute mixtures, the chemical potential gradients are written as

$$\nabla\mu_k = RT\nabla \ln[X_k], \tag{17}$$

The Nernst–Planck equation follows as

$$\mathbf{J}_k = -D_k\left(\nabla[X_k] + \frac{z_k F}{RT}[X_k]\nabla\Phi\right). \tag{18}$$

In this form, it is evident that the defect fluxes depend upon concentration gradient (diffusion) and electrostatic-potential gradients (migration). The Nernst–Planck equation is valid in a dilute limit (i.e., neglecting off-diagonal Onsager contributions). In other words, the flux of the kth defect directly depends only on the concentration profiles of the kth defect (as well as the electrostatic-potential profile).

The partial conductivity σ_k of each species is a function of its concentration and diffusion coefficient as

$$\sigma_k = \frac{F^2}{RT} z_k^2 [X_k] D_k. \tag{19}$$

The overall conductivity follows as

$$\sigma = \frac{F^2}{RT}\sum_{k=1}^{K} z_k^2 [X_k] D_k. \tag{20}$$

The partial conductivities can be expressed in terms of transference numbers t_k as

$$t_k = \frac{\sigma_k}{\sigma}. \tag{21}$$

Measured conductivities are typically reported as functions of temperature and partial pressures of O_2 and H_2O.

Practical technical applications often depend upon maintaining significantly different gas-phase compositions on opposite faces of the membrane. Consequently, the defect concentrations can vary greatly through the thickness of the membrane. In such cases, Eq. 20 shows that the conductivity also varies through the membrane thickness.

By substituting Eq. 19 into Eq. 18, the Nernst–Planck fluxes can be written in terms of conductivities as

$$\mathbf{J}_k = -\sigma_k\left(\frac{RT}{F^2 z_k^2}\frac{\nabla[X_k]}{[X_k]} + \frac{\nabla\Phi}{z_k F}\right). \tag{22}$$

Table 2: Defect diffusion coefficients, $D_k = D_k^\circ \exp(-E_k/RT)$. [17]

	D_k° ($m^2\ s^{-1}$)	E_k (kJ mol^{-1})	D_k (650°C) ($m^2\ s^{-1}$)	D_k (750°C) ($m^2\ s^{-1}$)
$OH_O^\bullet$	1.55×10^{-8}	43.0	5.72×10^{-11}	9.90×10^{-11}
$V_O^{\bullet\bullet}$	1.90×10^{-9}	70.0	2.08×10^{-13}	5.07×10^{-13}
$h^\bullet$	1.05×10^{-6}	97.0	3.41×10^{-12}	1.17×10^{-11}
e'	1.70×10^{-7}	90.0	1.37×10^{-12}	4.32×10^{-12}

Table 2 lists the diffusion-coefficient parameters [17] that are used in the present study. In the models that follow, both diffusion coefficients and conductivities are used. The partial conductivities are easily evaluated from the diffusion coefficient parameters and the defect concentrations using Eq. 19.

5. Nernst–Planck–Poisson (NPP) model

The NPP problem is formulated in terms of mass and charge conservation equations. In steady-state and one spatial dimension these equations are reduced to an ordinary-differential-equation boundary-value problem.

5.1. Defect conservation

The spatial and temporal variations in defect concentrations are governed by conservation equations as

$$\frac{\partial[X_k]}{\partial t} + \nabla\cdot\mathbf{J}_k = 0, \tag{23}$$

where $[X_k]$ are the defect concentrations and t is time. At steady state,

$$\nabla\cdot(D_k\nabla[X_k]) + \nabla\cdot\left(D_k\frac{z_k F}{RT}[X_k]\nabla\Phi\right) = 0, \quad (k = 1, \ldots, K). \tag{24}$$

Because Eqs. 24 involves the electrostatic potential Φ, these equations cannot be solved alone to predict the K defect concentrations. The electrostatic-potential profiles are determined by solving the Gauss equation.

5.2. Gauss equation

The electrostatic potential Φ is related to the local charge density ρ_e by the Gauss law as

$$\nabla\cdot(\varepsilon_r\varepsilon_o\nabla\Phi) = -\rho_e = -F\sum_{k=1}^{K} z_k[X_k]. \tag{25}$$

The relative and vacuum permittivities are represented as ε_r and ε_o, respectively. In addition to the mobile charge carriers (e.g., $V_O^{\bullet\bullet}$, $OH_O^\bullet$, $h^\bullet$, e'), the concentrations of fixed charges (e.g., associated with the doping) must be included in the summation to evaluate the local charge density. In other words, in the BZY20 case $[\mathrm{Y}'_{\mathrm{Zr}}]_{\mathrm{L}}$ is included in the summation (cf., Eq. 5). Once boundary conditions are specified, the Gauss equation coupled with the defect transport equations form a complete solvable system.

Solving the Gauss equation is nearly equivalent to, but more general than, imposing strict electroneutrality (i.e., $\sum_{k=1}^{K} z_k F[X_k] = 0$). Requiring strict electroneutrality is an implicit relationship from which the electrostatic potential profiles can be determined. Because computational cost of solving Eq. 25 is modest and the generality is increased, the Gauss law is retained in the present paper. However, for the circumstances considered here, solving the Gauss law or imposing strict charge neutrality produce virtually identical electrostatic potential profiles. It can be shown by asymptotic analysis (although outside the scope of this paper) that even extremely small values of ρ_{e} cause leading-order variations in Φ within the bulk of the membrane [12]. This is the reason that strict electroneutrality is a very good approximation. Different algorithms and computational implementations are needed for solving the Gauss equation (a differential equation) or imposing strict electroneutrality (an algebraic constraint). Nevertheless, the computational costs are nearly equivalent.

5.3. Boundary conditions

Because both differential equations in Eqs. 24 and 25 involve elliptic spatial operators, solution requires boundary conditions at both interfaces of the membrane with the adjacent gas. Assuming equilibrium defect reactions provides a means to establish defect concentrations at the membrane surfaces. In addition to defect concentrations, boundary conditions associated with the electrostatic potentials are needed. A reference potential is set arbitrarily to $\Phi = 0$ V on the upper surface. At the lower surface, there must be a balance between the electrical current density i (i.e., the net current per membrane surface area) through an external circuit and the current density associated with charged-defect flux within the membrane. This balance can be expressed as

$$i = \sum_k z_k F J_k. \tag{26}$$

Here J_k is understood to be the axial component of the defect-flux vector, evaluated at the boundary. At open-circuit, which is the subject of the present paper, $i = 0$. Although nominally associated with the Gauss equation, it is interesting to note that this is a boundary condition that does not directly involve Φ.

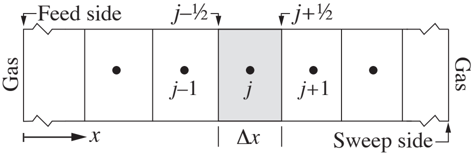

Figure 2: Illustration of a finite-volume mesh network. The shaded area represents a finite volume for cell j. The neighboring cells are represented as $j-1$ and $j+1$.

The coupled combination of Eqs. 24 and 25, together with boundary conditions, form the Nernst–Planck–Poisson model. As discussed subsequently, the problem can be solved computationally. However, it may be noted that under certain limiting circumstances (e.g., ambipolar diffusion and small variations in gas-phase composition) analytical solution can be found [29].

5.4. NPP computational implementation

After spatial discretization the resulting computational problem becomes a system of nonlinear algebraic equations. The spatial discretization in the one-dimensional cartesian coordinates (cf., Fig. 2) can be expressed as

$$\nabla \cdot \mathbf{J} = \frac{d(J)}{dx} \approx \frac{(J_{j+1/2} - J_{j-1/2})}{\Delta x}. \tag{27}$$

The diffusion and migration contributions to the defect fluxes (Eq. 18) can be discretized as, for example,

$$J^{\mathrm{D}}_{j+1/2} \approx -D_k \frac{[X_k]_{j+1} - [X_k]_j}{\Delta x}. \tag{28}$$

As represented in Eq. 27, the fluxes are evaluated at cell faces (i.e., $j + 1/2$ and $j - 1/2$). In the case of the diffusion fluxes (i.e., Eq. 28), the discrete operator is straightforward. However, in the case of the migration flux,

$$\mathbf{J}^{\mathrm{M}}_k = -\left(\frac{z_k F}{RT} D_k \nabla\Phi\right)[X_k], \tag{29}$$

there are alternatives for where to evaluate $[X_k]$. The electrostatic-potential gradient serves as a driving force to transport the charged defect $[X_k]$ in a certain direction. As stated in Eq. 29, the coefficient of $[X_k]$ takes the role of a velocity with an associated magnitude and direction. On physical grounds, the migration flux carries information in the direction of the velocity. For example, in a one-dimensional setting, if $\nabla\Phi > 0$ and $z_k > 0$, then the migration flux is in the negative x direction. In this case, the concentration should be evaluated at x_{j+1}.

In addition to the physical interpretation, there are computational benefits associated with evaluating $[X_k]$ in the sense of an "upwind" convective derivative in fluid mechanics [30].

6. Integral model

Considering Eqs. 17 and 22, the Nernst–Planck equation can be expressed in terms of partial conductivities and the gradients of chemical and electrostatic potentials as

$$\mathbf{J}_k = -\frac{\sigma_k}{z_k^2 F^2}\left(\nabla\mu_k + z_k F \nabla\Phi\right). \tag{30}$$

Under open-circuit conditions (i.e., $F\sum z_k \mathbf{J}_k = 0$), the gradient of electrostatic potential can be replaced, and the species fluxes can be represented using the gradients of chemical potential alone [3];

$$\mathbf{J}_k = -\frac{\sigma_k}{z_k^2 F^2}\left(\nabla\mu_k - z_k \sum_{j=1}^{K} \frac{t_j}{z_j}\nabla\mu_j\right). \tag{31}$$

For a one-dimensional planar membrane at steady state, the axial flux components J_k are spatially uniform within the membrane. The Nernst–Planck flux expression can be integrated across the membrane as

$$\int_{\mathrm{I}}^{\mathrm{II}} J_k \mathrm{d}x = J_k L = -\int_{\mathrm{I}}^{\mathrm{II}} \frac{\sigma_k}{z_k^2 F^2}\left(\mathrm{d}\mu_k - z_k \sum_{j=1}^{K} \frac{t_j}{z_j}\mathrm{d}\mu_j\right), \tag{32}$$

where L is the membrane thickness. Thus, the flux of species k can be represented as

$$J_k = -\frac{1}{z_k^2 F^2 L}\int_{\mathrm{I}}^{\mathrm{II}} \sigma_k \left(\mathrm{d}\mu_k - z_k \sum_{j=1}^{K} \frac{t_j}{z_j}\mathrm{d}\mu_j\right). \tag{33}$$

As a practical matter, the chemical potentials of the charged species cannot be determined directly. To assist the evaluation, the equilibrium relationship between each charged species and its associated neutral species and electrons can be introduced. Consider, for example, the following electrochemical redox reaction for a generic species "A" with charge z.

$$\mathrm{A} \rightleftharpoons \mathrm{A}^z + z\mathrm{e}^- \tag{34}$$

The chemical potentials follow as

$$\mathrm{d}\mu_{\mathrm{A}^z} = \mathrm{d}\mu_{\mathrm{A}} - z\mathrm{d}\mu_{\mathrm{e}^-}. \tag{35}$$

The summation in Eq. 33 can now be represented in terms of the associated neutral species as

$$\sum_{j=1}^{K} \frac{t_j}{z_j}\mathrm{d}\mu_j = -\mathrm{d}\mu_{\mathrm{e}^-} + \sum_{i=1}^{N} \frac{t_i}{z_i}\mathrm{d}\mu_{n,i}, \tag{36}$$

where the summation in the right-hand side includes all ionic species N, and $\mu_{n,i}$ is the chemical potential of the neutral species n with the same chemical composition as i. In this expression, electrons are excluded from the summation.

Equations 35 and 36 can be substituted into Eq. 33, yielding

$$J_k = -\frac{1}{z_k^2 F^2 L}\int_{\mathrm{I}}^{\mathrm{II}} \sigma_k \left(\mathrm{d}\mu_{n,k} - z_k \sum_{i=1}^{N} \frac{t_i}{z_i}\mathrm{d}\mu_{n,i}\right), \tag{37}$$

As an example, consider the application of Eq. 37 to the flux of protons,

$$J_{\mathrm{H}^+} = -\frac{1}{F^2 L}\int_{\mathrm{I}}^{\mathrm{II}} \sigma_{\mathrm{H}^+}\left[\mathrm{d}\mu_{\mathrm{H}} - \left(t_{\mathrm{H}^+}\mathrm{d}\mu_{\mathrm{H}} - \frac{t_{\mathrm{O}^{2-}}}{2}\mathrm{d}\mu_{\mathrm{O}}\right)\right], \tag{38}$$

The charge for the proton is $z_{\mathrm{H}^+} = +1$ and the associated neutral species is atomic hydrogen, H. Assuming four mobile charge carriers (protons, oxide ions, electrons, and holes), the transference numbers must sum to unity as

$$t_{\mathrm{H}^+} + t_{\mathrm{O}^{2-}} + t_{\mathrm{h}^+} + t_{\mathrm{e}^-} = 1. \tag{39}$$

Assume further, that atomic and molecular hydrogen are in equilibrium,

$$2\mathrm{H} \rightleftharpoons \mathrm{H}_2. \tag{40}$$

The atomic-hydrogen chemical potential can be written as

$$\mu_{\mathrm{H}} = \frac{\mu^{\circ}_{\mathrm{H}_2}}{2} + \frac{1}{2}RT\ln p_{\mathrm{H}_2}, \qquad \mathrm{d}\mu_{\mathrm{H}} = \frac{1}{2}RT\mathrm{d}\left(\ln p_{\mathrm{H}_2}\right). \tag{41}$$

Thus, with some algebraic manipulation, Eq. 38 can be rewritten as

$$\begin{aligned} J_{\mathrm{H}^+} = -\frac{RT}{4F^2 L}\int_{\mathrm{I}}^{\mathrm{II}} & \sigma_{\mathrm{H}^+}[2\left(t_{\mathrm{O}^{2-}} + t_{\mathrm{e}^-} + t_{\mathrm{h}^+}\right)\ \mathrm{d}\left(\ln p_{\mathrm{H}_2}\right) \\ & + t_{\mathrm{O}^{2-}}\ \mathrm{d}\left(\ln p_{\mathrm{O}_2}\right)]. \end{aligned} \tag{42}$$

This expression can be further modified by assuming gas-phase equilibrium among H_2, O_2, and H_2O, to yield

$$\begin{aligned} J_{\mathrm{H}^+} = -\frac{RT}{2F^2 L}\int_{\mathrm{I}}^{\mathrm{II}} & \sigma_{\mathrm{H}^+}[\left(t_{\mathrm{e}^-} + t_{\mathrm{h}^+}\right)\ \mathrm{d}\left(\ln p_{\mathrm{H}_2}\right) \\ & + t_{\mathrm{O}^{2-}}\ \mathrm{d}\left(\ln p_{\mathrm{H}_2\mathrm{O}}\right)]. \end{aligned} \tag{43}$$

To simplify the notation somewhat, it is convenient to define the sum of the electron and hole transference numbers as

$$t_{\mathrm{el}} \equiv t_{\mathrm{e}^-} + t_{\mathrm{h}^+}. \tag{44}$$

Thus, the proton flux can be represented as

$$J_{\mathrm{H^+}} = -\frac{RT}{2F^2L}\int_{\mathrm{I}}^{\mathrm{II}} \sigma_{\mathrm{H^+}}\left[t_{\mathrm{el}}\,\mathrm{d}\left(\ln p_{\mathrm{H_2}}\right) + t_{\mathrm{O^{2-}}}\,\mathrm{d}\left(\ln p_{\mathrm{H_2O}}\right)\right]. \tag{45}$$

Equation 45, represents a contour integral involving two independent thermodynamic variables ($p_{\mathrm{H_2}}$ and $p_{\mathrm{H_2O}}$). Thus, the integral may be path-dependent as pointed out by Yoo and Martin [31], and cannot be evaluated without introducing some physical assumptions. By considering the proton flux a state function (i.e., path-independent) the single integral in Eq. 45 may separated onto two integrals as

$$\begin{aligned} J_{\mathrm{H^+}} = &-\frac{RT}{2F^2L}\int_{\mathrm{I}}^{\mathrm{II}} \sigma_{\mathrm{H^+}}t_{\mathrm{el}}\,\mathrm{d}\left(\ln p_{\mathrm{H_2}}\right) \\ &-\frac{RT}{2F^2L}\int_{\mathrm{I}}^{\mathrm{II}} \sigma_{\mathrm{H^+}}t_{\mathrm{O^{2-}}}\,\mathrm{d}\left(\ln p_{\mathrm{H_2O}}\right). \end{aligned} \tag{46}$$

In this form, Eq. 46 shows that to a first approximation the proton flux depends upon the ambipolar diffusion of protons and a charge-compensating mobile defect (in this case oxide ions) and an electronic defect (electrons and/or holes). Moreover, the expression shows that the proton transport depends upon the hydrogen and steam partial pressures at the membrane interfaces.

Integrals that are analogous to Eq. 46 can be developed for the oxide ion flux, again assuming that the oxide ion flux is a state function:

$$\begin{aligned} J_{\mathrm{O^{2-}}} = &-\frac{RT}{8F^2L}\int_{\mathrm{I}}^{\mathrm{II}} \sigma_{\mathrm{O^{2-}}}t_{\mathrm{el}}\,\mathrm{d}\left(\ln p_{\mathrm{O_2}}\right) \\ &-\frac{RT}{4F^2L}\int_{\mathrm{I}}^{\mathrm{II}} \sigma_{\mathrm{O^{2-}}}t_{\mathrm{H^+}}\,\mathrm{d}\left(\ln p_{\mathrm{H_2O}}\right). \end{aligned} \tag{47}$$

The approximate expressions for proton and oxide ion fluxes can be rewritten in terms of partial conductivities as

$$\begin{aligned} J_{\mathrm{H^+}} = &-\frac{RT}{2F^2L}\int_{\mathrm{I}}^{\mathrm{II}} \frac{\sigma_{\mathrm{H^+}}\sigma_{\mathrm{el}}}{\sigma_{\mathrm{tot}}}\mathrm{d}\left(\ln p_{\mathrm{H_2}}\right) \\ &-\frac{RT}{2F^2L}\int_{\mathrm{I}}^{\mathrm{II}} \frac{\sigma_{\mathrm{H^+}}\sigma_{\mathrm{O^{2-}}}}{\sigma_{\mathrm{tot}}}\mathrm{d}\left(\ln p_{\mathrm{H_2O}}\right), \end{aligned} \tag{48}$$

$$\begin{aligned} J_{\mathrm{O^{2-}}} = &-\frac{RT}{8F^2L}\int_{\mathrm{I}}^{\mathrm{II}} \frac{\sigma_{\mathrm{O^{2-}}}\sigma_{\mathrm{el}}}{\sigma_{\mathrm{tot}}}\mathrm{d}\left(\ln p_{\mathrm{O_2}}\right) \\ &-\frac{RT}{4F^2L}\int_{\mathrm{I}}^{\mathrm{II}} \frac{\sigma_{\mathrm{O^{2-}}}\sigma_{\mathrm{H^+}}}{\sigma_{\mathrm{tot}}}\mathrm{d}\left(\ln p_{\mathrm{H_2O}}\right). \end{aligned} \tag{49}$$

To evaluate the integrals in Eqs. 48 and 49, partial pressures on both sides of the membrane and transport parameters for all mobile species must be known. Depending on the membrane material and the gas-phase compositions, the partial conductivities can vary significantly through the membrane thickness. Thus, evaluating the integrals depends upon being able to express the functional dependencies of the partial conductivities. For the BZY20 considered here, the electronic conductivity is dominated by electron holes, which increases as a function of $p_{\mathrm{O_2}}$. Thus, in a configuration such as Fig. 1 with a reducing environment on the feed (top) side, the hole conductivity increases through the membrane from the relatively low $p_{\mathrm{O_2}}$ feed side toward the relatively high $p_{\mathrm{O_2}}$ permeate side.

A simplified electroneutrality model is assumed to establish functional dependencies for the partial conductivities. The acceptors are charge-compensated by oxygen vacancies, and under wet conditions by protons as well. Thus, the oxide ion and proton conductivities are assumed to be independent of $p_{\mathrm{O_2}}$. Considering the equilibrium relationship (Eq. 8), the hole conductivity may be assumed to be a function of $p_{\mathrm{O_2}}$ or $p_{\mathrm{H_2}}$ (at constant $p_{\mathrm{H_2O}}$) as

$$\sigma_{\mathrm{h^+}} = \sigma^{\circ}_{\mathrm{h^+,O_2}}p_{\mathrm{O_2}}^{1/4} = \sigma^{\circ}_{\mathrm{h^+,H_2}}p_{\mathrm{H_2}}^{-1/2}, \tag{50}$$

where $\sigma^{\circ}_{\mathrm{h^+,O_2}}$ is the hole conductivity at one atmosphere of O_2, and $\sigma^{\circ}_{\mathrm{h^+,H_2}}$ is the hole conductivity at one atmosphere of H_2. Assuming that oxygen vacancies are the dominant charge-compensating defect under both wet and dry conditions with an essentially constant concentration, an analogous expression (using Eq. 9) can be obtained for the proton conductivity of BZY20 as a function of water-vapor partial pressure,

$$\sigma_{\mathrm{H^+}} = \sigma^{\circ}_{\mathrm{H^+}}p_{\mathrm{H_2O}}^{1/2}, \tag{51}$$

where $\sigma^{\circ}_{\mathrm{H^+}}$ is the proton conductivity at one atmosphere of H_2O.

Using the assumed functional forms for the conductivities and using, for example,

$$\mathrm{d}\left(\ln p_{\mathrm{H_2}}\right) = \frac{\mathrm{d}p_{\mathrm{H_2}}}{p_{\mathrm{H_2}}}, \tag{52}$$

the flux integrals (Eqs. 46 and 49) can be rewritten as

$$\begin{aligned} J_{\mathrm{H^+}} = &-\frac{RT}{2F^2L}\int_{\mathrm{I}}^{\mathrm{II}} \frac{\sigma_{\mathrm{H^+}}\sigma^{\circ}_{\mathrm{h^+,H_2}}p_{\mathrm{H_2}}^{-1/2}}{\sigma_{\mathrm{H^+}} + \sigma_{\mathrm{O^{2-}}} + \sigma^{\circ}_{\mathrm{h^+,H_2}}p_{\mathrm{H_2}}^{-1/2}}\frac{\mathrm{d}p_{\mathrm{H_2}}}{p_{\mathrm{H_2}}} \\ &-\frac{RT}{2F^2L}\int_{\mathrm{I}}^{\mathrm{II}} \frac{\sigma_{\mathrm{O^{2-}}}\sigma^{\circ}_{\mathrm{H^+}}p_{\mathrm{H_2O}}^{1/2}}{\sigma^{\circ}_{\mathrm{H^+}}p_{\mathrm{H_2O}}^{1/2} + \sigma_{\mathrm{O^{2-}}} + \sigma_{\mathrm{el}}}\frac{\mathrm{d}p_{\mathrm{H_2O}}}{p_{\mathrm{H_2O}}}. \end{aligned} \tag{53}$$

$$J_{\mathrm{O}^{2-}} = -\frac{RT}{8F^2L}\int_{\mathrm{I}}^{\mathrm{II}} \frac{\sigma_{\mathrm{O}^{2-}}\sigma^{\circ}_{\mathrm{h}^+,\mathrm{O}_2} p_{\mathrm{O}_2}^{1/4}}{\sigma_{\mathrm{H}^+} + \sigma_{\mathrm{O}^{2-}} + \sigma^{\circ}_{\mathrm{h}^+,\mathrm{O}_2} p_{\mathrm{O}_2}^{1/4}} \frac{\mathrm{d}p_{\mathrm{O}_2}}{p_{\mathrm{O}_2}}$$

$$- \frac{RT}{4F^2L}\int_{\mathrm{I}}^{\mathrm{II}} \frac{\sigma_{\mathrm{O}^{2-}}\sigma^{\circ}_{\mathrm{H}^+} p_{\mathrm{H}_2\mathrm{O}}^{1/2}}{\sigma^{\circ}_{\mathrm{H}^+} p_{\mathrm{H}_2\mathrm{O}}^{1/2} + \sigma_{\mathrm{O}^{2-}} + \sigma_{\mathrm{el}}} \frac{\mathrm{d}p_{\mathrm{H}_2\mathrm{O}}}{p_{\mathrm{H}_2\mathrm{O}}}. \tag{54}$$

The integrals in Eqs. 53 and 54 can be evaluated analytically, with the fluxes expressed as functions of the partial conductivities and gas phase partial pressures on both sides of the membrane. As an example, the following expression shows the integrated form of the first integral in Eq. 53

$$2\sigma_{\mathrm{H}^+}\ln\left(p_{\mathrm{H}_2}^{1/2}\right) - 2\sigma_{\mathrm{H}^+}\ln\left(\frac{2(\sigma_{\mathrm{H}^+} + \sigma_{\mathrm{O}^{2-}})p_{\mathrm{H}_2}^{1/2}}{\sigma^{\circ}_{\mathrm{h}^+,\mathrm{H}_2}} + 2\right)\Bigg|_{\mathrm{I}}^{\mathrm{II}}.$$

The partial conductivities are determined from the surface defect concentrations (Eqs. 7-11) combined with Eq. 19. The gas-phase composition in the upper chamber (feed) is specified. The gas-phase composition in the lower chamber (permeate) is established from the steady-state perfectly stirred reactor model (Sect. 8).

7. Equilibrium gas-phase fluxes

The NPP and Integral models both predict species fluxes within the membrane. The ionic species manifest themselves as gas-phase fluxes at the interface. Assuming equilibrium chemistry at the interfaces, the gas-phase fluxes can be evaluated as follows.

Assuming the only gas-phase species are H_2, O_2, and H_2O, and based on the oxygen and hydrogen element balances, the gas-phase species must satisfy the following constraints:

$$2\mathbf{J}_{\mathrm{O}_2} + \mathbf{J}_{\mathrm{H}_2\mathrm{O}} = \mathbf{J}_{\mathrm{O}^{2-}}, \tag{55}$$

$$2\mathbf{J}_{\mathrm{H}_2} + 2\mathbf{J}_{\mathrm{H}_2\mathrm{O}} = \mathbf{J}_{\mathrm{H}^+}. \tag{56}$$

Assume further that oxygen, hydrogen and water vapor are in equilibrium at the membrane surface. Thus, the relative concentration variations of the gas-phase species are required to satisfy

$$\frac{1}{[\mathrm{H_2O}]}\frac{d[\mathrm{H_2O}]}{dt} - \frac{1}{[\mathrm{H_2}]}\frac{d[\mathrm{H_2}]}{dt} - \frac{1}{2[\mathrm{O_2}]}\frac{d[\mathrm{O_2}]}{dt} = 0, \tag{57}$$

which is obtained by differentiating Eq. 11 (at fixed temperature). Assume that the gas-phase species near the membrane surfaces (interface area A_{s}) are equilibrated within a small, but arbitrary, volume V_{s}. Assume further that variations in gas-phase concentrations are due only to the species fluxes at the membrane surface $\mathbf{J}_k$. The gas-phase concentrations within the volume can be represented as

$$\frac{d[X_k]}{dt} = \frac{A_{\mathrm{s}}}{V_{\mathrm{s}}}\mathbf{J}_k. \tag{58}$$

Substituting Eq. 58 into Eq. 57 yields

$$\frac{\mathbf{J}_{\mathrm{H_2O}}}{[\mathrm{H_2O}]} - \frac{\mathbf{J}_{\mathrm{H_2}}}{[\mathrm{H_2}]} - \frac{1}{2}\frac{\mathbf{J}_{\mathrm{O_2}}}{[\mathrm{O_2}]} = 0. \tag{59}$$

Combining Eqs. 55, 56,and 59, exchanging concentrations for partial pressures, and doing some algebraic simplification, the gas-phase H_2O flux can be written as

$$\mathbf{J}_{\mathrm{H_2O}} = \frac{\mathbf{J}_{\mathrm{H}^+}}{\left[2 + \dfrac{2p_{\mathrm{H}_2}}{p_{\mathrm{H_2O}}} + \dfrac{p_{\mathrm{H}_2}}{2p_{\mathrm{O}_2}}\right]} + \frac{\mathbf{J}_{\mathrm{O}^{2-}}}{\left[1 + \dfrac{4p_{\mathrm{O}_2}}{p_{\mathrm{H_2O}}} + \dfrac{4p_{\mathrm{O}_2}}{p_{\mathrm{H}_2}}\right]}. \tag{60}$$

The O_2 and H_2 fluxes follow easily as

$$\mathbf{J}_{\mathrm{O}_2} = \frac{1}{2}\mathbf{J}_{\mathrm{O}^{2-}} - \frac{1}{2}\mathbf{J}_{\mathrm{H_2O}}, \tag{61}$$

$$\mathbf{J}_{\mathrm{H}_2} = \frac{1}{2}\mathbf{J}_{\mathrm{H}^+} - \mathbf{J}_{\mathrm{H_2O}}. \tag{62}$$

It is interesting to note the limiting behaviors of the gas-phase-flux expressions. Under a strongly reducing environment (i.e., $[\mathrm{H_2}] \gg [\mathrm{O_2}]$, and $[\mathrm{H_2O}] \gg [\mathrm{O_2}]$), the gas-phase species fluxes are approximately

$$\mathbf{J}_{\mathrm{H_2O}} = \mathbf{J}_{\mathrm{O}^{2-}}, \tag{63}$$

$$\mathbf{J}_{\mathrm{O}_2} = 0, \tag{64}$$

$$\mathbf{J}_{\mathrm{H}_2} = \frac{1}{2}\mathbf{J}_{\mathrm{H}^+} - \mathbf{J}_{\mathrm{O}^{2-}}. \tag{65}$$

Under a strongly oxidizing environment (i.e., $[\mathrm{O_2}] \gg [\mathrm{H_2}]$, and $[\mathrm{H_2O}] \gg [\mathrm{H_2}]$), the gas-phase species fluxes are approximately

$$\mathbf{J}_{\mathrm{H_2O}} = \frac{1}{2}\mathbf{J}_{\mathrm{H}^+}, \tag{66}$$

$$\mathbf{J}_{\mathrm{O}_2} = -\frac{1}{4}\mathbf{J}_{\mathrm{H}^+} + \frac{1}{2}\mathbf{J}_{\mathrm{O}^{2-}}, \tag{67}$$

$$\mathbf{J}_{\mathrm{H}_2} = 0. \tag{68}$$

8. Gas-phase balance

The lower chamber (Fig. 1) can be modeled as a perfectly stirred reactor (PSR). As illustrated in Fig. 3, sweep gases with a fixed composition (mole fraction $X_{\mathrm{s},k}$ or mass fraction $Y_{\mathrm{s},k}$) and fixed mass flow rate $\dot{m}_{\mathrm{s}}$

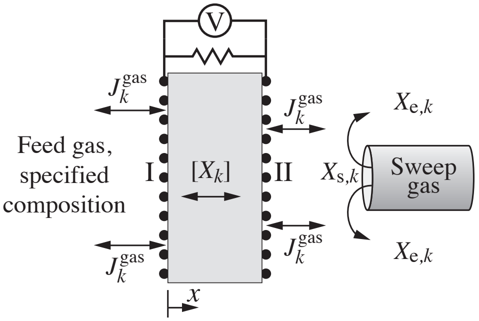

Figure 3: Schematic representation of a button-cell ceramic membrane being exposed to different gas-phase environments.

enter the chamber through the inner tube. Additionally, there is gas exchange at the membrane interface. Once within the open space below the membrane, gases are presumed to mix immediately and completely. The composition of the mixture leaving the chamber via the annular space between the inlet tube and the membrane-support tube is assumed to be the same as the mixture within the stirred reactor.

The overall mass balance requires that

$$\dot{m}_{\mathrm{s}} + A_{\mathrm{s}} \sum_{k=1}^{K} J_k^{\mathrm{gas}} W_k = \dot{M}, \tag{69}$$

where J_k^{gas} are molar fluxes of the gas-phase species at the membrane interface (i.e., Eqs. 60-62), A_{s} is the membrane surface area, and W_k are the gas-phase species molecular weights. The net mass flow rate leaving the chamber is $\dot{M}$. The species mass-continuity equations can be expressed as

$$\dot{m}_{\mathrm{s}} Y_{\mathrm{s},k} + A_{\mathrm{s}} J_k^{\mathrm{gas}} W_k = \dot{M} Y_{\mathrm{e},k}, \tag{70}$$

where $Y_{\mathrm{e},k}$ are the exiting mass fractions, which is the composition that would be measured in an experiment.

9. Results and discussion

Table 3: Nominal model parameters

Parameter	Value
General	
Temperature, T	750 °C
Pressure, p	1 atm
Diameter, d	10 mm
Surface area, A_{s}	7.85×10^{-5} m^2
Feed volume bulk gas composition	
Feed $p_{\mathrm{H_2}}$	0.98 atm
Feed $p_{\mathrm{H_2O}}$	0.02 atm
Feed $p_{\mathrm{O_2}}$	10^{-12} atm
Feed p_{Ar}	0 atm
Membrane (BZY20)	
Thickness, L	25 μm
Sweep inlet flow	
Sweep flow rate, Q	0.1 slpm
Sweep flow rate, $\dot{m}''$	3.77×10^{-2} kg s^{-1} m^{-2}
Sweep p_{Ar}	0.98 atm
Sweep $p_{\mathrm{H_2O}}$	0.02 atm
Sweep $p_{\mathrm{O_2}}$	10^{-5} atm
Sweep $p_{\mathrm{H_2}}$	10^{-15} atm

Table 3 lists nominal parameters that are used to illustrate the models. The temperature is uniform at 750 °C and the total pressure is atmospheric. The membrane is 10 mm in diameter, yielding a surface area of $A_{\mathrm{s}} = 7.85 \times 10^{-5}$ m^2. The feed-side flow rate (top of Fig. 1) is assumed to be very high, establishing a fixed gas-phase composition within the volume above the membrane (Table 3). However, at the membrane surface the gas-phase composition is evaluated at equilibrium. The sweep side is fed with a relatively low flow rate having a fixed inlet composition. When the sweep flow rate is comparable to the apparent gas-phase fluxes through the membrane, the measurable gas composition emerging from the permeate side will depend upon the fluxes through the membrane. In most cases, the sweep flow rate Q is stated in standard liters per minute (slpm), which would relate to the experimental laboratory conditions. However, a more general measure is mass flow rate normalized by the membrane area as $\dot{m}'' = Q\rho/A$ (kg s^{-1} m^{-2}).

9.1. *Fluxes as function of membrane thickness*

Figure 4 compares modeled fluxes from the NPP and Integral models as functions of membrane thickness for the gas-phase compositions listed in Table 3. The two approaches predict nearly identical fluxes for all membrane thicknesses. The total flux is dominated by protons and electron holes, with only minor contributions from oxide ions, due to the relatively low conductivity of both oxide ions and electron holes under essentially wet reducing conditions. Thus, under these conditions, the system can be considered within the limit of ambipolar transport. Furthermore, because there is negligible water vapor variation across the membrane, the potential mathematical error associated with splitting the integral in Eq. 45 is not significant.

Based upon the NPP model, Fig. 5 shows defect concentration and electrostatic-potential profiles within the membrane for the nominal conditions (Table 3). The

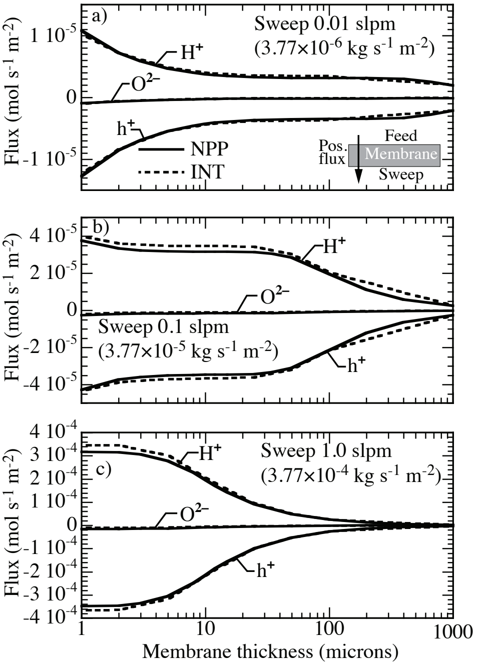

Figure 4: Predicted species fluxes (protons H^+, oxide ions O^{2-}, and holes h^+) as functions of membrane thickness for three different sweep flow rates. A positive flux means transport from the feed side toward the sweep side. The temperature is isothermal at 750 °C and Table 3 lists the feed and sweep compositions. The solid lines represent the NPP model and the dashed lines represent the Integral model.

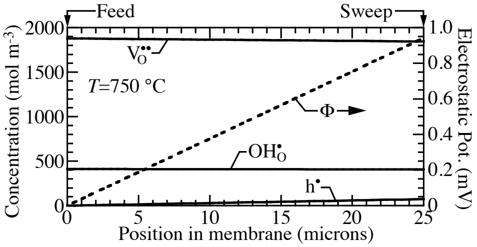

Figure 5: Defect-concentration and electrostatic-potential profiles predicted by the NPP model within the membrane. In this case, the membrane thickness is 25 μm, the sweep rate is 0.1 slpm (3.77×10^{-5} kg s^{-1} m^{-2}), and the temperature is 750 °C.

oxygen vacancy and proton concentrations are nearly uniform, while the electron hole concentration increases from the highly reducing feed side toward the essentially inert sweep side. Nevertheless, electron hole concentration remains a minority defect throughout the membrane. Thus, the simplified electroneutrality condition assumed for the Integral model ($2[\mathrm{V}_\mathrm{O}^{\bullet\bullet}] = [\mathrm{Y}'_{Zr}]$) is consistent with the predicted defect concentrations from the NPP model. The profiles from the NPP model provide further support for the predictions from the two models being essentially the same under conditions such as those in Table 3.

As is easily anticipated, Fig. 4 shows that the fluxes decrease as the membrane thickness increase. Additionally, the defect fluxes increase as the sweep flow rate increases. However, Fig. 4 reveals certain “plateau” regions where the defect fluxes are nearly constant as functions of membrane thickness. Such behavior is more unexpected. Defect fluxes are generally expected to vary linearly with membrane thickness when the surface reactions are assumed to be equilibrated. Discussion in the following section shows that these effects are due to the coupled interactions between gas-phase composition in the sweep-side chamber and defect fluxes through the membrane.

9.2. *Gas phase fluxes*

As represented by Eqs. 69 and 70, the sweep-volume composition is the result of interactions between gas fluxes at the membrane surface and the introduction of gases via the sweep flow. Gas fluxes at the membrane surface are related to the defect fluxes, which in turn are affected directly by the gas-phase composition at the surface (Eqs. 60-62). Figure 6 shows gas-phase fluxes predicted by the NPP model, corresponding to the simulations shown in Fig. 4. Consider, for example, Fig. 6b showing the 0.1 slpm case. With thin membranes (i.e., $L < 10\,\mu$m), the gas fluxes into and out of the membrane are very nearly balanced (e.g., gas-phase flux H_2 leaving the feed volume is essentially the same as the H_2 flux entering the sweep volume). This behavior is the result of relatively high fluxes through the membrane compared to the sweep flow rates. For membrane thickness greater than approximately $10\,\mu$m there is a significant departure between the gas fluxes that are apparently entering the membrane from the feed side and the fluxes of the gases apparently leaving the membrane and entering the sweep volume (Fig. 6b); the proton flux on the sweep side is increasingly reacted to form H_2O (reverse of Reaction 3). Correspondingly, as a result of gas-phase equilibrium at the sweep-side membrane surface ($H_2 + \frac{1}{2}O_2 \rightleftharpoons H_2O$), there is an apparent flux of O_2 into the membrane and H_2O away from the membrane. Fig-

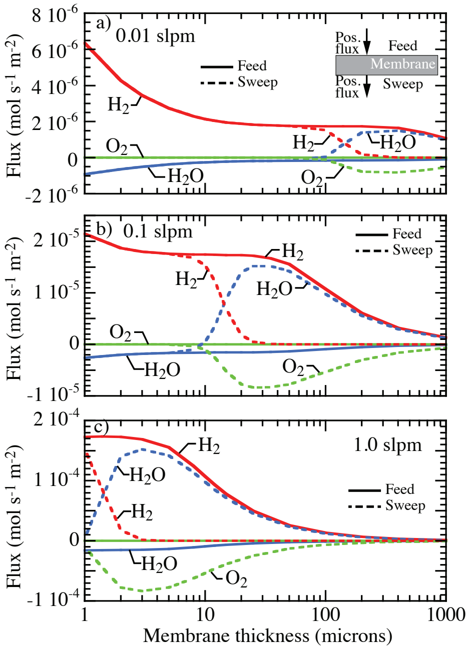

Figure 6: Predicted gas fluxes versus membrane thickness for three different sweep flow rates. The solid lines represent the fluxes on the feed side and the dashed lines represent the fluxes on the sweep side. Positive fluxes on the feed side indicate gases leaving the feed volume and apparently entering the membrane and positive fluxes on the sweep side represent gases leaving the membrane and entering the sweep volume. The temperature is isothermal at 750 °C and Table 3 lists the feed and sweep compositions.

ures 6abc all show the similar qualitative behaviors, but with the regions of gas-phase flux departures depending upon sweep flow rates. These results, which emphasize the coupled behaviors between the sweep flow rates and the membrane fluxes, provide potentially insight in interpreting experimental observations from experiments such as illustrated in Fig. 1.

Figure 7, showing gas-phase mole fractions in the sweep volume, provides further insight to interpret the results shown on Figs. 4 and 6. The model considers two limiting gas-phase compositions in the sweep volume; one is the bulk gas composition (mass fractions $Y_{\mathrm{e,k}}$ or mole fractions $X_{\mathrm{e,k}}$) and the other is the equilibrium mixture at the membrane surface (mass fractions $Y^{\mathrm{eq}}_{\mathrm{e,k}}$ or mole fractions $X^{\mathrm{eq}}_{\mathrm{e,k}}$). Figure 7 shows the bulk mole fractions as solid lines and the equilibrium as dashed lines. For the cases considered here the bulk

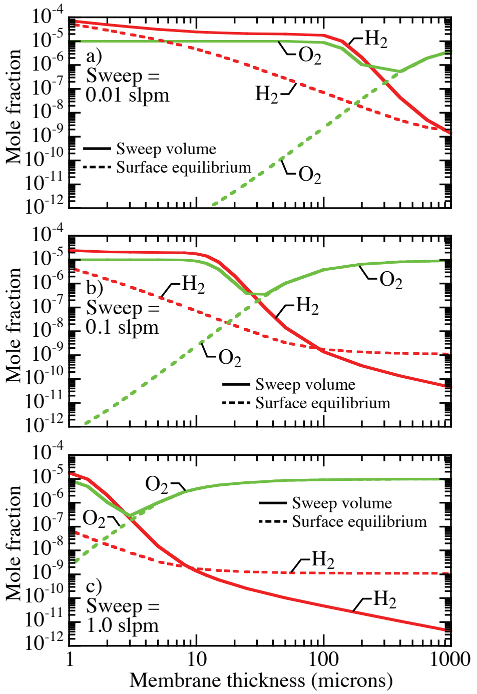

Figure 7: Predicted gas-phase mole fractions versus membrane thickness for three different sweep flow rates. The solid lines represent the bulk composition within the sweep volume and the dashed lines represent equilibrium compositions. The model assumes that gas-phase equilibrium is achieved at the membrane surface, and the equilibrium gas-phase composition is used in evaluating the equilibrium defect composition at the membrane surface. The bulk H_2O mole fraction remains very close to 2% for all conditions, and are not included in this figure. The temperature is isothermal at 750 °C and Table 3 lists the feed and inlet sweep compositions.

H_2O mole fraction remains very close to 2%, and only the relatively small H_2 and O_2 mole fractions are plotted. The bulk composition (e.g., $X_{\mathrm{e,k}}$) is the measurable composition in an experiment such as the one illustrated in Fig. 1.

Consider the H_2 and O_2 mole fractions in Fig. 7b. For membrane thickness above about 50 μm the equilibrium mole fractions of O_2 and H_2 are essentially constant and identical to the inlet sweep gas composition (Table 3). As the thickness decreases, the equilibrium mole fraction of O_2 decreases nearly linearly, with a corresponding increase in the H_2 mole fraction. The oxygen depletion leads to decreased electron hole concentration as a function of decreasing membrane thickness. Accord-

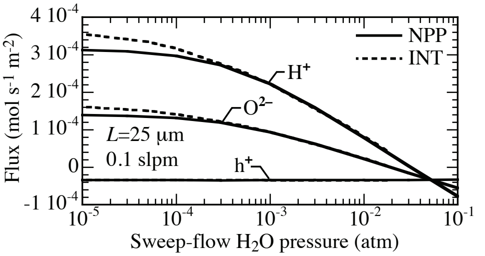

Figure 8: Defect fluxes as a function of H_2O concentration in the sweep flow. The membrane thickness is 25 μm, the temperature is 750 °C, and the sweep flow rate is 0.1 slpm. Positive fluxes are in the direction from the feed side toward the sweep side.

ingly, the flux of protons – limited by electron hole conductivity in these cases – becomes effectively thickness independent, as observed in Fig. 4. This result illustrates how gas-phase chemistry at the membrane surface (e.g., departures from equilibrium) can strongly influence defect fluxes through the membrane interior. Even when the surface reactions are assumed to be at equilibrium, fluxes depend upon coupled nonlinear interactions with the transport processes. Figures 7abc all show the same qualitative trends, but with the effects of thickness depending upon the sweep flow rates.

The model is written generally to allow gas-phase to be equilibrated or not-equilibrated on the membrane surface and in the bulk gas sweep volume. The results in the present paper are based upon the surface being equilibrated, but the bulk sweep-volume gas phase not being in chemical equilibrium. Thus, as shown in Fig. 7, for example, H_2 and O_2 can co-exist in the bulk sweep gas. If an ignition source were present, or the composition was within auto-ignition flammability limits, it is possible that the bulk gas could be also equilibrated, which would reduce the H_2 and O_2 concentrations and increase the H_2O concentration.

9.3. Sweep flow steam concentration

In the foregoing example, the inlet gas compositions were fixed at the nominal model conditions; essentially wet and reducing atmospheres on both sides of the membrane. Figure 8 presents the predicted defect fluxes using the NPP and Integral models as a functions of sweep-side inlet water-vapor partial pressure. The varying H_2O concentration is offset by Ar concentration, with the O_2 and H_2 concentrations remaining fixed as in Table 3. The feed composition is also fixed as in Table 3. The results show that the models agree well for $p_{H_2O} > 10^{-4}$ atm. The sweep side gas is essentially reducing in all cases and electron holes are still predicted to act as minority defects concentration-wise according to the NPP model, in accordance with the electroneutrality assumed for the Integral model. At lower p_{H_2O} (i.e., with larger water vapor variations), the Integral model predicts slightly higher defect fluxes than the NPP model. For these conditions, the mathematical error related to splitting the integral in Eq 45 increases, decreasing the accuracy of the Integral model.

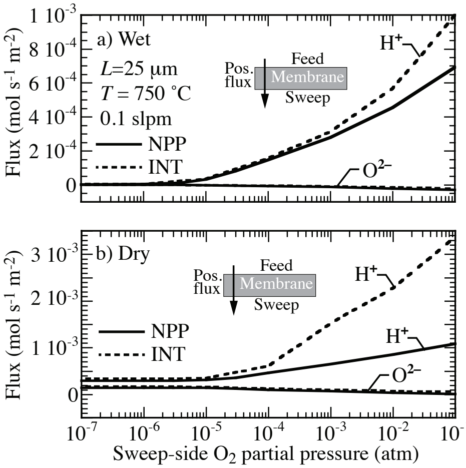

Figure 9: Defect fluxes versus O_2 concentration in the sweep flow. The membrane thickness is 25 μm, the temperature is 750 °C, and the sweep flow rate is 0.1 slpm. The “wet” cases assume 2% H_2O in the sweep-flow inlet gas and the “dry” cases assume 10^{-5} atm H_2O in the sweep composition. The feed side composition is fixed as in Table 3.

9.4. Sweep flow oxygen concentration

Figure 9 compares predicted fluxes using NPP and Integral models as functions of oxygen partial pressure in the sweep flow. In the “wet” cases, the H_2O partial pressure is fixed as $p_{H_2O} = 0.02$ atm and in the “dry” cases $p_{H_2O} = 10^{-5}$ atm. The varying oxygen partial pressure is offset by varying the Ar partial pressure. The sweep flow rate is fixed at 0.1 slpm. Clearly, as the sweep side becomes increasingly oxidizing, the departure between the NPP and Integral models increases. The Integral approach tends to predict larger fluxes than the NPP approach does. Especially in the dry cases, the departure is significant. To elucidate the origin of of the observed deviations, the defect concentration and electrostatic-potential profiles predicted by the NPP model are presented in Figure 10. Clearly, the variation in the profiles is more significant across the membrane thickness

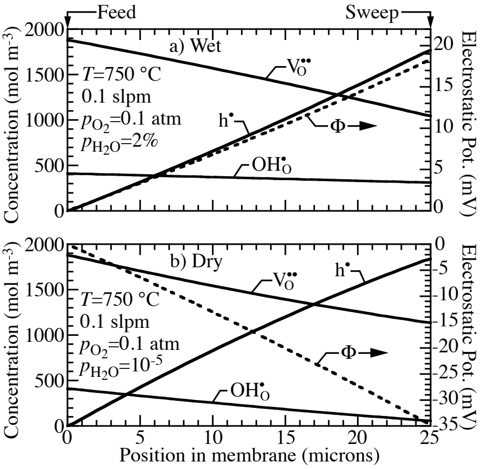

Figure 10: Defect-concentration and electrostatic-potential profiles predicted by the NPP model within the membrane. In both cases, the O_2 partial pressure in the sweep gas is p_{O_2} = 0.1 atm. The sweep gas in the wet case has p_{H_2O} = 0.02 atm and in the dry case $p_{H_2O} = 10^{-5}$ atm. The membrane thickness is 25 μm, the sweep rate is 0.1 slpm (3.77×10^{-5} kg s^{-1} m^{-2}), and the temperature is 750 °C.

than in the nominal case (cf., Fig. 5). The oxygen vacancy concentration decreases toward the oxidizing sweep side of the membrane, and is overtaken by electron holes as the dominant charge-compensating positive defect close to the sweep-side surface. In comparison, the Integral model which assumes that oxygen vacancies are majority defects throughout the membrane interior, predicts a much higher hole concentration on the sweep side surface (on the order of 3000 mol m^{-3}). The relative difference in the predicted hole concentration at the sweep surface between the models is consistent with the observed difference in proton flux under wet oxidizing sweep conditions (cf., Fig. 10a). The larger deviation under dry sweep conditions is due to additional inaccuracies introduced to the Integral model by the mathematical simplification when evaluating the integral in Eq. 45 with significant variations in both p_{H_2O} and p_{H_2}. Such behavior was also observed in Figure 8.

9.5. Model comparisons and implications

Quantitative comparison of the Integral and NPP models shows excellent agreement when the membrane is exposed to small gas-phase variations across the membrane, as in the nominal case. Under these circumstances, the electroneutrality assumptions and the derived functional forms of all partial conductivities in the Integral model are valid and consistent with the more general NPP formulation. For example, with an increasingly oxidizing sweep side (assuming reducing conditions on the feed side), assumptions used in the Integral model become less valid, leading to higher predicted fluxes compared to the NPP model. Introduction of water vapor differences across the membrane also causes differences in the predicted defect fluxes. These differences are attributed to the mathematical error associated with evaluating integral in Eq. 45 with two or more partial-pressure variations across the membrane. The Integral model assumes that the ionic fluxes can be considered as state functions in order to separate the contour Integral over two independent thermodynamic parameters. Yoo and Martin [31] showed that the proton flux could indeed be considered path-independent for the special case of $2[V_O^{\bullet\bullet}] = [Y'_{Zr}]$. Thus, the mathematical error associated with the Integral model increases as the sweep side becomes increasingly oxidizing and the concentration of electron holes contributes significantly to the electroneutrality.

Thus, for systems exposed to increasingly large composition variations across the membrane, the Integral model in its current form should be viewed as increasingly qualitative. Although it certainly predicts all the correct trends, the Integral model predictions depart quantitatively from those of the NPP model. The Integral model is a valuable tool for the qualitative and quantitative interpretation of gas phase and defect fluxes under most conditions. Because it is analytical and directly related to measurable parameters (e.g., conductivities), the Integral model may be the preferred tool for interpreting experimental flux measurements. However, there are also circumstances with large composition variations across the membrane where the NPP models should be preferred for quantitative predictions. In these cases, the use of computational models and lack of analytical expressions is warranted.

In addition to the direct model comparisons, results from both the Integral and NPP models show the importance of coupled interactions between gas-phase compositions, surface chemistry, membrane thickness, sweep flow rates, etc. Understanding these interactions is central to the quantitative evaluation and interpretation of experimental observations. Especially when investigating materials such as doped barium cerates and zirconates, with three or more possible charge-carrying defects, it is important that the models have quantitative predictive capability.

10. Summary and conclusions

Doped ceramic oxides with mixed ion-electron conduction can be used as membranes in numerous applications. Depending upon the gas-phase environments across the membrane, there can be effective gas-phase transport of hydrogen, oxygen, and steam. There is a need to develop predictive models that can be used to assist evaluation of property measurements in the laboratory and to assist the design and development of practical technology. The present paper directly compares two models, one based on an Integral formulation and the other based on a Nernst–Planck–Poisson (NPP) formulation. Both models predict defect and gas-phase fluxes as functions of the gas-phase environments across the membrane. Evaluation of fluxes from the Integral method is essentially analytic, and hence more easily used in most circumstances. The NPP method requires the computational solution of coupled, nonlinear, differential equations. The NPP approach is more general, requiring fewer approximations than the Integral approach.

In all cases, both models predict qualitatively similar results. Direct model comparisons show that the two models agree quantitatively when the membrane is exposed to small gas-phase variations across the membrane. In these case, assumptions needed in the Integral formulation are shown to be valid. However, flux predictions between the NPP and Integral can be significantly different when there are large variations in gas composition across the membrane, such as when one side of the membrane is a reducing environment and the other side is oxidizing. Both models show the importance of representing and understanding the nonlinear coupled interactions between gas-phase compositions, membrane transport properties, physical attributes (e.g., thickness), and gas flow rates.

Although both models are found to be suitable for interpreting experiments (e.g., Fig. 1) under most circumstances, it is also noted that the NPP models are more general and more extendible than the Integral models. For example, in developing technology applications (e.g., fuel cells, electrolyzers, membrane reactors) there is a need to incorporate transient responses, surface chemical kinetics, and large variations in gas-phase environments. In these cases, the added complexity of computational simulation needed for the NPP approach is warranted.

11. Acknowledgements

This publication has been supported by the BIGCCS Centre, under the Norwegian research program Centres for Environment-friendly Energy Research (FME). The authors acknowledge the following partners for their contributions: Aker Solutions, ConocoPhilips, Det Norske Veritas, Gassco, Hydro, Shell, Statkraft, Statoil, TOTAL, GDF SUEZ and the Research Council of Norway (193816/S60). The research at the Colorado School of Mines (CSM) was supported by the Office of Naval Research via grant N00014-08-1-0539. We are especially grateful for extensive and insightful discussions with Prof. Truls Norby (University of Oslo), as well as numerous insightful discussions with Prof. Ryan O'Hayre (CSM) and Dr. Grover Coors (CoorsTek, Inc.). We also acknowledge close interactions with faculty and students in the Colorado Fuel Cell Center who are working on experimental aspects of the ceramic membrane development. These include Profs. Neal Sullivan and Sandrine Ricote, and students Wade Rosensteel and Sean Babiniec.

12. References

[1] H.-I. Yoo, J.-K. Kim, and C.-E. Lee. Electrical conductivity relaxations and chemical diffusivities of $BaCe_{0.95}Yb_{0.05}O_{2.975}$ upon hydration and oxidation. *J. Electrochem. Soc.*, 156:B66–B73, 2009.

[2] H. Matsumoto, T. Shimura, T. Higuchi, H. Tanaka, K. Katahira, T. Otake, T. Kudo, K. Yashiro, A. Kaimai, T. Kawada, and J. Mizusaki. Protonic-electronic mixed conduction and hydrogen permeation in $BaCe_{0.9-x}Y_{0.1}Ru_xO_{3-\alpha}$. *J. Electrochem. Soc.*, 152:A488–A492, 2005.

[3] T. Norby and R. Haugsrud. Dense ceramic membranes for hydrogen separation. In A.F. Sammells and M.V. Mundschau, editors, *Nonporous inorganic membranes*. Wiley-VCH Verlag GmhH & Co., Weinheim, Germany, 2006.

[4] M. Matsuka, R.D. Braddock, H. Matsumoto, T. Sakai, I.E. Agranovski, and T. Ishihara. Experimental and theoretical studies of hydrogen permeation for doped strontium cerates. *Solid State Ionics*, 181:1328–1335, 2010.

[5] B.A. van Hassel, T. Kawada, N. Sakai, H. Yokokawa, M. Dokiya, and H.J.M. Bouwmeester. Oxygen permeation modelling of perovskites. *Solid State Ionics*, 66:295–305, 193.

[6] S.J. Song, E.D. Wachsman, J. Rhodes, S.E. Dorris, and U. Balachandran. Numerical modeling of hydrogen permeation in chemical potential gradients. *Solid State Ionics*, 164:107–116, 2003.

[7] H. Cohen and J.W. Cooley. The numerical solution of the time-dependent Nernst–Planck equations. *Biophysical J.*, 5:145–162, 1965.

[8] R.P. Buck. Kinetics of bulk and interfacial ionic motion: Microscopic basis and limits for the Nernst–Planck equation applied to membrane systems. *J. Membrane Sci.*, 17, 1984.

[9] J. Bobacka, A. Ivaska, and A. Lewenstam. Potentiometric ion sensors. *Chem. Rev.*, 108:329–351, 2008.

[10] J.J. Jasielec, T. Sokalski, R. Filipek, and A. Lewenstam. Comparison of different approaches to the description of the detection limit of ion-selective electrodes. *Electrochimica Acta*, 55:6836–6848, 2010.

[11] B. Grysakowski, J.J. Jasielec, B. Wierzba, T. Sokalski, A. Lewenstam, and M. Danielewski. Electrochemical impedance spectroscopy (EIS) of ion sensors: Direct modeling and inverse problem solving using the Nernst-Planck-Poisson (NPP) model and the HGS(FP) optimization strategy. *J. Electroanalytical Chem.*, 662:143–149, 2011.

[12] M.Z. Bazant, K. Thornton, and A. Ajdari. Diffuse-charge dynamics in electrochemical systems. *Phys. Rev. E*, 70:021506, 2004.

[13] M.Z. Bazant, K.T. Chu, and B.J. Bayly. Current-voltage relations for electrochemical thin films. *SIAM J. Appl. Math.*, 65:1463–1484, 2005.

[14] K.T. Chu and M.Z. Bazant. Nonlinear electrochemical relaxation around conductors. *Phys. Rev. E*, 74:011501, 2006.

[15] P.M. Biesheuvel, M. van Soestbergen, and M.Z. Bazant. Imposed currents in galvanic cells. *Electrochimica Acta*, 54:4857–4871, 2009.

[16] L.H. Olesen, M.Z. Bazant, and H. Bruus. Strongly nonlinear dynamics of electrolytes in large AC voltages. *Phys. Rev. E*, 82:011501, 2010.

[17] R.J. Kee, H. Zhu, B.W. Hildenbrand, E. Völlestad, M.D. Sanders, and R.P. O'Hayre. Modeling the steady-state and transient response or polarized and non-polarized proton-conducting doped-perovskite membranes. *J. Electrochem. Soc.*, 160:F290–F300, 2013.

[18] N. Bonanos. Transport properties and conduction mechanism in high-temperature protonic conductors. *Solid State Ionics*, 53-56:967–974, 1992.

[19] G. Ma, T. Shimura, and H. Iwahara. Ionic conduction and nonstoichiometry in $Ba_xCe_{0.90}Y_{0.10}O_{3-\alpha}$. *Solid State Ionics*, 110:103–110, 1998.

[20] H. Iwahara, T. Esaka, H. Uchida, and N. Maeda. Proton conduction in sintered oxides and its application to steam electrolysis for hydrogen production. *Solid State Ionics*, 3-4:359–363, 1981.

[21] H. Iwahara, T. Esaka, H. Uchida, T. Yamauchi, and K. Ogaki. High temperature type protonic conductor based on $SrCeO_3$ and its application to the extraction of hydrogen gas. *Solid State Ionics*, 18-19:1003–1007, 1986.

[22] K.-D. Kreuer. Proton conductivity: Materials and applications. *Chemistry of Materials*, 8:610–641, 1996.

[23] X. Qi and Y.S. Li. Electrical conduction and hydrogen permeation through mixed proton-electron conducting strontium cerate membranes. *Solid State Ionics*, 130:149–156, 1986.

[24] S. Zhan, X. Zhu, B. Ji, W. Wang, X. Zhang, J. Wang, W. Yang, and L. Lin. Preparation and hydrogen permeation of $SrCe_{0.95}Y_{0.05}O_{3-\delta}$ asymmetrical membranes. *J. Membrane Sci.*, 340:241–248, 2009.

[25] T. Shimura, S. Fujimoto, and H. Iwahara. Proton conduction in non-perovskite-type oxides at elevated temperatures. *Solid State Ionics*, 143:117–123, 2001.

[26] R.C.T. Slade and N. Singh. Systematic examination of hydrogen ion conduction in rare-earth doped barium cerate ceramics. *Solid State Ionics*, 46:111–115, 1991.

[27] R.C.T. Slade and N. Singh. The perovskite-type proton-conducting solid electrolyte $BaCe_{0.90}Y_{0.10}O_{3?\alpha}$ in high temperature electrochemical cells. *Solid State Ionics*, 61:111–114, 1993.

[28] H. Iwahara, T. Yajima, T. Hibino, K. Ozaki, and H. Suzuki. Protonic conduction in calcium, strontium and barium zirconates. *Solid State Ionics*, 61:65–69, 1993.

[29] K. Yashiro, S. Akoshima, T. Kudo, M. Oishi, H. Matsumoto, K. Sato, T. Kawada, and J. Mizusaki. Electrical conductivity and chemical diffusion in perovskite-type proton conductors in H_2-H_2O gas mixtures. *Solid State Ionics*, 192:76–82, 2011.

[30] R.J. Kee, M.E. Coltrin, and P. Glarborg. *Chemically Reacting Flow: Theory and Practice*. Wiley, Hoboken, NJ, 2003.

[31] H.-I. Yoo and M. Martin. On the path-dependence of the open-cell voltage of a galvanic cell involving a ternary or multinary compound with multiple mobile ionic species under multiple chemical potential gradients. *Phys. Chem. Chem. Phys.*, 12:14699–14705, 2010.

[32] K.D. Kreuer, E. Schönherr, and J. Maier. Proton and oxygen diffusion in baceo3 based compounds: A combined thermal gravimetric analysis and conductivity study. *Solid State Ionics*, 70-71:278–284, 1994.

[33] K.D. Kreuer. Aspects of the formation and mobility of protonic charge carriers and the stability of perovskite-type oxides. *Solid State Ionics*, 125:285–302, 1999.

[34] J. Crank. *The Mathematics of Diffusion*. Oxford University Press, Oxford, UK, 1975.

Appendix A. Ambipolar transport

Even in MIEC materials that can support transport of three or more defects, circumstances are often encountered where the transport is dominated by only two defects. This ambipolar limit leads to interesting simplifications of the transport equations. To illustrate the simplifications, consider only two charge-carrying defects, generically called "A" and "B." For example, consider a material such as BZY20 where the defects could be protons $\mathrm{OH}_\mathrm{O}^{\bullet}$ and oxygen vacancies $\mathrm{V}_\mathrm{O}^{\bullet\bullet}$. In this case, $z_{\mathrm{OH}_\mathrm{O}^{\bullet}} = 1$ and $z_{\mathrm{V}_\mathrm{O}^{\bullet\bullet}} = 2$.

For this two-species situation, the electroneutrality constraint (i.e., $\sum z_k[X_k] = 0$) provides that

$$z_\mathrm{A}[\mathrm{A}] + z_\mathrm{B}[\mathrm{B}] = \text{Constant}, \tag{A.1}$$

where for a materials such as BZY20, the constant is the immobile dopant concentration (cf., Eq. 5). It follows directly that the concentration gradients are related as

$$z_\mathrm{A}\nabla[\mathrm{A}] = -z_\mathrm{B}\nabla[\mathrm{B}]. \tag{A.2}$$

The total charge flux resulting from transport of two defects (i.e., $\mathbf{J}^\mathrm{c} = \sum_{k=1} z_k F \mathbf{J}_k$) may be written as

$$\begin{aligned} \mathbf{J}^\mathrm{c} = &- z_\mathrm{A} F D_\mathrm{A}\left(\nabla[\mathrm{A}] + \frac{z_\mathrm{A}F}{RT}[\mathrm{A}]\nabla\Phi\right) \\ &- z_\mathrm{B} F D_\mathrm{B}\left(\nabla[\mathrm{B}] + \frac{z_\mathrm{B}F}{RT}[\mathrm{B}]\nabla\Phi\right). \end{aligned} \tag{A.3}$$

The electrostatic-potential gradient can be factored to yield

$$\mathbf{J}^\mathrm{c} = -\sigma\nabla\Phi - \{z_\mathrm{A} F D_\mathrm{A}\nabla[\mathrm{A}] + z_\mathrm{B} F D_\mathrm{B}\nabla[\mathrm{B}]\}, \tag{A.4}$$

where the conductivity σ is defined to be

$$\sigma = \frac{z_A^2 F^2}{RT} D_A[\mathrm{A}] + \frac{z_B^2 F^2}{RT} D_B[\mathrm{B}]. \tag{A.5}$$

Because charge neutrality requires $\mathbf{J}_c = 0$, an expression for the electrostatic-potential gradient can be obtained as

$$-\sigma \nabla \Phi = z_A F D_A \nabla[\mathrm{A}] + z_B F D_B \nabla[\mathrm{B}]. \tag{A.6}$$

Using this equation for the electrostatic-potential gradient, defect transport flux of [A] can be represented as

$$\mathbf{J}_A = -\frac{\left(z_A^2[\mathrm{A}] + z_B^2[\mathrm{B}]\right) D_A D_B}{z_A^2 D_A[\mathrm{A}] + z_B^2 D_B[\mathrm{B}]} \nabla[\mathrm{A}] = -\mathcal{D}\nabla[\mathrm{A}]. \tag{A.7}$$

The ambipolar diffusion coefficient is defined to be

$$\mathcal{D} \equiv \frac{\left(z_A^2[\mathrm{A}] + z_B^2[\mathrm{B}]\right) D_A D_B}{z_A^2 D_A[\mathrm{A}] + z_B^2 D_B[\mathrm{B}]}. \tag{A.8}$$

Considering transport of two illustrative defects ($\mathrm{OH}_\mathrm{O}^\bullet$ and $\mathrm{V}_\mathrm{O}^{\bullet\bullet}$) within BZY20 under a steam environment, the ambipolar diffusion coefficients for the proton transport can be represented as

$$\mathcal{D}_{\mathrm{OH}_\mathrm{O}^\bullet} = \frac{\left([\mathrm{OH}_\mathrm{O}^\bullet] + 4[\mathrm{V}_\mathrm{O}^{\bullet\bullet}]\right) D_{\mathrm{OH}_\mathrm{O}^\bullet} D_{\mathrm{V}_\mathrm{O}^{\bullet\bullet}}}{D_{\mathrm{OH}_\mathrm{O}^\bullet}[\mathrm{OH}_\mathrm{O}^\bullet] + 4 D_{\mathrm{V}_\mathrm{O}^{\bullet\bullet}}[\mathrm{V}_\mathrm{O}^{\bullet\bullet}]}. \tag{A.9}$$

An alternative expression can be written in terms of the hydration extent $\chi = \left[\mathrm{OH}_\mathrm{O}^\bullet\right] / \left[\mathrm{Y}_\mathrm{Zr}'\right]$ as [32, 33]

$$\mathcal{D}_{\mathrm{OH}_\mathrm{O}^\bullet} = \frac{(2-\chi)\, D_{\mathrm{OH}_\mathrm{O}^\bullet} D_{\mathrm{V}_\mathrm{O}^{\bullet\bullet}}}{\chi D_{\mathrm{OH}_\mathrm{O}^\bullet} + 2\,(1-\chi)\, D_{\mathrm{V}_\mathrm{O}^{\bullet\bullet}}}. \tag{A.10}$$

The hydration extent χ represents the fraction of extrinsic oxygen vacancies occupied by protons.

Generally speaking, the defect conservation equation for [A] can be expressed as

$$\frac{\partial[\mathrm{A}]}{\partial t} = \nabla \cdot \mathbf{J}_A = \nabla \cdot \mathcal{D}\nabla[\mathrm{A}], \tag{A.11}$$

which does not explicitly appear to incorporate a migration contribution. Nevertheless, although subsumed into $\mathcal{D}$, the migration contribution is included as is the local electric-potential gradient. The analogous conservation equation is easily derived for "B." That is,

$$\frac{\partial[\mathrm{B}]}{\partial t} = \nabla \cdot \mathcal{D}\nabla[\mathrm{B}]. \tag{A.12}$$

The ambipolar formulation appears to be straightforward diffusion equation, albeit with the ambipolar diffusion coefficient being a combination of the two individual defect diffusion coefficients. One advantage is that this equation can be solved analytically using classical techniques such as separation of variables [34]. A disadvantage, however, is the fact that the ambipolar diffusion coefficient depends upon the local defect concentrations (Eq. A.8). Thus, when the defect composition varies within the membrane the ambipolar diffusion coefficient is not constant even if the individual defect diffusion coefficients are constants. Spatial variation of the ambipolar diffusion coefficient significantly limits the availability of analytic solutions to the transport equations.

6. Discussion

The articles presented in this thesis address various aspects related to the fundamental properties of proton conducting hydrogen transport membranes, with emphasis on the novel material class LnWO. Manuscript I presented fabrication of thin film LWO56 by Pulsed Laser Deposition, and subsequent structural and electrical characterization. In Manuscript II, the hydrogen permeation properties of Mo-substituted LWO were investigated, while Manuscripts III and IV presented cation diffusion studies of the LWO system to evaluate long-term kinetic stability under operating conditions for membrane applications. Manuscript V describes mathematical modelling of mixed conducting oxides under an electrochemical potential gradient. This chapter will connect and discuss the individual manuscripts in a broader context, with focus on the viability of LnWO materials as hydrogen transport membranes, and fundamental aspects of proton conducting membranes and their role in future applications.

6.1. LnWO-system as a hydrogen transport membrane

6.1.1 Bulk transport of majority charge carriers

Thin film fabrication and characterization (Manuscript I) showed that dense and uniform films of LWO can be deposited successfully by PLD. The films crystallize in the fluorite-type structure of LWO with a slightly larger cell parameter and lower proton conductivity than bulk LWO. The cell parameter relaxed towards that of bulk LWO upon heating the films above 800 °C. Unfortunately, annealing at these temperatures also resulted in pinhole formation in the LWO films. Thus, electrical characterization became increasingly difficult towards the higher temperatures due to electrode degradation and short-circuits between the top electrode and the Pd substrate.

Dense and seemingly uniform films of LWO were also deposited on porous substrates by PLD (cf. Figure 4.2). Unfortunately, pinhole formation during annealing caused increased porosity and pinhole propagation in the LWO films, which made it impossible to maintain a gas tight and leak-free film for hydrogen permeation measurements. Therefore, hydrogen permeation was measured on bulk pellets of Mo-substituted LWO54 (LWMo), which have been found to exhibit higher electronic conductivity under reducing conditions as compared to nominally undoped LWO [42, 43].

Figure 6.1 compares the hydrogen permeabilities of LWMo, LWO56 [41] and LWO55 [67] measured using wet hydrogen as feed gas and dry inert sweep gas. The effect of partial Mo-substitution is noticeable, particularly below 800 °C where hydrogen permeation in LWO is limited by the electronic conductivity. For LWMo in the same temperature range, the proton conductivity was identified as the rate limiting factor for hydrogen permeation. Predicted hydrogen permeabilities based on the integral model described in Manuscripts II and VI, with partial conductivities from the work of Magrasó [43] as input parameters, are also included in Figure 6.1. The modelled fluxes are in good agreement with the measured hydrogen permeation rates in LWMo and LWO. Based on the ambipolar transport properties of the LnWO system, it is apparent that LWMo is an attractive candidate material for hydrogen separation applications. Nominally undoped LWO may be better suited as an electrolyte material in proton conducting fuel and electrolyser cells that operate below 600 °C, where its n-type conductivity is much less significant.

Below 800 °C, the measured permeability of LWO56 is significantly lower than the predicted values, with relatively high activation energy. This could indicate that the measured hydrogen flux for LWO56 was limited by surface kinetics at these temperatures, similar to what was observed for LWMo2 in Manuscript II. Such an effect could also explain the larger activation energy for n-type conductivity in LWO56 obtained from curve fitting of flux measurements (350 $kJ\cdot mol^{-1}$) as compared to the value obtained from conductivity measurements (275 $kJ\cdot mol^{-1}$) [46]. The measurements on

LWO55 by Escolástico *et al.* [67] were conducted after screen printing a porous platinum layer on both membrane surfaces, and should as such represent the bulk hydrogen permeability of the material. Thus, the increased hydrogen permeability in LWMO can be directly related to the increased electronic conductivity, and moreover confirm that the proton conductivity is not significantly affected by partial Mo-substitution in LWO.

Recent work by Escolástico *et al*. [68] reported hydrogen permeation in 20 at% Re- and Mo- substituted LWO55 (LWRO55 and LWMO55, respectively). In their work, they found that hydrogen permeation below 750 °C was not limited by electronic conductivity, and reported a maximum hydrogen permeability of 0.007 $mL·cm^{-1}·min^{-1}$ for $La_{5.5}W_{0.8}Re_{0.2}O_{11.25}$ which represents the highest reported value for a single phase proton conducting hydrogen transport membrane. The reported total conductivities of these materials under reducing conditions are similar to those reported for LWMo [42, 43]. It is therefore surprising to observe such an enhanced permeability in LWRO55 and LWMO55 compared to what was found for LWMo in Manuscript II. In the investigations of LWReO55, all measurements were conducted using wet sweep gas. Accordingly, hydrogen formation due to water splitting may also contribute to the enhanced, apparent hydrogen flux. Moreover, the measurements were conducted using sweep flow rates of 150 $mL·min^{-1}$ compared to the 5-15 $mL·min^{-1}$ used in Manuscript II. Thus, the hydrogen partial pressures on the sweep side of the membrane should be an order of magnitude lower, which could have an influence on the measured hydrogen permeabilities, as discussed in Chapter 6.3. For LWMO55, the conductivity measurements indicated higher oxide ion conductivity and lower proton conductivity than in the undoped LWO55. Still, the hydrogen permeability under dry sweep conditions – where only ambipolar proton-electron conductivity should contribute to the measured hydrogen flux – was significantly enhanced compared to LWO55, which does not correspond with decreased proton conductivity. Clearly, there are unresolved questions regarding the underlying processes that govern defect transport and hydrogen permeation in partially substituted LWO.

As discussed previously, the LWO-based materials display considerable oxide ion conductivity above 800 °C [37, 69], which under wet sweep conditions results in hydrogen formation in the sweep gas due to ambipolar transport of oxide ions and electrons and water splitting in the sweep. The potential positive and negative effects of oxide ion conductivity and water splitting effects in proton conducting hydrogen transport membranes will be discussed in further detail in Chapter 6.4.

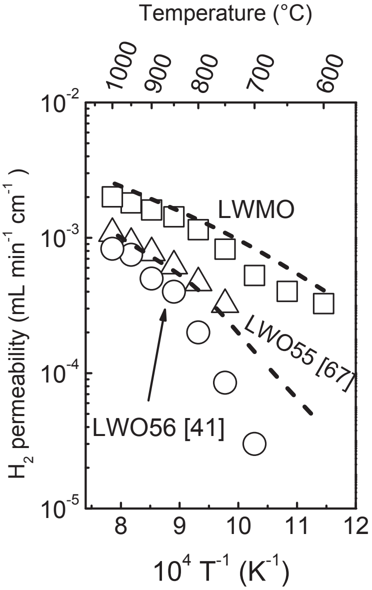

Figure 6.1 – Hydrogen permeability of LWMo, LWO56 [41] and LWO55 [67] using dry inert sweep gas and wet H_2 as feed gas. The lines indicate predicted fluxed based on partial conductivities for LWMo and LWO54 from the work of Magrasó [43].

6.1.2 Surface kinetics

The work in Manuscript II revealed that hydrogen permeation was limited by surface kinetics for a 0.65 mm thick pellet (LWMo2), and significantly enhanced by the addition of a porous Pt layer on both surfaces. Large activation energies and Δp_{H_2}-dependencies also indicated that surface kinetics influenced the measured hydrogen flux for a 1.3 mm thick pellet at low feed side p_{H_2}. These findings are surprising considering recent work by Hancke *et al.*, where the surface hydrogen exchange rate was measured on both LWO and LWMo [70]. The authors calculated the critical thickness of LWMo (i.e. the thickness below which surface kinetics would limit hydrogen permeation) to approximately 30 μm at 700 °C. Thus, the observed surface limitations for a much thicker membrane were quite unexpected. Especially considering that reduced molybdenum (Mo^{4+}) was observed on the surfaces of LWMo1 by XPS analysis after the permeation measurements (Manuscript II), which Hancke *et al.* speculated as the origin of the fast surface kinetics [70].

Another interesting observation was the similarity between the temperature and partial pressure dependencies for hydrogen permeation in the surface limited LWMo2 sample and the surface exchange rates measured for nominally pure LWO by Hancke *et al.* [70]. One may therefore speculate whether the surface of the LWMo membrane measured in Manuscript II display similar properties as that of nominally pure LWO. The slow surface kinetics could also be related to the observed degradation and secondary phase formation in LWMo after the hydrogen permeation experiments. The secondary phases may occupy and effectively reduce the number of catalytically active LWMo sites and thus reduce the surface exchange rates.

Clearly there is a need for increased understanding of the surface kinetics on LWMo surfaces to elucidate the origin of the discrepancy between the critical thickness estimated by Hancke *et al.* and the permeation measurements presented in Manuscript II. These findings also illustrate the importance of studying the surface kinetics of proton conducting oxides when moving towards commercialization, in order to provide fundamental understanding of the elementary reactions occurring on the membrane surfaces and input parameters for predictive modelling of complete membrane reactor applications.

6.1.3 Cation diffusion and kinetic stability

In Manuscripts III and IV, cation diffusion in the LWO-based system was investigated by means of inter-diffusion and chemical tracer diffusion experiments. Both studies revealed that the bulk diffusivities of W and La (and tracer diffusivities of Nd and Mo) were similar over the entire temperature range investigated (1000-1350 °C). The bulk diffusion coefficients in LWO are in the order of 10^{-16} $cm^2 \cdot s^{-1}$ close to 1000 °C, which is similar or lower than many perovskite-based oxygen transport membranes. However, the bulk diffusivities are significantly higher and the activation energies lower than in other oxygen-deficient fluorites such as zirconia. The latter is most likely due to the defective nature of the fluorite-type LWO structure, where there is a degree of disorder in both the anion and cation sublattice. Moreover, it has been shown that there are strong repulsive forces prohibiting direct cation jumps from one cation site to another in the cubic fluorite structure [71]. In LWO, the cations on the La2-sublattice reside in a distorted cube with seven-fold coordination. Thus, the repulsive forces related to the cation jump are weakened, and the migration enthalpy decreased. The higher diffusivities of LWO are not entirely unexpected considering the much higher melting temperatures of ceria and zirconia [72].

Enhanced grain boundary diffusion was exclusively observed for La site, with diffusion coefficients 3-4 orders of magnitude larger than the bulk diffusion coefficients. In Manuscript IV we suggested that depletion of W^{6+} and Mo^{6+} in the space charge region could account for the lack of grain boundary diffusion of these species. It was also speculated that cation vacancy segregation near the grain boundary core was the cause for the faster La diffusion. In other oxygen-deficient fluorites, segregation of acceptor dopants near the grain boundary core has been observed due to the electric field in the space charge region [73-75]. However, in LWO where there are no acceptor dopants, other negative defects will be attracted towards the positive grain boundary core. Indeed, coupled experimental and computational analysis of fluorite bi-crystals revealed that cation vacancies and yttrium dopants are stabilized near the oxygen vacancies in the core [73]. Hence, an interesting follow-up study could comprise careful investigation of LWO grain boundaries by means of high resolution transmission electron microscopy and *ab initio* modelling to elucidate the structure and composition near the grain boundary core.

The kinetic stability towards cation diffusion related degradation in LWO-based membranes can be evaluated based on the self-diffusion coefficients of La and W. In the following discussion, estimated self-diffusion coefficients based on the interdiffusion and chemical tracer diffusion coefficients presented in Manuscript III and IV forms the basis for a qualitative discussion of degradation phenomena in LWO:

$$D_{\mathrm{bulk}}^{\mathrm{La,W}} = 1 \cdot 10^{-16}\,\mathrm{cm}^2\,\mathrm{s}^{-1} \quad , \tag{6.1}$$

$$D_{\mathrm{gb}}^{\mathrm{La}} = 1 \cdot 10^{-12}\,\mathrm{cm}^2\,\mathrm{s}^{-1} \quad , \tag{6.2}$$

Although the bulk diffusivities of La and W are similar, the grain boundary diffusivity of La will yield an enhanced effective diffusion coefficient according to

$$D_{eff} = (1-r)D_{\mathrm{bulk}} + rD_{\mathrm{gb}} \quad , \tag{6.3}$$

where $r \approx \frac{3\omega}{d}$. Accordingly, the effective diffusion coefficient can be calculated assuming a grain boundary width (ω) of 1 nm and a grain size (d) of 10 µm:

$$D_{eff}^{\mathrm{La}} = 4 \cdot 10^{-16}\ \mathrm{cm}^2\ \mathrm{s}^{-1} \quad , \qquad (6.4)$$

Firstly, we can identify the ratio of the cation diffusivities as $\frac{D_{eff}^{\mathrm{W}}}{D_{eff}^{\mathrm{La}}} = \frac{1}{4}$. According to a similar treatment as presented in Chapter 3, demixing and decomposition should occur in LWO if the diffusivity ratio is below ½. We should therefore expect some degree of lanthanum enrichment towards the high p_{O_2}-side of the membrane after prolonged exposure to a p_{O_2} gradient. Still, kinetic demixing and decomposition is rate limited by the fastest moving species and it would take up to 40 years to reach steady state kinetic demixing for a 10 μm thick membrane based on the effective La diffusivity calculated in Equation 6.4. However, kinetic decomposition or performance degradation during the transient demixing may still influence the performance of LWO membranes.

In Manuscript II, we observed a decrease in hydrogen permeation over time and indications of W-rich crystallites on the feed side surface (reducing side) after exposure to a hydrogen gradient at elevated temperatures. This is in accordance with kinetic demixing or decomposition due to faster lanthanum diffusion towards the oxidizing side of the membrane. Degradation due to kinetic demixing or decomposition could further account for the more pronounced degradation in the thinner LWMO membranes, as the driving force for cation diffusion increases with decreasing thickness. These observations are similar to a recent study on the kinetic stability of La_2NiO_4 [55], where preferential diffusion of Ni^{2+} along the grain boundaries resulted in kinetic decomposition and formation of Ni-rich phases on the oxidizing side of the membrane. An initial drop in the oxygen flux was observed before it stabilized for a prolonged period. The authors speculated that formation of a thin blocking La_2O_3 layer on the low p_{O_2}-side could take up some of the imposed $\Delta\mu_{\mathrm{O}_2}$ and effectively reduce oxygen permeation and further decomposition. Thus, one may speculate whether the expected excess lanthanum on the sweep side surface may have formed a thin blocking layer of La_2O_3 similarly as in the case of La_2NiO_4.

Although the data presented in this work serve as indications of the kinetic stability of LWO based membranes, the mechanisms governing cation diffusion in the bulk and along the grain boundaries remain uncertain. Even for heavily studied systems such as zirconia there are still uncertainties regarding the transport facilitating defects and the influence of cation size and charge. It is of particular interest to study the effects of cation stoichiometry on the cation diffusion properties, as this could shed more light on the participating defects and the effect of oxygen vacancy concentration on cation migration. These studies may also aid in further optimizing the LWO stoichiometry in terms of thermodynamic stability in reducing conditions, as formation of secondary phases were observed in LWO after prolonged exposure to reducing conditions at elevated temperatures. Combined theoretical calculations and high resolution transmission electron microscopy on the grain boundary structure and defect chemistry may provide valuable insight on the processes governing grain boundary diffusion – and consequently the kinetic stability.

6.2. Mathematical modelling of mixed ionic-electronic conductors under chemical potential gradients

In Manuscript V (and Appendix A), a mathematical model is developed for mixed proton-electron conducting oxides under electrochemical potential gradients. By formulating the multi-species diffusion problem as a system of ordinary differential equations, it is possible to predict both steady-state and transient behaviour with and without an applied voltage load. The model is based on the Nernst-Planck equation for the flux density of charged species, similar to the more conventional integral formulation commonly used in the literature. In Manuscript V the two models were compared for a number of various conditions to investigate the correspondence between the two methods, using thermodynamic data that results in significant p-type electronic conductivity in oxidizing atmospheres. The predicted partial fluxes of protons and oxide ions from both models were in good qualitative and quantitative agreement when only a small hydrogen gradient was imposed over the membrane. If an additional water vapour gradient was introduced, or the sweep side was made increasingly oxidizing, the two models started to depart.

The discrepancy between the models under these conditions can be rationalized based on the assumptions that are implicitly stated in the integral formulation:

- A simplified electroneutrality condition (e.g. $[\mathrm{OH_O^\bullet}] = [\mathrm{Acc}^{/}]$) was implemented to obtain partial pressure dependencies for the partial conductivities. As the gradients across the membrane become increasingly large, there is no longer one single simplified electroneutrality condition which is valid throughout the membrane for the given thermodynamic parameters.
- The proton and oxide ion flux expressions were assumed to be state functions such that the contour integral involving two independent thermodynamic variables could be divided onto two separate integrals. This assumption is equivalent to saying that the flux expressions are path-independent, as first described by Yoo and Martin [76].

In Manuscript II, the integral formulation was used to predict hydrogen permeability in LWMo based on partial conductivities measured directly by Magrasó [43]. The integral model accurately predicted the qualitative permeation behaviour in LWMo, with a reasonable quantitative agreement with the measured hydrogen fluxes (cf. Figure 6.1). These findings illustrate some of the main advantages of the integral formulation; the input parameters are directly measurable and the mathematics is straightforward with the potential of analytical solutions. As such, the integral model promotes conceptual understanding of the permeation processes, which will be further discussed in Chapter 6.3. Accordingly, the integral formulation will most likely remain the mathematical tool of choice for evaluation of simple permeation experiments, where focus is on understanding the fundamental processes governing the measured permeabilities rather than precise and accurate predictions of transport and concentration profiles for all mobile species.

The more general Nernst-Planck-Poisson (NPP) formulation is better suited for more complex systems where gas phase transport and surface reactions are of vital importance to the permeation properties of the membrane, such as in tubular membrane reactors. The advantage of the NPP model is that it can be readily integrated with already developed software for chemical engineering and gas phase reactions, and the potential of modelling transient behaviour (cf. Figure 6.2). Further, the gas-solid interactions occurring at the membrane surfaces can be readily incorporated once the proper reaction schemes are described. It is therefore clear that the more rigorous models based on partial differential equations are useful when technologies based on mixed ionic electronic conductors are moved towards commercial realization. However, there are many improvements yet to be made, particularly when it comes to determination of consistent thermodynamic parameters for the oxides of interest.

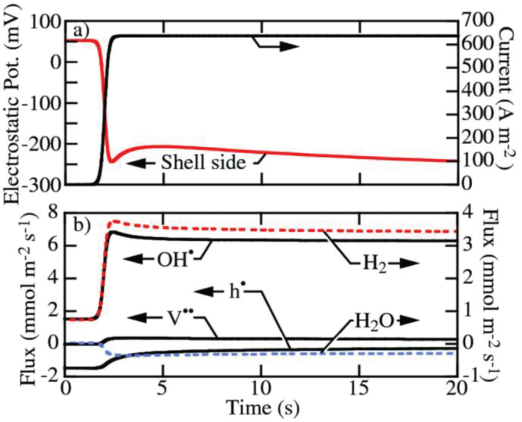

Figure 6.2. Illustration of transient modelling of a proton conducting membrane following a sudden polarization of the membrane. See Appendix for further details.

6.3. Functional dependencies and interpretation of hydrogen permeation measurements

In Manuscript II we noted it was a challenge to relate the partial pressure dependency of hydrogen permeation directly to the defect chemistry and transport properties of oxides that display considerable mixed conduction of three or more species. This is in line with the observations we made in Manuscript V, where the permeation behaviour becomes increasingly complex when the relative contributions of all species are similar in magnitude. In the following we will go deeper into the temperature and partial pressure dependencies of hydrogen permeation in a mixed proton, electron and oxide ion conducting oxide exposed to a hydrogen gradient. We will start by examining the situation where both sides of the membrane are wet, such that there is no gradient in water vapour partial pressure across the membrane.

From Manuscript II and V we recall that the flux of hydrogen gas through a mixed proton-, electron- and oxide ion conductor can be expressed as

$$j_{\mathrm{H_2}} = -\frac{RT}{4F^2L}\int_{\mathrm{I}}^{\mathrm{II}} \sigma_{\mathrm{H^+}} t_{\mathrm{e^-}} \frac{\mathrm{d}\, p_{\mathrm{H_2(g)}}}{p_{\mathrm{H_2(g)}}} - \frac{RT}{4F^2L}\int_{\mathrm{I}}^{\mathrm{II}} \sigma_{\mathrm{O^{2-}}} t_{\mathrm{e^-}} \frac{\mathrm{d}\, p_{\mathrm{O_2(g)}}}{p_{\mathrm{O_2(g)}}} \quad , \qquad (6.5)$$

where I and II represents the hydrogen partial pressures on the sweep and feed side, respectively. The first part of Equation 6.5 represents hydrogen permeation by ambipolar transport of protons and electrons, whereas the latter represents hydrogen formed in the sweep gas as a result of water splitting and transport of oxide ions towards the feed side of the membrane. To obtain an analytical solution to Equation 6.5, assumptions regarding the transport parameters and defect chemistry of the membrane material must be implemented. The following treatment will outline analytical solutions and resulting functional dependencies for hydrogen permeation and water splitting for a selection of simplified electroneutrality conditions.

Consider a membrane where the electronic conductivity is considerably higher than the ionic conductivity ($t_{e^-} \approx 1$), in which oxygen vacancies and protons are the majority defects charge compensated by a constant acceptor concentration, and electrons as minority defects concentration wise. Figure 6.3 provides a simplified schematic illustration of the surface reactions, chemical potential gradients and defect concentration profiles occurring on and within a membrane exposed to a wet reducing feed gas and a wet inert sweep gas under the assumption that the surfaces are in equilibrium with their surrounding atmospheres.

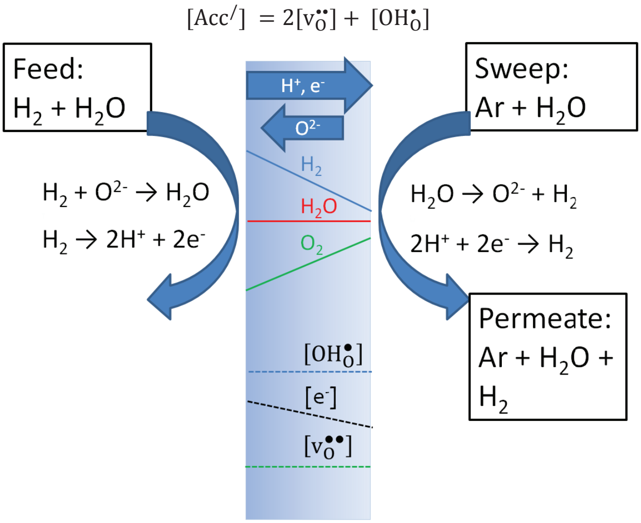
$[\mathrm{Acc}^/] = 2[\mathrm{v}_\mathrm{O}^{\bullet\bullet}] + [\mathrm{OH}_\mathrm{O}^{\bullet}]$
Feed: $H_2 + H_2O$
Sweep: $Ar + H_2O$
H^+, e^-
O^{2-}
H_2
H_2O
O_2
$H_2 + O^{2-} \rightarrow H_2O$
$H_2 \rightarrow 2H^+ + 2e^-$
$H_2O \rightarrow O^{2-} + H_2$
$2H^+ + 2e^- \rightarrow H_2$
Permeate: $Ar + H_2O + H_2$
$[\mathrm{OH}_\mathrm{O}^{\bullet}]$
$[e^-]$
$[\mathrm{v}_\mathrm{O}^{\bullet\bullet}]$

Figure 6.3. Schematic illustration of the chemical potential and defect concentration profiles across a membrane exposed to wet reducing feed and wet inert sweep gas.

Under constant water vapour partial pressure, the proton and oxide ion conductivity will be essentially constant with p_{H_2} and p_{O_2} due to the constant acceptor concentration, and can therefore be placed outside the integral. Equation 6.6 can then be solved analytically as

$$\begin{aligned} j_{\mathrm{H_2}} = & -\frac{RT}{4F^2L}\sigma_{\mathrm{H^+}}\left[\ln p_{\mathrm{H_2(g),II}} - \ln p_{\mathrm{H_2(g),I}}\right] \\ & + \frac{RT}{8F^2L}\sigma_{\mathrm{O^{2-}}}\left[\ln p_{\mathrm{O_2(g),II}} - \ln p_{\mathrm{O_2(g),I}}\right] \ . \end{aligned} \qquad (6.6)$$

When the water vapour partial pressure is the same on the permeate and feed side, the second term in Equation 6.6 can be rewritten in terms of the hydrogen partial pressure by utilizing the H_2-O_2-H_2O equilibrium:

$$\begin{aligned} j_{\mathrm{H_2}} = & -\frac{\mathrm{R}T}{4\mathrm{F}^2L}\sigma_{\mathrm{H^+}}\left[\ln p_{\mathrm{H_2(g),II}} - \ln p_{\mathrm{H_2(g),I}}\right] \\ & - \frac{\mathrm{R}T}{4\mathrm{F}^2L}\sigma_{\mathrm{O^{2-}}}\left[\ln p_{\mathrm{H_2(g),II}} - \ln p_{\mathrm{H_2(g),I}}\right] \end{aligned} \qquad (6.7)$$

Thus, the apparent hydrogen flux (i.e. both hydrogen permeation and water splitting) should be proportional to $\Delta\ln p_{\mathrm{H_2(g)}}$ for materials dominated by n-type conductivity with electrons as minority defects concentration-wise. Provided that the surface is sufficiently fast, the temperature dependency of hydrogen permeation and water splitting will in this case be given by the activation energy of proton conductivity and oxide ion conductivity, respectively.

If on the other hand the electrons are majority defects concentration-wise, we obtain different functional dependencies for the hydrogen flux. When the electrons are charge compensated by oxygen vacancies, the proton conductivity is proportional to $p_{\mathrm{H_2}}^{1/2}$ and the oxide ion conductivity to $p_{\mathrm{H_2}}^{1/3}$. The analytical solution to Equation 6.5 under wet sweep conditions then yields

$$j_{\mathrm{H_2}} = -\frac{RT}{2F^2L}\sigma_{\mathrm{H^+}}^0\left[p_{\mathrm{H_2(g),II}}^{1/2} - p_{\mathrm{H_2(g),I}}^{1/2}\right] - \frac{3\mathrm{R}T}{4\mathrm{F}^2L}\sigma_{\mathrm{O^{2-}}}^0\left[p_{\mathrm{H_2(g),II}}^{1/3} - p_{\mathrm{H_2(g),I}}^{1/3}\right], \qquad (6.8)$$

where $\sigma^0_{\mathrm{H^+}}$ and $\sigma^0_{\mathrm{O^{2-}}}$ are the proton and oxide ion conductivity at standard hydrogen pressure (10^5 Pa), respectively. Thus, depending on whether hydrogen permeation or water splitting dominates the measured apparent hydrogen flux, different $\Delta p_{\mathrm{H_2}}$-dependencies are expected. Finally, if the electrons are charge compensated by protons, the proportionalities are $p^{1/4}_{\mathrm{H_2(g)}}$ for proton conductivity and $p^{1/2}_{\mathrm{H_2(g)}}$ for oxide ion conductivity. Thus, the integration of Equation 6.5 yields

$$j_{\mathrm{H_2}} = -\frac{\mathrm{R}T}{4\mathrm{F}^2L}\sigma^0_{\mathrm{H^+}}\left[p^{1/4}_{\mathrm{H_2(g),II}} - p^{1/4}_{\mathrm{H_2(g),I}}\right] - \frac{\mathrm{R}T}{4\mathrm{F}^2L}\sigma^0_{\mathrm{O^{2-}}}\left[p^{1/2}_{\mathrm{H_2(g),II}} - p^{1/2}_{\mathrm{H_2(g),I}}\right]. \quad (6.9)$$

Until now, I have only discussed materials which display predominantly n-type conductivity. However, many of the studied membrane materials display predominantly proton conductivity ($t_{\mathrm{H+}} \approx 1$) at intermediate temperatures, with electrons as minority defects. Once again, the proton and oxide ion conductivities are independent of $p_{\mathrm{H_2}}$ and $p_{\mathrm{O_2}}$ (assuming constant $p_{\mathrm{H_2O}}$ across the membrane), whereas the n-type electronic conductivity is proportional to $p^{1/2}_{\mathrm{H_2}}$. Thus, the integral may be solved analytically as

$$\begin{aligned} j_{\mathrm{H_2}} = {} & -\frac{\mathrm{R}T}{4\mathrm{F}^2L}\sigma^0_{\mathrm{e^-}}\left[p^{1/2}_{\mathrm{H_2(g),II}} - p^{1/2}_{\mathrm{H_2(g),I}}\right] \\ & -\frac{\mathrm{R}T}{4\mathrm{F}^2L}t_{\mathrm{O^{2-}}}\,\sigma^0_{\mathrm{e^-}}\left[p^{1/2}_{\mathrm{H_2(g),II}} - p^{1/2}_{\mathrm{H_2(g),I}}\right] . \end{aligned} \quad (6.10)$$

Here, $\sigma^0_{\mathrm{e^-}}$ is the electronic conductivity at standard hydrogen partial pressure. In this case the apparent hydrogen flux is proportional to $\Delta p^{1/2}_{\mathrm{H_2}}$, and the temperature dependency for hydrogen permeation is determined by the activation energy for electron conduction. Table 6.1 summarizes the hydrogen partial pressure dependencies for H_2 permeation and H_2O splitting as derived in the above discussion. In most cases, the amount of hydrogen formed on the permeate side (i.e. H_2 permeation + H_2O splitting) displays a dependency on the form $\Delta p^{1/x}_{\mathrm{H_2}}$ where x ranges from two to four. In those cases, the hydrogen partial pressure on the feed side has a large effect on the apparent hydrogen flux, whereas the concentration of hydrogen on the permeate side has a negligible impact. However, in the special case where H_2 permeation and H_2O splitting is proportional to $\Delta\ln p_{H_2(g)}$, feed and permeate side partial pressures have similar impact on the resulting hydrogen flux. Thus, in materials where the electronic species are minority defects, but the conductivity is predominantly electronic, the sweep side hydrogen partial pressure in the permeate gas will affect the measured hydrogen flux significantly. Accordingly, it is possible to increase the hydrogen flux by increasing the flow rate of the inert gas on the sweep side maintaining a lower $p_{H_2,\mathrm{permeate}}$. This furthermore makes it difficult to directly compare hydrogen permeabilities measured using different geometries or sweep flow rates for materials that exhibit a $\Delta\ln p_{H_2}$-dependency on hydrogen permeation.

Table 6.1. Hydrogen partial pressure dependencies for H_2 permeation and H_2O splitting for selected electroneutrality conditions and predominating charge carriers.

	$t_{H+} \approx 1$		$t_{e^-} \approx 1$	
	H_2 permeation	H_2O splitting	H_2 permeation	H_2O splitting
$2[v_O^{\bullet\bullet}] + [OH_O^{\bullet}] = [Acc^{/}]$	$\Delta p_{H_2}^{1/2}$	$\Delta p_{H_2}^{1/2}$	$\Delta\ln p_{H_2(g)}$	$\Delta\ln p_{H_2(g)}$
$[OH_O^{\bullet}] = [e^{/}]$	-	-	$\Delta p_{H_2}^{1/2}$	$\Delta p_{H_2}^{1/3}$
$2[v_O^{\bullet\bullet}] = [e^{/}]$	-	-	$\Delta p_{H_2}^{1/4}$	$\Delta p_{H_2}^{1/2}$

So far, the discussion has been restricted to the functional dependencies for hydrogen permeation when both sides of the membrane are wet, such that there is no gradient in water vapour partial pressure across the membrane. Conversely, if the sweep gas is dry inert gas and the feed gas wet and reducing, the situation becomes more complex. Clearly, there is a gradient in both H_2 and H_2O across the membrane. In addition, an initial gradient in oxygen potential is present due to trace amount of oxygen gas and water vapour in the inert sweep gas. Thus, there are gradients in three gaseous species at the initial stage. These gradients will impose fluxes of the mobile species through the membrane, which will significantly alter the sweep gas compositions. Thus, the partial pressure gradients and the transport properties across the membrane are interdependent parameters that both influence the measured flux. Although a formal treatment of possibilities is outside the scope of this thesis, we will still take a further look into the specific case where the sweep gas is sufficiently dry and inert such that the oxygen potential gradient across the membrane can be considered negligible at steady state. Using this assumption, expressions for the defect concentration profiles across the membrane can be established for a given electroneutrality. Figure 6.4 presents schematically the steady-state gas-phase chemical potential gradients and defect concentration profiles for two simplified electroneutrality conditions; $2[\mathrm{v}_\mathrm{O}^{\bullet\bullet}] = [\mathrm{Acc}^{/}]$ and $[\mathrm{OH}_\mathrm{O}^{\bullet}] = [\mathrm{Acc}^{/}]$.

Once these relations are established, Δp_{H_2}-dependencies of the hydrogen flux for different electroneutrality conditions and transport parameters are readily established by solving the flux equation under dry sweep conditions:

$$j_{\mathrm{H}_2} = -\frac{RT}{4F^2L}\int_{\mathrm{I}}^{\mathrm{II}} \frac{\sigma_{\mathrm{H}^+} \cdot \sigma_{\mathrm{e}^-}}{\sigma_{\mathrm{H}^+} + \sigma_{\mathrm{e}^-}\ \sigma_{\mathrm{O}^{2-}}} \frac{\mathrm{d}\, p_{\mathrm{H}_2(\mathrm{g})}}{p_{\mathrm{H}_2(\mathrm{g})}} \qquad (6.11)$$

A rigorous derivation of these dependencies is tedious and very similar to the derivations presented for the wet sweep case. Thus, the resulting dependencies are presented graphically in Figure 6.5 for various ratios of the proton and electron transport numbers, assuming a constant oxide ion transport number. Figure 6.4 and 6.4 reveals that the Δp_{H_2}-dependencies and defect concentration profiles are significantly affected by the electroneutrality condition. Moreover, Figure 6.5 shows that the Δp_{H_2}-dependencies for the two electroneutrality conditions are inversely dependent on the transport number ratio. For example, the hydrogen flux is proportional to $\Delta p_{\mathrm{H_2}}^{1/2}$ for $t_{\mathrm{e^-}} \approx 1$ and $2[\mathrm{v_O^{\bullet\bullet}}] = [\mathrm{Acc}^{/}]$, whereas the same dependency is obtained for $t_{\mathrm{H^+}} \approx 1$ and $[\mathrm{OH_O^{\bullet}}] = [\mathrm{Acc}^{/}]$. Thus, we cannot conclude anything regarding the transport number ratios of a mixed conducting membrane unless the defect chemistry is well established and vice versa. These observations underline the complexities related to hydrogen flux measurements, and that it is difficult to extract clear and exact conclusions from these measurements if the defect chemistry is not properly and unambiguously established. Another important observation is the similarity between the slopes for the various transport number ratios in the low $p_{\mathrm{H_2}}$ regime. For instance, the slope is proportional to $p_{\mathrm{H_2}}^{2/5}$ for $t_{\mathrm{H^+}} = 0.1$ and $p_{\mathrm{H_2}}^{1/2}$ for $t_{\mathrm{H^+}} = 0.8$ when protons are the charge compensating defects (cf. Figure 6.5a). Thus, it can be difficult to distinguish different dependencies when experimental errors and scatter in the results are considered.

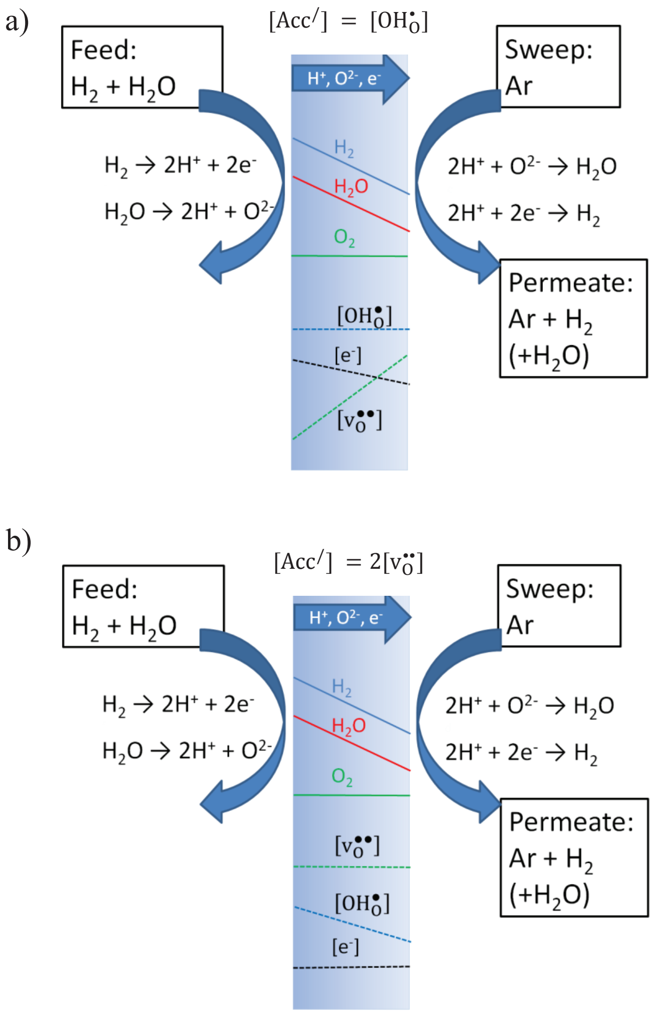
a)
[Acc/] = [OH•O]
Feed:
H2 + H2O
H+, O2-, e-
Sweep:
Ar
H2 → 2H+ + 2e-
H2O → 2H+ + O2-
H2
H2O
O2
2H+ + O2- → H2O
2H+ + 2e- → H2
Permeate:
Ar + H2
(+H2O)
[OH•O]
[e-]
[v••O]
b)
[Acc/] = 2[v••O]
Feed:
H2 + H2O
H+, O2-, e-
Sweep:
Ar
H2 → 2H+ + 2e-
H2O → 2H+ + O2-
H2
H2O
O2
2H+ + O2- → H2O
2H+ + 2e- → H2
Permeate:
Ar + H2
(+H2O)
[v••O]
[OH•O]
[e-]

Figure 6.4. Schematic illustrations of chemical potential gradients and defect concentration profiles for a membrane exposed to wet reducing feed gas and dry inert gas for two different simplified electroneutrality conditions: a) $[\mathrm{OH}_\mathrm{O}^{\bullet}] = [\mathrm{Acc}^{/}]$ and b) $2[\mathrm{v}_\mathrm{O}^{\bullet\bullet}] = [\mathrm{Acc}^{/}]$

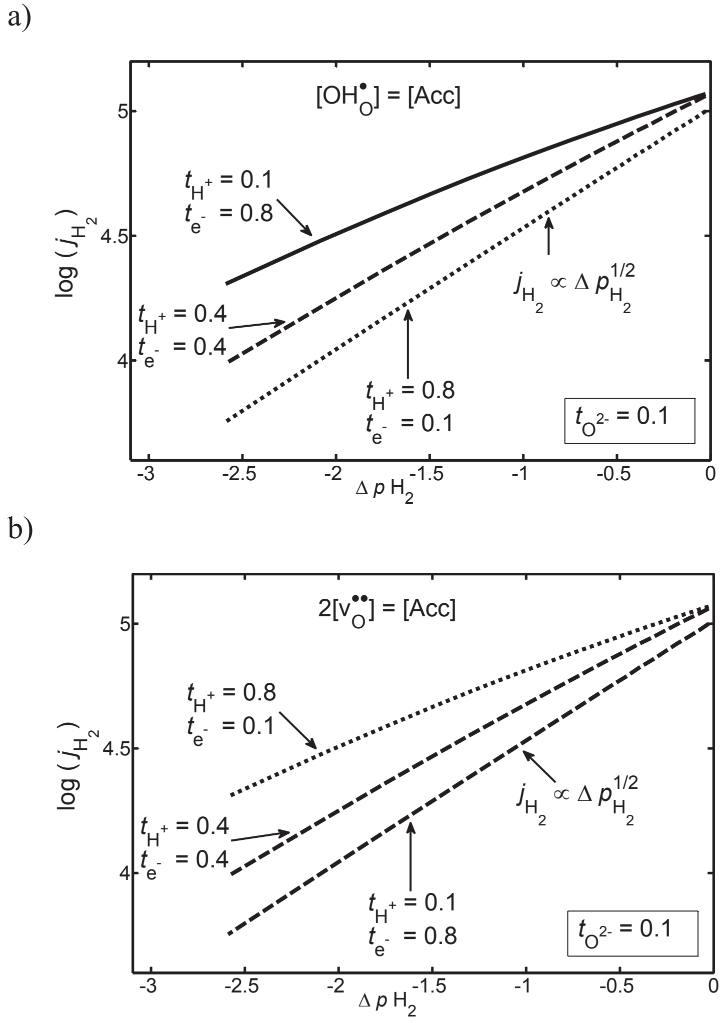

Figure 6.5 - $\Delta p_{\mathrm{H_2}}$-dependencies on the hydrogen flux as a function of proton and electron transport numbers for a) $[\mathrm{OH_O^{\bullet}}] = [\mathrm{Acc}^{/}]$ and b) $2[\mathrm{v_O^{\bullet\bullet}}] = [\mathrm{Acc}^{/}]$

6.4. Proton conducting membranes – applicability and challenges

Eu-doped $SrCeO_3$ has for more than a decade represented the benchmark for mixed proton-electron conducting hydrogen transport membranes in terms of transport properties. The hydrogen flux of LWMo reported in Manuscript II combined with the work of Escolástico *et al.* have shown that even higher permeabilities can be achieved for partially substituted lanthanum tungsten oxide. For LWReO55, a hydrogen flux of 2 mL min^{-1} cm^{-2} was estimated for a 30 µm thick asymmetric membrane, assuming that permeation was limited by bulk transport [68]. Even higher permeabilities are reported for composites of Ni metal and $BaCe_{0.7}Zr_{0.1}Y_{0.2}O_{3-\delta}$ (Ni-BCZY), but these suffer from poor chemical and mechanical stability [77, 78].

Both the dual phase “cermet” composition and the lanthanum tungsten oxides display hydrogen permeation rates far inferior to the novel Pd-based alloys, which are currently being deployed in on-site pilot testing for steam methane reforming with continuous hydrogen removal. Still, the ceramic membranes may offer advantages in terms of chemical and thermal stability that facilitates integration in high temperature processes. For instance, the Hydrogen Membrane Reformer technology suggested by Norsk Hydro incorporates oxygen or air on the sweep side of the hydrogen transport membrane coupled with high temperature and pressure. Thus, metal based membranes are vulnerable towards oxidation and the chemically stable oxides comprise a more suitable alternative. For proton conducting membranes, a target flux of 5 mL min^{-1} cm^{-2} has been proposed for pre-combustion power cycles. Fluxes of this magnitude can be obtained for a 30 µm thick membrane dominated by electronic conductivity ($t_e \approx 1$) and the bulk proton conductivity of barium zirconate (≈ 0.02 S cm^{-1}). However, no single phase materials are close to such transport characteristics, and efforts are now devoted to develop dual phase composites comprising a proton conducting and an electronically conducting oxide. Such ceramic-ceramic composites should display increased chemical and thermal stability compared to the cermets discussed previously.

To investigate the potential of dual phase ceramic-ceramic membranes in further detail, we will first look into the equations that govern the mixed ambipolar conductivity in these systems. These were derived by Wu and Liu for randomly distributed composites comprising one ionic and one ionic conducting phase [79]. Based on their derivation, the mean proton conductivity of the dual phase composite ($\sigma_m^{\mathrm{H}^+}$) can be estimated as

$$\sigma_m^{\mathrm{H}^+} = \frac{E_1^{\mathrm{H}^+} + \sqrt{E_1^{\mathrm{H}^{+2}} + E_2^{\mathrm{H}^+}}}{4} \quad , \tag{6.12}$$

where

$$E_1^{\mathrm{H}^+} = 3\left(p_1\sigma_1^{\mathrm{H}^+} + p_2\sigma_2^{\mathrm{H}^+}\right) - \left(\sigma_1^{\mathrm{H}^+} + \sigma_2^{\mathrm{H}^+}\right), \tag{6.13}$$

$$E_2^{\mathrm{H}^+} = 8 \cdot \sigma_1^{\mathrm{H}^+} \cdot \sigma_2^{\mathrm{H}^+}. \tag{6.14}$$

Here, $\sigma_1^{\mathrm{H}^+}$ and $\sigma_2^{\mathrm{H}^+}$ are the proton conductivities of phase 1 and 2. p_1 and p_2 are the volume fractions of the same phases. In a similar manner, the mean electronic conductivity (σ_m^{e}) can be calculated as

$$\sigma_m^{\mathrm{e}} = \frac{E_1^{\mathrm{e}} + \sqrt{E_1^{\mathrm{e}2} + E_2^{\mathrm{e}}}}{4} \tag{6.15}$$

where

$$E_1^{\mathrm{e}} = 3(p_1\sigma_1^{\mathrm{e}} + p_2\sigma_2^{\mathrm{e}}) - (\sigma_1^{\mathrm{e}} + \sigma_2^{\mathrm{e}}), \tag{6.16}$$

$$E_2^{\mathrm{e}} = 8 \cdot \sigma_1^{\mathrm{e}} \cdot \sigma_2^{\mathrm{e}}. \tag{6.17}$$

On these bases, the ambipolar conductivity can be calculated for various partial conductivities and volume fractions of the two phases. For comparison, we shall look further into composites comprising either the pure proton conducting BCZY ($\sigma_{\mathrm{H}^+} \approx$ 0.02 S·cm^{-1}) or the mixed proton-electron conducting LWMO ($\sigma_{\mathrm{H}^+} \approx 0.002$ S·cm^{-1}) in combination with an electronically conducting oxide operating at 700 °C. Figure 6.6 presents calculated ambipolar conductivities as a function of the volume fraction of the electronically conducting phase in a matrix of BCZY (a) and LWMO (b) with varying degree of proton conductivity in the electronic phase. The atmosphere assumed for this calculation is 0.05 bar H_2, 0.025 bar H_2O and 0.925 bar Ar. Under these conditions, the electronic conductivity of BCZY is considered negligible, whereas the n-type conductivity of LWMO is ~0.002 S·cm^{-1}.

From Figure 6.6a we can recognize the threshold volume fraction for a percolating composite (p_2 = 0.3), where the ambipolar conductivity of the composite far exceeds the single phase conductivities. There is no significant effect of the proton conductivity in the electronic phase on the maximum ambipolar conductivity of the composite. It is evident from Figure 6.6a that an ambipolar conductivity of 0.01 S·cm^{-1} is theoretically attainable for composites of BCZY. On theses bases, composite ceramic-ceramic membranes may prove to be the solution for proton conducting membranes, provided that the electronic phase is chemically and mechanically compatible with BCZY.

In the case of LWMO composites (Figure 6.6b), the ambipolar conductivity is not significantly increased unless the proton conductivity of the electronic phase is comparable to that of LWMO. For lower proton conductivities the composite ambipolar conductivity remains similar that of LWMO up to the threshold volume fraction, due to the inherently high electronic conductivity of single phase LWMO. Thus, if the electronic phase provides faster surface kinetics or increased mechanical stability, the performance of a composite may still surpass single phase LWMO as the membrane thickness is decreased.

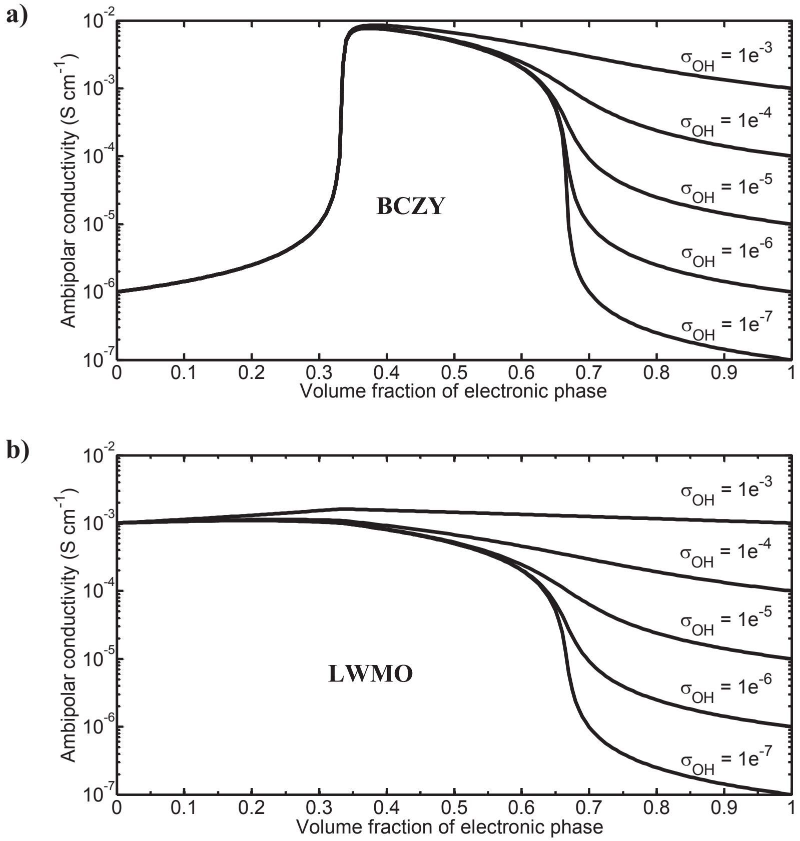

Figure 6.6 – Calculated ambipolar conductivities for composite membranes with BCZY (a) and LWMO (b) as a function of the volume fraction of the electronic phase. The lines represent various proton conductivities in the electronic phase, as indicated in the graph.

In the non-oxidative de-hydrogenation process described in Chapter 1.2, the target temperature is 600-700 °C with a minimum flux requirement of 0.1 mL·min^{-1}·cm^{-2} for a H_2 gradient of 0.1 bar. The permeability requirement for the hydrogen transport membrane is lower than for steam reforming, as the primary objective is to shift the equilibrium towards higher yields of aromatic products. If the hydrogen flux is too high, the equilibrium will shift towards coke formation on the membrane surface may occur. As the de-hydrogenation reaction is endothermic, additional heat must be provided to maintain energy balance through the system. This can be achieved by adding oxygen to the sweep gas, which will produce heat when it reacts with the hydrogen transported through the membrane. Thus, proton conducting oxides comprise the most promising alternative for this particular application due to their chemical stability towards both oxidizing and reducing atmospheres, intermediate hydrogen permeabilities and a less catalytically active surface towards coke formation compared to dense metal membranes. One may also envision that zeolite or MOF-based membranes could be beneficial for this application, as these membranes could act both as a catalyst for the de-hydrogenation reaction and as membranes for hydrogen extraction. However, the thermal and chemical stability of such membranes exposed to raw natural gas at 700 °C remains a challenge.

The preceding discussion elaborates that there is promise in the application of proton conducting membranes for hydrogen separation and natural gas processing. However, there are still many challenges and questions that remain unresolved. As evident for LWMo, oxide ion conductivity and hydrogen formation by water dissociation becomes increasingly prevalent at high temperatures when the sweep gas contains water vapour. The concept of hydrogen production by water dissociation and oxygen transport is not new, and Balachandran *et al.*[80, 81] reported quite large hydrogen production rates using both cermet and single phase oxygen transport membranes. The impact of oxide ion transport and water splitting on membrane performance depends on both the operating conditions and the primary task of the hydrogen transport membrane in the reactor.

In steam methane reforming using hydrogen transport membranes, the separated hydrogen gas is either stored or directly combusted to generate energy, while the captured CO_2 is safely sequestrated. Hence, additional formation of hydrogen in the sweep gas due to water splitting may yield higher production rates of hydrogen during operation, while also providing increased oxidation of carbon-species present in the feed gas stream. A recent study has also shown that oxide ion transport towards the feed side of a natural gas processing membrane reduces sulphur poisoning of the surface by oxidation of the sulphur species .

In the case of non-oxidative de-hydrogenation, the primary task of the membrane is to transport hydrogen from the reaction side to shift the equilibrium and increase the production yield of aromatics. Transport of oxide ions into the reaction chamber may, in this case, interrupt the non-oxidative reaction and oxidize the carbonaceous species, while the endothermic water splitting reaction will consume heat and alter the heat balance of the membrane reactor. Thus, in de-hydrogenation reactions, dry sweep gas should be used in order to minimize unwanted effects of oxide ion transport.

Finally, we should remember that proton conducting hydrogen transport membranes will be exposed to an electrochemical potential gradient at high temperatures in their applications. As discussed in Chapter 3.5, these gradients will in most cases induce a driving force for cation transport. Accordingly, cation diffusion induced kinetic instabilities such as demixing or decomposition may pose a serious risk for the durability of ceramic membranes. Moreover, there are additional degradation issues related to long term stability and cation diffusion. Typically these oxides are synthesized and sintered at temperatures well above the operating temperatures to ensure single phase compounds and dense membranes. For instance, large dopant concentrations are typically used to obtain high defect concentrations and conductivities. However, the dopant solubility at the operating temperature may be significantly lower than at the sintering temperature, effectively yielding a meta-stable composition. If such a phase is exposed to intermediate temperatures for a prolonged period, exsolution of the dopant may eventually deteriorate the membrane performance.

There are many reports in the literature regarding such phenomena for oxide ion conducting materials, but no reports on the cation diffusion properties of proton conducting oxides were available prior to the works presented in this thesis. Clearly, enhanced focus should be directed towards cation diffusion related degradation in order to verify the longevity of these membranes and the viability of proton conducting membranes as a competitive alternative for components in high temperature hydrogen technologies.

7. Conclusions

The present work presents investigations of the fundamental properties that govern the performance of the mixed proton electron conductor lanthanum tungsten oxide as a hydrogen transport membrane. A good proton conductor should exhibit high ambipolar proton-electron conductivity, high chemical, mechanical and redox stability, and high kinetic stability towards cation diffusion related degradation. Lanthanum tungsten oxide is a promising mixed proton conducting oxide with relatively high proton conductivity under wet conditions at intermediate temperatures (0.001 $S\cdot cm^{-1}$ at 600 °C) with proven chemical stability towards CO_2, and is therefore chosen as the model system for this work.

Hydrogen permeation by means of ambipolar proton-electron conductivity is significantly enhanced in Mo-substituted LWO compared to the nominally undoped oxide. Proton conductivity, with an activation energy of 50 $kJ\cdot mol^{-1}$, was identified as the rate limiting factor for ambipolar bulk transport of H_2. Hydrogen formed in the sweep gas due to water dissociation and oxide ion transport towards the feed side was found to contribute significantly to the level of hydrogen in the permeate above 750 °C under wet sweep conditions. Surface kinetics was identified as the limiting factor for hydrogen permeation in a 0.65 mm thick membrane, and was improved by coating the membrane surfaces with a catalytically active Pt layer. The reported hydrogen permeabilities for LWMO are higher than for state-of-the-art acceptor doped $SrCeO_3$, especially at temperatures below 800 °C, highlighting its potential as a hydrogen transport membrane. Mo-substitution in LWO was found to increase the n-type conductivity under reducing conditions without decreasing the proton conductivity significantly, evident from the increased hydrogen permeability as compared to the nominally pure LWO. Predicted fluxes based on a steady-state model using partial conductivities for LWMo are in good agreement with the measured hydrogen permeabilities, and confirmed that the hydrogen permeability in LWMo is above the target requirement for catalytic membrane reactors.

Bulk cation diffusivities in LWO, as determined by interdiffusion and chemical tracer diffusion studies, are similar in magnitude for both La and W site diffusion between 1000 °C and 1350 °C. A transport mechanism involving cation vacancies on the La2 sublattice is proposed. A change in activation energy from ~400 $kJ\cdot mol^{-1}$ above 1200 °C to ~250 $kJ\cdot mol^{-1}$ is attributed to frozen in defect concentrations at the lower temperatures. Enhanced diffusion of La along the grain boundaries, 10^{3}-10^{4} times faster than in bulk, may result in kinetic demixing or decomposition for a LWO membrane in an electrochemical potential gradient. At 900 °C, the cation diffusivities in LWO are in the order of 10^{-16} $cm^{2}\cdot s^{-1}$, resulting in an expected steady state demixing after 40 years, considerably longer than the proposed lifetime of proton conducting components in hydrogen technologies.

The present work also reveals that many complicating factors may influence the driving forces for mass transport in a mixed conducting membrane with an imposed chemical potential gradient. If a mixed proton, electron and oxide ion conductor is exposed to wet reducing feed gas and dry inert or dry oxidizing sweep gas, the resulting chemical potential gradients across the membrane will ultimately depend on both the imposed gradients and the transport parameters of the membrane itself. These effects make it increasingly difficult to interpret hydrogen permeation measurements for materials where the defect chemistry is not straightforward.

Mixed proton electron conducting oxides may serve as hydrogen transport membranes in applications where thermal integration, redox stability and cost are more important parameters than a high hydrogen flux. The contribution of water dissociation and oxide ion transport is positive in processes where hydrogen is the primary product and methane is oxidized to CO_2, and can prove beneficial in hydrogen production technologies.

Increased understanding of the reactions occurring at the membrane surfaces is necessary to further develop and describe the processes that limit hydrogen transport. The observation that hydrogen permeation through the rather thick LWMO membranes are limited by surface kinetics is surprising and in disagreement with surface exchange studies. Further work is therefore called upon to elucidate the discrepancy between the two experiments and to further our understanding of the elementary reactions that occur at the membrane surfaces. Moreover, as hydrogen based technologies are approaching commercialization, a complete set of predictive mathematical models that are easily integrated in present software is required to aid and assist in the design and analysis of future devices. These models require thermodynamic data input, currently not available for most proton conducting oxides. It should therefore be an aim to develop consistent sets of thermodynamic data for the most promising classes of proton conducting oxides to facilitate a complete description of the defect chemistry within the membrane materials. Better understanding and descriptions of the thermodynamic reactions may also allow for better implementation of composite systems that comprise compatible oxides in terms of chemical and mechanical stability. This could result in unprecedented hydrogen permeabilities for an all-oxide system if it were to succeed, and may be a promising next step in the development of ceramic hydrogen transport membranes.

References for Chapters 1-4 and 6

1. Brundtland, G.H., W.C.o. Environment, and Development, *Report of the World Commission on environment and development: "our common future."* 1987: United Nations.

2. Lu, G.Q., et al., *Inorganic membranes for hydrogen production and purification: A critical review and perspective.* Journal of Colloid and Interface Science, 2007. **314**(2): p. 589-603.

3. Hamakawa, S., et al., *Synthesis and hydrogen permeation properties of membranes based on dense SrCe0.95Yb0.05O3−α thin films.* Solid State Ionics, 2002. **148**(1–2): p. 71-81.

4. Li, L., R.W. Borry, and E. Iglesia, *Design and optimization of catalysts and membrane reactors for the non-oxidative conversion of methane.* Chemical Engineering Science, 2002. **57**(21): p. 4595-4604.

5. Tokyo-Gas. *On-site hydrogen production technology*. 2013; Available from: http://www.tokyo-gas.co.jp/techno/challenge/014_e.html.

6. Kjølseth, C.O., NO), Vestre, Per Christian (Jar, NO),, *PROTON CONDUCTING MEMBRANE*, 2012, PROTIA AS (Oslo, NO): United States.

7. Hamakawa, S., T. Hibino, and H. Iwahara, *Electrochemical Methane Coupling Using Protonic Conductors.* Journal of The Electrochemical Society, 1993. **140**(2): p. 459-462.

8. Hamakawa, S., T. Hibino, and H. Iwahara, *Electrochemical Hydrogen Permeation in a Proton‐Hole Mixed Conductor and Its Application to a Membrane Reactor.* Journal of The Electrochemical Society, 1994. **141**(7): p. 1720-1725.

9. McNaught, A.D. and A. Wilkinson, *{IUPAC}. Compendium of Chemical Terminology, 2nd ed. (the "Gold Book")*: Wiley-Blackwell; 2nd Revised edition edition.

10. Gallucci, F., et al., *Recent advances on membranes and membrane reactors for hydrogen production.* Chemical Engineering Science, 2013. **92**(0): p. 40-66.

11. Rao, M.B. and S. Sircar, *Nanoporous carbon membranes for separation of gas mixtures by selective surface flow.* Journal of Membrane Science, 1993. **85**(3): p. 253-264.

12. Bouwmeester, D.H.J.M. *Microporous ceramic membranes*. 2013 [cited 2013; Available from: http://www.utwente.nl/tnw/im/research/mcm.docx/.

13. Stahl, K. *Research Projects*. 2013; Available from: http://struktur.kemi.dtu.dk/kenny/research_projects.html.

14. Dong, J., Y.S. Lin, and W. Liu, *Multicomponent hydrogen/hydrocarbon separation by MFI-type zeolite membranes.* AIChE Journal, 2000. **46**(10): p. 1957-1966.

15. Gascon, J. and F. Kapteijn, *Metal-Organic Framework Membranes—High Potential, Bright Future?* Angewandte Chemie International Edition, 2010. **49**(9): p. 1530-1532.

16. Lewis, F.A., *The palladium hydrogen system*1967: Academic Press.

17. Edlund, D., et al., *Hydrogen-permeable metal membranes for high-temperature gas separations.* Gas separation & purification, 1994. **8**(3): p. 131-136.

18. Amandusson, H., L.-G. Ekedahl, and H. Dannetun, *The effect of CO and O< sub> 2</sub> on hydrogen permeation through a palladium membrane.* Applied surface science, 2000. **153**(4): p. 259-267.

19. Kamakoti, P. and D.S. Sholl, *A comparison of hydrogen diffusivities in Pd and CuPd alloys using density functional theory.* Journal of Membrane Science, 2003. **225**(1): p. 145-154.

20. Kamakoti, P. and D.S. Sholl, *Towards first principles-based identification of ternary alloys for hydrogen purification membranes.* Journal of Membrane Science, 2006. **279**(1): p. 94-99.

21. Sonwane, C.G., J. Wilcox, and Y.H. Ma, *Solubility of hydrogen in PdAg and PdAu binary alloys using density functional theory.* The Journal of Physical Chemistry B, 2006. **110**(48): p. 24549-24558.

22. Sonwane, C.G., J. Wilcox, and Y.H. Ma, *Achieving optimum hydrogen permeability in PdAg and PdAu alloys.* The Journal of chemical physics, 2006. **125**: p. 184714.

23. Ozdogan, E. and J. Wilcox, *Investigation of H2 and H2S adsorption on niobium-and copper-doped palladium surfaces.* The Journal of Physical Chemistry B, 2010. **114**(40): p. 12851-12858.

24. Netherlands, E.R.C.o.t. *Hydrogen Separation Module*. 2013; Available from: www.hysep.com.

25. Yogo, K., H. Takeyama, and K. Nagata, *Pore-fill-type Palladium–Porous Alumina Composite Membrane for Hydrogen Separation.* Energy Procedia, 2013. **37**(0): p. 1104-1108.

26. Roa, F., et al., *Palladium-copper and palladium-gold alloy composite membranes for hydrogen separations*, in *Inorganic membranes for energy and environmental applications*2009, Springer. p. 221-239.

27. Hatlevik, Ø., et al., *Palladium and palladium alloy membranes for hydrogen separation and production: History, fabrication strategies, and current performance.* Separation and Purification Technology, 2010. **73**(1): p. 59-64.

28. Norby, T. and R. Haugsrud, *Dense Ceramic Membranes*, in *Membranes for Energy Conversion*2008, Wiley-VCH Verlag GmbH & Co KgaA. p. 169.

29. Kreuer, K.D., *PROTON-CONDUCTING OXIDES.* Annual Review of Materials Research, 2003. **33**(1): p. 333-359.

30. Iwahara, H., et al., *High temperature type protonic conductor based on SrCeO3 and its application to the extraction of hydrogen gas.* Solid State Ionics, 1986. **18–19, Part 2**(0): p. 1003-1007.

31. S. J. Zhan, et al., *Preparation and hydrogen permeation of SrCe0.95Y0.05O3-delta asymmetrical membranes.* J. Membr. Science, 2009. **340**(1-2): p. 241-248.

32. Song, S.J., et al., *Numerical modeling of hydrogen permeation in chemical potential gradients.* Solid State Ionics, 2003. **164**(1–2): p. 107-116.

33. Song, S.J., et al., *Hydrogen permeability of SrCe1−xMxO3−δ (x=0.05, M=Eu, Sm).* Solid State Ionics, 2004. **167**(1–2): p. 99-105.

34. Shirsat, A.N., et al., *Thermodynamic stability of SrCeO3.* Journal of Solid State Chemistry, 2004. **177**(6): p. 2007-2013.

35. Okada, S., et al., *Chemical stability of SrCe0.95Yb0.05O3−α in hydrogen atmosphere at elevated temperatures.* Solid State Ionics, 2004. **175**(1–4): p. 593-596.

36. R. Haugsrud, *Defects and transport properties in Ln6WO12 (Ln = La, Nd, Gd, Er).* Solid State Ionics, 2007. **178**(7-10): p. 555-560.

37. R. Haugsrud and C. Kjølseth, *Effects of protons and acceptor substitution on the electrical conductivity of La6WO12.* J. Phys. Chem. Solids, 2008. **69**(7): p. 1758-1765.

38. Shimura, T., S. Fujimoto, and H. Iwahara, *Proton conduction in non-perovskite-type oxides at elevated temperatures.* Solid State Ionics, 2001. **143**(1): p. 117-123.

39. Escolástico, S., C. Solís, and J.M. Serra, *Hydrogen separation and stability study of ceramic membranes based on the system Nd5LnWO12.* International Journal of Hydrogen Energy, 2011. **36**(18): p. 11946-11954.

40. Escolástico, S., C. Solís, and J.M. Serra, *Study of hydrogen permeation in (La5/6Nd1/6)5.5WO12-δ membranes.* Solid State Ionics, 2012. **216**(0): p. 31-35.

41. Erdal, S., *Hydrogen in Oxides*, in *Department of Chemistry*2011, University of Oslo.

42. Amsif, M., et al., *Mo-Substituted Lanthanum Tungstate La28–yW4+yO54+δ: A Competitive Mixed Electron–Proton Conductor for Gas Separation Membrane Applications.* Chemistry of Materials, 2012. **24**(20): p. 3868-3877.

43. Magrasó, A., *Transport number measurements and fuel cell testing of undoped and Mo-substituted lanthanum tungstate.* Journal of Power Sources, 2013. **240**(0): p. 583-588.

44. Schmalzried, H. and W. Laqua, *Multicomponent oxides in oxygen potential gradients.* Oxid. Met., 1981. **15**(3): p. 339-353.

45. Martin, M., *Materials in thermodynamic potential gradients.* The Journal of Chemical Thermodynamics, 2003. **35**(8): p. 1291-1308.

46. Erdal, S., et al., *Defect Structure and its Nomenclature for Mixed Conducting Lanthanum Tungstates La28xW4+xO54+3x/2.* Int. J. Hydrogen Energy, 2012. **37**: p. 8051-8055.

47. Magraso, A., et al., *Complete structural model for lanthanum tungstate: a chemically stable high temperature proton conductor by means of intrinsic defects.* J. Mater. Chem., 2012. **22**(5): p. 1762-1764.

48. A. Magraso, et al., *New crystal structure and characterization of lanthanum tungstate "La6WO12" prepared by freeze-drying synthesis.* Dalton Trans., 2009(46): p. 10273-10283.

49. Maier, J., *Physical Chemistry of Ionic Materials: Ions and Electrons in Solids*2004: Wiley.

50. Darken, L.S., *Diffusion, mobility and their interrelation through free energy in binary metallic systems.* Trans. Aime, 1948. **175**(184): p. 41.

51. Schmalzried, H. and W. Laqua, *Multicomponent oxides in oxygen potential gradients.* Oxidation of Metals, 1981. **15**(3): p. 339-353.

52. Schmalzried, H., *Demixing, decomposition and degradation of oxides in chemical potential gradients.* Journal of the Chemical Society, Faraday Transactions, 1990. **86**(8): p. 1273-1280.

53. Martin, M., *Cation demixing in an oxygen ion conductor exposed to an oxygen potential gradient*, in *The Electrochemical Society Proceedings Series*, Pennington, Editor 1999. p. 308-316.

54. Martin, M., *Electrotransport and demixing in oxides.* Solid State Ionics, 2000. **136–137**(0): p. 331-337.

55. Čebašek, N., T. Norby, and Z. Li, *Kinetic Decomposition of a La2NiO4+δ Membrane under an Oxygen Potential Gradient.* Journal of The Electrochemical Society, 2012. **159**(8): p. F461-F467.

56. Martin, M. and H. Schmalzried, *Cobaltous Oxide in an Oxygen Potential Gradient: Morphological Stability of the Phase Boundaries.* Berichte der Bunsengesellschaft für physikalische Chemie, 1985. **89**(2): p. 124-130.

57. Krebs, H.-U., et al., *Pulsed Laser Deposition (PLD) -- A Versatile Thin Film Technique*, in *Advances in Solid State Physics*, B. Kramer, Editor 2003, Springer Berlin Heidelberg. p. 505-518.

58. Schneider, C. and T. Lippert, *Laser Ablation and Thin Film Deposition*, in *Laser Processing of Materials*, P. Schaaf, Editor 2010, Springer Berlin Heidelberg. p. 89-112.

59. De Souza, R.A., et al., *Determining oxygen isotope profiles in oxides with Time-of-Flight SIMS.* Solid State Ionics, 2005. **176**(15–16): p. 1465-1471.

60. Norby, T. and P.E.R. Kofstad, *Electrical Conductivity and Defect Structure of Y2O3 as a Function of Water Vapor Pressure.* Journal of the American Ceramic Society, 1984. **67**(12): p. 786-792.

61. Crank, J., *The mathematics of diffusion* 1979: Clarendon Press.

62. Mehrer, H., *Diffusion in Solids: Fundamentals, Methods, Materials, Diffusion-Controlled Processes*2007: Springer.

63. Holzapfel, C., *Fe-Mg interdiffusion at high pressures in mineral phases relevant for the Earth's mantle*, in *Mathematisch-Naturwissenschaftlichen Fakultät*2004, University of Cologne. p. 11.

64. Whipple, R.T., *Concentration contours in Grain Boundary Diffusion.* Philos. Mag. A, 1954. **45**: p. 1225-34.

65. Claire, A.D.L., *The analysis of grain boundary diffusion measurements.* British Journal of Applied Physics, 1963. **14**(6): p. 351.

66. Chung, Y.-C. and B.J. Wuensch, *An improved method, based on Whipple&#x2019;s exact solution, for obtaining accurate grain&#x2010;boundary diffusion coefficients from shallow solute concentration gradients.* Journal of Applied Physics, 1996. **79**(11): p. 8323-8329.

67. Escolástico, S., et al., *Hydrogen separation in La5.5WO11.25−δ membranes.* Journal of Membrane Science, 2013(0).

68. Escolastico, S., et al., *Enhanced H2 Separation through Mixed Proton–Electron Conducting Membranes Based on La5.5W0.8M0.2O11.25−δ.* ChemSusChem, 2013. **6**(8): p. 1523-1532.

69. Erdal, S., et al., *Defect structure and its nomenclature for mixed conducting lanthanum tungstates La28–xW4+xO54+3x/2.* Int. J. Hydrogen Energy, 2012. **37**(9): p. 8051-8055.

70. Hancke, R., Z. Li, and R. Haugsrud, *Hydrogen surface exchange on proton conducting oxides studied by gas phase analysis with mass spectrometry.* Journal of Membrane Science, 2013. **439**(0): p. 68-77.

71. Chen, P.-L. and I.W. Chen, *Role of Defect Interaction in Boundary Mobility and Cation Diffusivity of CeO2.* Journal of the American Ceramic Society, 1994. **77**(9): p. 2289-2297.

72. Ruh, R., et al., *The System Zirconia-Scandia.* Journal of the American Ceramic Society, 1977. **60**(9-10): p. 399-403.

73. Lei, Y., et al., *Segregation Effects at Grain Boundaries in Fluorite-Structured Ceramics.* Journal of the American Ceramic Society, 2002. **85**(9): p. 2359-2363.

74. Kilo, M., et al., *Cation self-diffusion of [sup 44]Ca, [sup 88]Y, and [sup 96]Zr in single-crystalline calcia- and yttria-doped zirconia.* Journal of Applied Physics, 2003. **94**(12): p. 7547-7552.

75. Kowalski, K., A. Bernasik, and A. Sadowski, *Bulk and grain boundary diffusion of titanium in yttria-stabilized zirconia.* Journal of the European Ceramic Society, 2000. **20**(7): p. 951-958.

76. Yoo, H.I. and M. Martin, *On the path-dependence of the open-cell voltage of a galvanic cell involving a ternary or multinary compound with multiple mobile ionic species under multiple chemical potential gradients.* Phys Chem Chem Phys, 2010. **12**(44): p. 14699-705.

77. Zuo, C., et al., *Effect of Zr-Doping on the Chemical Stability and Hydrogen Permeation of the Ni−BaCe0.8Y0.2O3-α Mixed Protonic−Electronic Conductor.* Chemistry of Materials, 2006. **18**(19): p. 4647-4650.

78. Zuo, C., et al., *Composite Ni–Ba(Zr0.1Ce0.7Y0.2)O3 membrane for hydrogen separation.* Journal of Power Sources, 2006. **159**(2): p. 1291-1295.

79. Wu, Z. and M. Liu, *Modelling of ambipolar transport properties of composite mixed ionic-electronic conductors.* Solid State Ionics, 1996. **93**(1–2): p. 65-84.

80. Balachandran, U., *Use of mixed conducting membranes to produce hydrogen by water dissociation.* International Journal of Hydrogen Energy, 2004. **29**(3): p. 291-296.

81. Balachandran, U., T. Lee, and S. Dorris, *Hydrogen production by water dissociation using mixed conducting dense ceramic membranes.* International Journal of Hydrogen Energy, 2007. **32**(4): p. 451-456.

Appendix

Modeling the Steady-State and Transient Response of Polarized and Non-Polarized Proton-Conducting Doped-Perovskite Membranes

Robert J. Kee, Huayang Zhu, Brett W. Hildenbrand, Einar Vøllestad,
Michael D. Sanders and Ryan P. O'Hayre

Journal of the Electrochemical Society, **160** (3) F290-F300 (2013)

Journal of The Electrochemical Society, **160** (3) F290-F300 (2013)
0013-4651/2013/160(3)/F290/11/$31.00 © The Electrochemical Society

Modeling the Steady-State and Transient Response of Polarized and Non-Polarized Proton-Conducting Doped-Perovskite Membranes

Robert J. Kee,[a,*,z] Huayang Zhu,[a] Brett W. Hildenbrand,[a] Einar Vøllestad,[b] Michael D. Sanders,[c,] and Ryan P. O'Hayre[c]**

[a]*Mechanical Engineering, Colorado School of Mines, Golden, Colorado 80401, USA*
[b]*Department of Chemistry, University of Oslo, Oslo, Norway*
[c]*Metallurgical and Materials Engineering, Colorado School of Mines, Golden, Colorado, USA*

This paper develops and demonstrates a model representing radial defect transport through proton-conducting ceramic membranes, such as might be used in shell-and-tube type membrane reactors. The model uses a Nernst–Planck–Poisson (NPP) formulation and is designed to represent both steady-state and transient responses within mixed-conducting membranes with multiple charge-carrying defects. The partial differential equations, representing defect and charge conservation, are solved computationally using the method-of-lines in a differential-algebraic setting. Several example problems are solved and discussed, illustrating important aspects of the model.
© 2013 The Electrochemical Society. [DOI: 10.1149/2.016304jes] All rights reserved.

Manuscript submitted December 6, 2012; revised manuscript received January 15, 2013. Published January 23, 2013.

Certain doped perovskite ceramics, such as yttrium-doped barium zirconates (BZY), barium cerates (BCY), and solid solutions thereof (BCZY), are proton conductors. Thus, they are potentially valuable for application as separation membranes and in membrane reactors.[1,2] The most natural thought is that these materials are hydrogen-selective permeable membranes. However, depending upon the gas compositions across the membrane, and possibly electrode polarization, the membranes can effectively transport H_2, H_2O, and O_2. It is important to recognize the distinction between hydrogen-permeable membranes (e.g., palladium) and proton-conducting membranes, which do not conduct H_2 directly. In the ceramic membranes, the apparent gas-phase fluxes of all species through the membrane depend upon the gas-phase composition at the membrane surfaces.

Figure 1 illustrates a shell and tube configuration in which a thin (order 10 microns) ceramic membrane is supported on a porous-ceramic tube. The subject of this paper is the development of a model that can predict the radial electrochemical defect transport through the membrane. The model also predicts the apparent gas-phase fluxes.

At elevated temperatures around 600 °C and above, most proton-conducting perovskites are in fact mixed ionic-electronic conductors (MIECs).[3–6] As such, multicomponent charged-defect transport of protons $\mathrm{OH}_\mathrm{O}^\bullet$, oxygen vacancies $\mathrm{V}_\mathrm{O}^{\bullet\bullet}$, electrons e', and/or electron holes $\mathrm{h}^\bullet$[4,3] is possible. To fully capture the transport of these multiple charged defects, this model formulates and solves coupled defect-conservation equations for all mobile charged species, with the defect fluxes being represented via the Nernst–Planck equations. At the membrane surfaces the defect reactions are assumed to be in equilibrium with the gas phase, thus establishing boundary conditions for the transport equations. Internal electric-potential gradients are formed within the membrane to maintain electroneutrality. Thus the defect fluxes depend upon both concentration gradients and the local electric fields. The membrane performance depends upon physical parameters, including defect mobilities and equilibrium constants for the gas-surface defect reactions. The steady-state system of governing equations forms an ordinary-differential-equation boundary-value problem that is solved computationally using finite-volume discretization. The mathematical structure is somewhat unusual because of the requirement to determine the internal electric fields.

An important objective of this paper is to describe algorithm design and computational implementation for mixed-conducting membranes with multiple charge-carrying defects. By implementing the model using computational mathematics tools in Matlab, we seek to make the approach broadly accessible, thus enabling wider application of models that are significantly more capable than the ones typically used (e.g., ambipolar diffusion models). The modeling capabilities are demonstrated using yttrium-doped barium zirconate as an example. The illustrative material properties are all reasonable and in concert with independent measurements. However, it is not the intent of this paper to establish physical properties for a particular material.

Although the present approach offers advantages compared to typical practice in the analysis and interpretation of mixed conduction in ceramics, the underpinning model does rely on significant assumptions. In principle, many of the assumptions can be relaxed. However, doing so requires the introduction of numerous physical parameters that are unknown. Thus, although the assumptions may cause some quantitative inaccuracies in model predictions, the basic model is expected to provide a very good overall picture of the relevant physical processes. Moreover, it provides a sound foundation on which to build more complex models as new knowledge and data becomes available.

Prior literature

There is much prior literature concerning the modeling of defect transport within mixed-conducting membranes. Many of the important contributions are concerned with biological systems, such as ion transport across cell boundaries. The Nernst–Planck–Poisson (NPP) problem was first implemented computationally by Cohen and Cooley.[7] In 1984 Buck published a review article discussing many aspects of the Nernst–Planck–Poisson model formulation. The NPP models are applied in modeling applications such as ion sensors.[8–10] Bazant and colleagues have contributed numerous papers concerning the underpinning electrochemical and mathematical theory, as well as analytic solutions under certain conditions (cf., 11–15).

In the ceramic membrane literature, the Nernst–Planck equation is generally used to represent defect transport fluxes, considering both diffusion (concentration gradients) and migration (electrostatic potential gradient). However, there are only a few examples of formulating and solving ceramic membrane problems in the context of solving the complete NPP equations. As an alternative to solving the Poisson equation, other approximations can be used to determine the spatial variations of electric potential. One approach is to enforce strict charge neutrality throughout the membrane. A closely related, but somewhat weaker approximation, is to assume that the local charge fluxes vanish. Yet another approach is to assume a uniform electrical field. Such approximations serve to effectively decouple the ionic and electronic transport.[16] The resulting simplified equations can sometimes be solved analytically,[17–21] or may be represented in the form of an equivalent circuit.[22,23] Another approach is to solve the problem

---

[*] Electrochemical Society Active Member.
[**] Electrochemical Society Student Member.
[z] E-mail: rjkee@mines.edu

Downloaded on 2013-08-19 to IP 129.240.152.19 address. Redistribution subject to ECS license or copyright; see ecsdl.org/site/terms_use

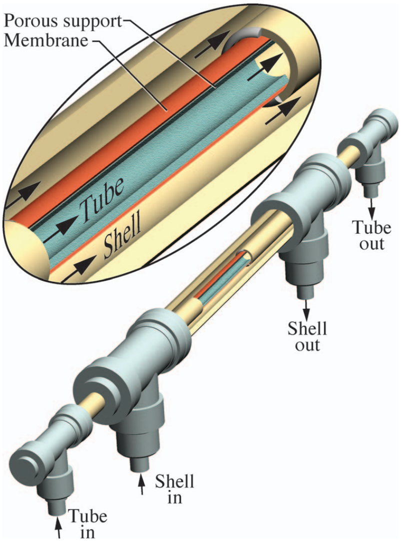

Figure 1. Cartoon representation of a shell and tube reactor with a thin membrane supported on the outside of a porous support tube.

approximately in an integral setting, thus not considering details of the defect and electrostatic-potential profiles within the membrane.[24]

For steady-state ceramic-membrane problems, the electrostatic potential gradient is usually established by assuming a zero net current through the membrane under open-circuit conditions.[25,26] In this case, the defect transport fluxes can be expressed approximately as functions of the defect concentration gradients alone. Considering two major defects ($OH_O^\bullet$ and $V_O^{\bullet\bullet}$ for the doped $BaCeO_3$), Kreuer, et al.[27] derived an expression of H_2O flux in terms of the H_2O concentration gradient and chemical diffusion coefficient, which is an explicit function of hydration degree and the self-diffusion coefficients of $OH_O^\bullet$ and $V_O^{\bullet\bullet}$. Virkar and Baek[28] presented an alternative form of H_2O chemical diffusion coefficient. Under the state-steady conditions, local thermodynamic equilibrium within the membrane is usually assumed, and the permeation rates of the defect and gaseous species through the membrane are obtained by averaging the local defect fluxes through the membrane, rather than directly solving defect conservation equations.[25,26] This approach is used widely in measuring defect equilibrium constants and transport coefficients.[29–33]

By formulating and solving the MIEC problem in the NPP framework, the present approach provides substantial advantages compared to the conventional practice in understanding charged-defect transport.c Solving in the differential-equation framework enables predictions of concentration and electrostatic-potential profiles within the membrane. Moreover, the transient problem can be solved, enabling the direct modeling of relaxation-type experiments. Integral approaches do not predict internal profiles and they are not useful in simulating transient behaviors. The present approach considers three or more charged defects, thus going beyond the commonly used ambipolar setting that is restricted to two charge carriers.

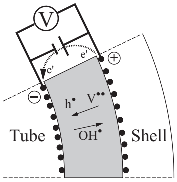

Figure 2. Schematic representation of a polarized membrane reactor with an external circuit.

Model configuration

Figure 2 is a schematic representation of the class of system that is to be modeled. For example, a feed-side tube may contain a high concentration of hydrogen, while a sweep gas on the shell side may be dominantly inert. Typical tube diameters are on the order of 10 mm. The mixed-conducting membranes are typically as thin as possible, say on the order of 10 μm. The very thin membranes must be supported, typically on a porous ceramic (not illustrated in Fig. 2). An external circuit can be used to change the electric field within the membrane. If the membrane is to be polarized, the porous support must be electrically conducting, which can be accomplished with a metal-ceramic composite. Mass transport through porous supports will cause concentration gradients, which is easily modeled as commonly done for anode-supported solid-oxide fuel cells. However, the present paper focuses entirely on the membrane itself with the gas-phase composition being specified at the membrane surface.

At steady state and open circuit there is no net current through the membrane or the external circuit. As illustrated in Fig. 2, protons $OH^\bullet$ are transported through the membrane toward the shell side, while electron holes $h^\bullet$ and oxygen vacancies $V^{\bullet\bullet}$ are transported from the shell toward the tube side. Different gas mixtures will result in different directions and magnitudes of the defect fluxes. To maintain electroneutrality, an internal electrostatic-potential profile Φ is established. Although such a system can transport protons across the membrane, the effective transport of hydrogen gas through the membrane can be negligible. For example, the hydrogen that is removed from the tube side may be only recovered as H_2O on the shell side if both sides of the membrane are operated under highly reducing conditions. Under such conditions, however, the driving force for proton transport is small with consequently small effective hydrogen-transport rates.

Defect transport rates can be increased greatly by polarizing the membrane with an external circuit. That is, an electric field can be imposed that greatly increases the migration transport of the protons through the membrane. As illustrated in Fig. 2, the shell-side electrostatic potential is decreased to below that of the tube-side electrostatic potential, driving the positively charged protons toward regions of lower electrostatic potential. By adding sufficient energy, the electrostatic field can dominate diffusive effects. The relevant electrochemical processes can be modeled by posing and solving the conservation equations for defects and charge.

Governing equations

Conservation equations are needed for the defect concentrations, with the Gauss law providing the relationship between charge density and electric potential. Neglecting direct defect-defect interactions (i.e., assuming dilute behavior), the defect fluxes can be expressed in Nernst–Planck form. The objective is to solve differential equations, yielding spatial and temporal variations of the defect and electrostatic potential profiles through the thickness of the membrane.

Defect conservation.— The spatial and temporal variations in defect concentrations are governed by conservation equations as

$$\frac{\partial [X_k]}{\partial t} + \nabla \cdot \mathbf{J}_k = 0, \qquad [1]$$

where $[X_k]$ are the defect concentrations and t is time. The molar fluxes of the defects may be represented in terms of species mobilities u_k and electrochemical-potential gradients $\nabla\tilde{\mu}_k$ as

$$\mathbf{J}_k = -u_k [X_k] \nabla \tilde{\mu}_k. \qquad [2]$$

Downloaded on 2013-08-19 to IP 129.240.152.19 address. Redistribution subject to ECS license or copyright; see ecsdl.org/site/terms_use

The Nernst–Einstein relationship

$$u_k = \frac{D_k}{RT} \qquad [3]$$

expresses mobilities in terms of diffusion coefficients D_k. The electrochemical-potentials $\tilde{\mu}_k$ are defined in terms of chemical potentials μ_k as

$$\tilde{\mu}_k = \mu_k + z_k F \Phi, \qquad [4]$$

where z_k are the charges associated with the defects, F is the Faraday constant, and Φ is the electrostatic potential. Assuming dilute mixtures,

$$\mu_k = \mu_k^\circ + RT \ln[X_k], \qquad [5]$$

were μ_k° are the standard-state chemical potentials.

The Nernst–Planck equation expresses the molar defect fluxes as

$$\mathbf{J}_k = -D_k \left(\nabla[X_k] + \frac{z_k F}{RT}[X_k]\nabla\Phi \right). \qquad [6]$$

The conservation equations (i.e., Eqs. 1) can be rewritten as

$$\frac{\partial[X_k]}{\partial t} = \nabla \cdot (D_k \nabla[X_k]) + \nabla \cdot \left(D_k \frac{z_k F}{RT}[X_k]\nabla\Phi \right). \qquad [7]$$

This equation is valid in the dilute limit, in which there are no direct defect-defect interactions (i.e., off-diagonal Onsager contributions are neglected). Both the diffusion and the migration contributions are evident in Eqs. 6 and 7.

The Nernst–Planck equation (Eq. 6) neglects defect-defect coupling. Such interactions can be included by formulating the defect fluxes as

$$\mathbf{J}_k = -\sum_{j=1}^{K} L_{kj} \nabla \tilde{\mu}_j, \qquad [8]$$

where the diagonal components of L_{kj} are directly related to the diffusion coefficients.[18,23] Especially with high doping levels, it is reasonable to anticipate some charged-defect interactions. However, the off-diagonal elements introduce numerous unknown and difficult-to-establish parameters. The diffusion coefficients are temperature-dependent, but independent of local composition. Moreover, the transport model takes no specific account of effects such as grain size and grain-boundary impedances.

Gauss law.— The electric field is related to the charge density ρ by the Gauss law as

$$\nabla \cdot (\varepsilon_r \varepsilon_o \nabla \Phi) = -\rho = -F \sum z_k [X_k], \qquad [9]$$

where ρ is the local charge density. The relative and vacuum permittivities are represented as ε_r and ε_o, respectively. In addition to the mobile charge carriers (e.g., $V^{\bullet\bullet}$, $OH^\bullet$, $h^\bullet$, e'), the concentrations of fixed charges (e.g., associated with the doping levels) must be included in the summation to evaluate the local charge density. Because the Gauss law does not include a time derivative, it plays the role of an algebraic constraint in the solution of the defect conservation equations (Eq. 7). The equations are tightly coupled, causing both the concentrations and the electrostatic potentials to vary spatially and temporally.

Nernst–Planck–Poisson model.— Together, Eqs. 7 and 9 form a complete system of governing equations, usually called a Nernst–Planck–Poisson (NPP) model. The independent variables are time t and the spatial coordinates (here, the radius r, spanning from the inner to the outer radii of the membrane $r_i \leq r \leq r_o$). The dependent variables are the defect concentrations $[X_k]$ and the electrostatic potential Φ. A solution requires boundary conditions, and the transient problem requires initial conditions. It is at least interesting to note that Φ does not appear in any time derivative. Although this presents no mathematical problem in principle, such a circumstance leads to formulating the computational mathematics as differential-algebraic equations. Computational algorithms and solutions are discussed later in this paper.

Initial and boundary conditions.— Both conservation equations (i.e., Eqs. 7 and 9) involve elliptic spatial operators. Thus, boundary conditions are required at r_i and r_o (i.e., at the interfaces with the tube and shell gases). For the problems considered here, the defect concentrations $[X_k]$ at the membrane surfaces are established by computing the local equilibrium between the gas composition and defect concentrations at the inside (tube-side) and outside (shell-side) membrane surfaces.

In addition to defect concentrations, boundary conditions associated with the electrostatic potentials are needed. At the tube side, a reference potential is set arbitrarily to $\Phi_t = 0$ V. At the shell side, a net charge-density flux is imposed in the context of the electrical current I through the external circuit. The current density i (i.e., the net current per shell-side surface area of the membrane) enters the membrane as

$$i = \sum_k z_k F J_k. \qquad [10]$$

As written in Eq. 10, a one-dimensional radial problem is implied. The electrical current from an external circuit is balanced by the current carried by charged defects within the membrane. Here J_k is understood to be the radial component of the defect-flux vector, evaluated at the boundary. At open-circuit, $i = 0$. Note that this boundary condition does not directly involve Φ. Again, although this presents no mathematical problem in principle, it is not the usual case in the computational solution of differential equations.

To solve transient problems, initial conditions are required for the radial profiles of the dependent variables, $[X_k]$ and Φ. For the examples shown later in this paper, initial conditions are established by the solution of a steady-state problem. For example, initial conditions could be those from the open-circuit solution. A transient problem would follow by imposing an electric current through the external circuit (e.g., Fig. 2).

Defect equilibrium at gas-surface interfaces.— In addition to chemical equilibrium, per se, evaluation of the defect concentrations at the membrane surface requires the consideration of charge neutrality and lattice site conservation. Charge neutrality requires that

$$2[V_O^{\bullet\bullet}]_L + [OH_O^\bullet]_L + [h^\bullet]_L - [e']_L - [Y'_{Ce,Zr}]_L = 0. \qquad [11]$$

Perovskite doping concentrations are typically in the range of 10%, in which case $[Y'_{Ce,Zr}]_L \approx 0.1$. The number of oxygen-ion sites in a pervoskite lattice (per formula unit) must be maintained as 3. Thus,

$$[V_O^{\bullet\bullet}]_L + [OH_O^\bullet]_L + [O_O^\times]_L = 3. \qquad [12]$$

In the foregoing expressions the nomenclature $[X_k]_L$ is used to indicate that the concentrations are evaluated at the lattice scale, not molar concentrations as in Eq. 7. The two concentration representations are related by the molar volume V_m of the lattice as

$$V_m = \frac{[X_k]_L}{[X_k]}. \qquad [13]$$

Molar volumes for perovskites, which represent the volume occupied by a single ABO_3 formula-unit of the perovskite lattice, are typically on the order of 5×10^{-5} m^3 mol^{-1}.

Stated in Kröger–Vink notation, the reactions of interest here are:[34,35,3,4]

$$\frac{1}{2}H_2 + O_O^\times \rightleftharpoons OH_O^\bullet + e' \qquad [14]$$

$$\frac{1}{2}O_2 + V_O^{\bullet\bullet} \rightleftharpoons O_O^\times + 2h^\bullet \qquad [15]$$

$$H_2O + V_O^{\bullet\bullet} + O_O^\times \rightleftharpoons 2OH_O^\bullet \qquad [16]$$

Downloaded on 2013-08-19 to IP 129.240.152.19 address. Redistribution subject to ECS license or copyright; see ecsdl.org/site/terms_use

$$\text{null} \rightleftharpoons \text{h}^{\bullet} + \text{e}' \qquad [17]$$

In general, equilibrium constants can be related to the change in Gibbs free energy $\Delta G = \Delta H - T\Delta S$ for the reaction as

$$K_p = \exp\left(-\frac{\Delta G}{RT}\right). \qquad [18]$$

Evaluating the equilibrium constants requires sufficient thermodynamic knowledge of the participating species to evaluate the enthalpies H, entropies S, and free energies G.

The equilibrium defect compositions and partial pressures of the reactions of interest here may be expressed as

$$K_{p,\text{H}_2} = \frac{[\text{OH}_\text{O}^{\bullet}]_\text{L}[\text{e}']_\text{L}}{[\text{O}_\text{O}^{\times}]_\text{L}\text{p}_{\text{H}_2}^{1/2}}, \qquad [19]$$

$$K_{p,\text{O}_2} = \frac{[\text{O}_\text{O}^{\times}]_\text{L}[\text{h}^{\bullet}]_\text{L}^2}{[\text{V}_\text{O}^{\bullet\bullet}]_\text{L}\text{p}_{\text{O}_2}^{1/2}}, \qquad [20]$$

$$K_{p,\text{H}_2\text{O}} = \frac{[\text{OH}_\text{O}^{\bullet}]_\text{L}^2}{[\text{O}_\text{O}^{\times}]_\text{L}[\text{V}_\text{O}^{\bullet\bullet}]_\text{L}\text{p}_{\text{H}_2\text{O}}}, \qquad [21]$$

$$K_{p,\text{eh}} = [\text{h}^{\bullet}]_\text{L}[\text{e}']_\text{L}. \qquad [22]$$

It should be noted that the four constant-pressure equilibrium constants K_p are not independent, but are related through the gas-phase equilibrium as

$$K_{p,\text{gas}} = \frac{K_{p,\text{O}_2}K_{p,\text{H}_2}^2}{K_{p,\text{H}_2\text{O}}K_{p,\text{eh}}^2} = \frac{p_{\text{H}_2\text{O}}}{p_{\text{H}_2}p_{\text{O}_2}^{1/2}}. \qquad [23]$$

The quantities appearing in the K_p expressions above are unit-less. The defect concentrations are evaluated on the lattice scale while the partial pressures are normalized by the standard-state pressure (atm/atm).

The equilibrium constants as expressed in Eqs. 19–23 assume ideal solutions and unity activity coefficients. In principle, this assumption is easily relaxed. However, as noted in the foregoing comments, a quantitative knowledge of the Henrian activity coefficients is needed. A further assumption is that the defect thermodynamic properties are independent of composition. The assumption can be reasonably challenged, but quantitatively establishing the non-ideal properties is a very difficult task.

Heterogeneous and charge-transfer kinetics.— As discussed in the previous section, the present model assumes equilibrium at the gas-membrane interfaces. Although certainly reasonable under some circumstances, this assumption is clearly not generally valid. In fact, heterogeneous kinetics can be rate-limiting in the adsorption and desorption of gas-phase compounds at the surface. Under polarized conditions, finite-rate charge-transfer kinetics (e.g., in Butler–Volmer form) can be rate limiting, contributing polarization losses that are significant compared to ion resistance within the membrane. Although the possibility of such kinetics is well recognized and practiced in related contexts,[36–38] the present paper is focused primarily on electrochemical transport behaviors within the membrane.

Electroneutrality.— The present models requires that the boundaries (i.e., interface between membrane and gas) be electrically neutral (i.e., Eq. 11). However, there is no direct imposition of electroneutrality within the membrane. Nevertheless, because the permittivity ε is very small, the Gauss equation (Eq. 9) effectively forces very-near charge neutrality. In other words, although $\rho \neq 0$, $\rho = F\sum z_k[X_k] \approx 0$, including during transients.

Open-circuit voltage.— The measurable open-circuit voltage (i.e., the electric-potential difference between the electrodes with no net current) can be evaluated as the difference in the electrochemical potentials $\tilde{\mu}$ of the electrons within the electrodes as[18,19]

$$E_\text{cell} = \phi_\text{c} - \phi_\text{a} = -\frac{\tilde{\mu}_\text{e}(\text{c}) - \tilde{\mu}_\text{e}(\text{a})}{F}. \qquad [24]$$

The nomenclature here uses "a" and "c" to represent anode (negative electrode) and cathode (positive electrode), respectively. Referring to Fig. 2, the tube side is the anode and the shell side is the cathode. Assuming perfect, reversible, contact between the electrodes and the mating surface of the membrane, the electrochemical potential of the electrons is the same in the electrode and the immediately adjacent membrane. In other words, assume that there is no potential difference across the electrode-membrane interface.

Within the membrane, the electron electrochemical potentials can be expressed as

$$\tilde{\mu}_\text{e} = \mu_\text{e}^{\circ} + RT\ln[\text{e}'] - F\Phi, \qquad [25]$$

were $[\text{e}']$ represents the electron concentration. Thus, the measurable open-circuit voltage (OCV) can be evaluated as

$$E_\text{cell} = (\Phi_\text{e,c} - \Phi_\text{e,a}) - \frac{RT}{F}\ln\frac{[\text{e}']_\text{e,c}}{[\text{e}']_\text{e,a}}. \qquad [26]$$

In this expression, the nomenclature "e,a" and "e,c" represent the variables within the membrane at the anode and cathode interfaces. The electrostatic potentials and the electron concentrations are evaluated from the model solutions.

Considering Eq. 17, it may also be noted that

$$\tilde{\mu}_\text{e} + \tilde{\mu}_\text{h} = 0. \qquad [27]$$

Thus, the OCV may also be represented in terms of the electrochemical potential of the holes as

$$E_\text{cell} = (\Phi_\text{e,c} - \Phi_\text{e,a}) + \frac{RT}{F}\ln\frac{[\text{h}^{\bullet}]_\text{e,c}}{[\text{h}^{\bullet}]_\text{e,a}}. \qquad [28]$$

It should be noted that the measurable OCV and the Nernst potential (reversible potential) are different. And, with a mixed-conducting membrane, the evaluation of a unique Nernst potential can be elusive. If the membrane were a pure oxygen-ion conductor (such as is typical for solid-oxide fuel cells) then

$$E_\text{Nernst} = \frac{RT}{4F}\ln\frac{p_{\text{O}_2,\text{c}}}{p_{\text{O}_2,\text{a}}}, \qquad [29]$$

where p_{O_2} represents the oxygen partial pressure. If on the other hand, the membrane were a pure proton conductor, then

$$E_\text{Nernst} = \frac{RT}{2F}\ln\frac{p_{\text{H}_2,\text{a}}}{p_{\text{H}_2,\text{c}}}, \qquad [30]$$

In general, these two measures of the reversible potential yield different voltages. It should also be noted that while the cell potential (Eq. 26) can be measured, the electrostatic potential difference within the membrane $(\Phi_\text{e,c} - \Phi_\text{e,a})$ is not measurable.

Charge flux.— The net flux of charge $\mathbf{J}^\text{c}$ depends upon the fluxes of the charge-carrying defects as

$$\mathbf{J}^\text{c} = \sum_k z_k F\mathbf{J}_k. \qquad [31]$$

At steady state, the net charge through the membrane is constant and balanced exactly by the current supplied by the external circuit. At open circuit, there is no net charge flux through the membrane. In radial coordinates, the flux changes through the membrane thickness because the areas through which the flux proceeds varies with the radius. However, for thin membranes and relatively large tube radius, the flux is very nearly constant at steady state. Under transient conditions, such as a sudden imposition of current on one boundary, the flux can vary spatially within the membrane.

Downloaded on 2013-08-19 to IP 129.240.152.19 address. Redistribution subject to ECS license or copyright; see ecsdl.org/site/terms_use

Table I. Charged-defect diffusion coefficients, $D_k = D_k^\circ \exp(E_k/RT)$.

	D_k° (m^2 s^{-1})	E_k (kJ mol^{-1})	D_k (650°C) (m^2 s^{-1})	D_k (850°C) (m^2 s^{-1})
$\mathrm{OH}_\mathrm{O}^\bullet$	1.55×10^{-8}	43.0	5.72×10^{-11}	1.55×10^{-10}
$\mathrm{V}_\mathrm{O}^{\bullet\bullet}$	1.90×10^{-9}	70.0	2.08×10^{-13}	1.05×10^{-12}
$\mathrm{h}^\bullet$	1.05×10^{-6}	97.0	3.41×10^{-12}	3.23×10^{-11}
e'	1.70×10^{-7}	90.0	1.37×10^{-12}	1.11×10^{-11}

Conductivity.— Although the foregoing conservation equations are formulated in terms of mobilities and diffusion coefficients, there are also good reasons to evaluate the conductivities. Individual defect conductivities are written as

$$\sigma_k = \frac{F^2}{RT} z_k^2 [X_k] D_k. \qquad [32]$$

The net conductivity is evaluated by a summation over the defect conductivities as

$$\sigma = \frac{F^2}{RT} \sum_{k=1}^{K} z_k^2 [X_k] D_k. \qquad [33]$$

Even in cases where the diffusion coefficients D_k are assumed to be constant, the conductivities cannot be considered to be constants. The conductivities depend upon the defect concentrations $[X_k]$, which can vary greatly and nonlinearly through the thickness of the membrane.

Material properties

It is evident from the foregoing analysis that material properties are needed before solving any particular problem. However, for the materials of interest relatively little data has been reported. Table I reports the defect diffusion coefficients that have been estimated for $\mathrm{BaZr_{0.8}Y_{0.2}O_{3-\delta}}$ (BZY20). Table II reports the values of ΔH° and ΔS° that are used to evaluate the defect-reaction equilibrium constants (Eq. 18). The doping concentration used in the present analysis is taken to be 19%, $[\mathrm{Y}'_\mathrm{Zr}]_\mathrm{L} = 0.19$, and the molar volume is taken to be $V_\mathrm{m} = 4.55 \times 10^{-5}$ m^3 mol^{-1}. The relative permittivity ε_r is not known precisely, but should be in the range of 10 to 100. In any case, the results here are essentially unaffected by the value. Appendix A provides a brief further discussion about materials properties.

Computational algorithm

The computational algorithm is generally in the class of method-of-lines, wherein the spatial operators are discretized on a mesh network and the resulting system is solved using high-level ordinary-differential-equation software.

Spatial discretization.— In one-dimensional radial coordinates (cf., Fig. 3),

$$\nabla \cdot \mathbf{J} = \frac{1}{r}\frac{d(rJ)}{dr} \approx \frac{1}{r_j}\frac{(r_{j+1/2}J_{j+1/2} - r_{j-1/2}J_{j-1/2})}{\Delta r}. \qquad [34]$$

Table II. Thermodynamics for surface defect reactions.

	ΔH° (kJ mol^{-1})	ΔS° (J mol^{-1} K^{-1})	K_p (750°C)
$\frac{1}{2}\mathrm{H_2} + \mathrm{O}_\mathrm{O}^\times = \mathrm{OH}_\mathrm{O}^\bullet + \mathrm{e}'$	164.35	−17.85	4.74×10^{-10}
$\frac{1}{2}\mathrm{O_2} + \mathrm{V}_\mathrm{O}^{\bullet\bullet} = \mathrm{O}_\mathrm{O}^\times + 2\mathrm{h}^\bullet$	−135.0	−130.0	1.26×10^{00}
$\mathrm{H_2O} + \mathrm{V}_\mathrm{O}^{\bullet\bullet} + \mathrm{O}_\mathrm{O}^\times = 2\mathrm{OH}_\mathrm{O}^\bullet$	−93.3	−113.2	7.09×10^{-02}
$\mathrm{null} = \mathrm{h}^\bullet + \mathrm{e}'$	266.2	0.0	2.55×10^{-14}
$\mathrm{H_2} + \frac{1}{2}\mathrm{O_2} = \mathrm{H_2O}$	−245.45	−52.51	6.13×10^{09}

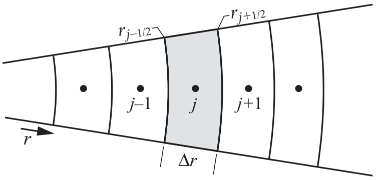

Figure 3. Illustration of a radial mesh. The shaded area represents a finite volume for cell j. The neighboring cells are represented as $j-1$ and $j+1$.

The diffusion and migration contributions to the defect fluxes (Eq. 7) can be discretized as, for example,

$$J_{j+1/2}^\mathrm{D} \approx -D_k \frac{[X_k]_{j+1} - [X_k]_j}{\Delta r}. \qquad [35]$$

The subscripts $j + 1/2$ and $j - 1/2$ indicates evaluation at the cell faces.

Migration upwinding.— As represented in Eq. 34, defect fluxes are evaluated at cell faces (i.e., $j + 1/2$ and $j - 1/2$). In the case of the diffusion fluxes (i.e., Eq. 35), the operator is straightforward. However, in the case of the migration flux,

$$\mathbf{J}_k^\mathrm{M} = -\left(\frac{z_k F}{RT} D_k \nabla\Phi\right)[X_k], \qquad [36]$$

there are alternatives for where to evaluate $[X_k]$. On physical grounds, the electrostatic-potential gradient (i.e., a vector) serves as a driving force to transport $[X_k]$ in a certain direction. There are computational benefits associated with evaluating $[X_k]$ in the sense of a convective derivative. In Eq. 36 the coefficient of $[X_k]$ takes the role of an artificial velocity. That is, in a one-dimensional radial setting, if $\nabla\Phi > 0$ and $z_k > 0$, then the migration flux is in the negative-r direction. In this case, the concentration is evaluated at $r_{j+1/2}$.

Boundary defect concentrations.— When considering only $\mathrm{H_2}$, $\mathrm{O_2}$, and $\mathrm{H_2O}$ as the active gas-phase species, the surface defect concentrations may be determined using a relatively straightforward iteration. Using the vacancy concentration $[\mathrm{V}_\mathrm{O}^{\bullet\bullet}]$ as the iteration variable, Eq. 21 can be rearranged as

$$[\mathrm{O}_\mathrm{O}^\times]_\mathrm{L} = \frac{1}{K_{p,\mathrm{H_2O}}\, p_\mathrm{H_2O}} \frac{[\mathrm{OH}_\mathrm{O}^\bullet]_\mathrm{L}^2}{[\mathrm{V}_\mathrm{O}^{\bullet\bullet}]_\mathrm{L}}. \qquad [37]$$

Based on the site constraint (Eq. 12), the following second-order quadratic equation can be solved analytically to represent $[\mathrm{OH}_\mathrm{O}^\bullet]_\mathrm{L}$ as a function of $[\mathrm{V}_\mathrm{O}^{\bullet\bullet}]_\mathrm{L}$,

$$\frac{1}{K_{p,\mathrm{H_2O}}\, p_\mathrm{H_2O}} \frac{[\mathrm{OH}_\mathrm{O}^\bullet]_\mathrm{L}^2}{[\mathrm{V}_\mathrm{O}^{\bullet\bullet}]_\mathrm{L}} + [\mathrm{OH}_\mathrm{O}^\bullet]_\mathrm{L} + [\mathrm{V}_\mathrm{O}^{\bullet\bullet}]_\mathrm{L} = 3. \qquad [38]$$

Because both $[\mathrm{OH}_\mathrm{O}^\bullet]_\mathrm{L}$ and $[\mathrm{O}_\mathrm{O}^\times]_\mathrm{L}$ have been already expressed as functions of $[\mathrm{V}_\mathrm{O}^{\bullet\bullet}]_\mathrm{L}$ (Eqs. 37 and 38), the hole and electron concentrations are represented indirectly as functions of $[\mathrm{V}_\mathrm{O}^{\bullet\bullet}]_\mathrm{L}$ by

$$[\mathrm{e}']_\mathrm{L} = \mathrm{K_{p,eh}} \mathrm{p}_\mathrm{H_2}^{1/2} \frac{[\mathrm{O}_\mathrm{O}^\times]_\mathrm{L}}{[\mathrm{OH}_\mathrm{O}^\bullet]_\mathrm{L}}, \qquad [39]$$

$$[\mathrm{h}^\bullet]_\mathrm{L} = \frac{K_{p,\mathrm{eh}}}{[\mathrm{e}']_\mathrm{L}}. \qquad [40]$$

With all the other defects being represented as functions of $[\mathrm{V}_\mathrm{O}^{\bullet\bullet}]_\mathrm{L}$, the overall charge neutrality constraint (Eq. 11) is a function of a single variable, $[\mathrm{V}_\mathrm{O}^{\bullet\bullet}]_\mathrm{L}$. Thus, given the gas-phase composition, the equilibrium surface defect concentrations can be evaluated by solving Eq. 11 iteratively for $[\mathrm{V}_\mathrm{O}^{\bullet\bullet}]_\mathrm{L}$. The defect boundary conditions for the conservation equations (Eq. 7) are converted to molar units as $[X_k] = [X_k]_\mathrm{L}/V_\mathrm{m}$.

Downloaded on 2013-08-19 to IP 129.240.152.19 address. Redistribution subject to ECS license or copyright; see ecsdl.org/site/terms_use

Computational solution.— When all the spatial terms are discretized, the ordinary-differential-equation system can be solved numerically. However, especially because of how the electric potential appears in the charge-conservation equation, the resulting system of equations cannot be solved in the so-called standard form $\mathbf{y}' = \mathbf{F}(t, \mathbf{y})$. Rather, the system is in the form of a system of differential-algebraic equations (DAE), $\mathbf{G}(t, \mathbf{y}, \mathbf{y}') = 0$.[39,40] In this format, every discretized equation is written in residual form and presented as a function to the DAE solution software. High-level software is available to solve such systems; the software used here is ode15i, which is part of the MATLAB package. This software is based upon the variable-step, variable-order, backward differentiation formulas, BDF.[39,40]

Equations 7 and 9 represent a transient problem. The equivalent steady-state problem uses the same spatial operators, but with $\partial/\partial t \equiv 0$. As with the transient problem, boundary condition are required. However, no initial conditions are needed. Once the spatial operators are discretized, the resulting computational problem is one of solving a system of nonlinear algebraic equations for the defect concentrations and electrostatic potentials at each of the discrete finite volumes. The present model solves the steady-state problem using the FSOLVE function in MATLAB, which implements a Levenberg-Marquardt algorithm.

Gas-phase fluxes.— Although the membrane model itself is concerned primarily with defect fluxes, it is the effective gas-phase fluxes that are of primary concern to applications such as separations and membrane reactors. Thus, it is important to establish the relationships between gas-phase and defect fluxes at the gas-membrane interfaces. The present model assumes that in the immediate proximity of the membrane surface, the gas phase is equilibrated. Thus, the gas-phase equilibrium composition can be different from that in the bulk gas flow, such as in the tube or sweep channels (e.g., Fig. 1). Generally speaking, as long as the gas-phase thermodynamic properties are available, the gas-phase equilibrium composition, represented as partial pressures $p_{\mathrm{eq},k}$, can always be evaluated from the bulk non-equilibrated gas-phase partial pressures p_k. For the mixtures of H_2, O_2, and H_2O considered here, the equilibrium composition is evaluated easily without software for a general free-energy minimization.

Qualitatively, it is known that H_2O production and consumption is the result of proton and oxygen-ion (vacancy) fluxes through the membrane. Water can be produced either from direct interactions among the defects or by reaction with the gas-phase environment. For example, a proton flux issuing into an oxidizing environment will likely produce water via reaction with O_2. Water can also be formed in an inert environment (e.g., Ar) via defect-defect reactions. Alternatively, water can be formed as oxygen ions issue into a reducing environment (i.e., negative vacancy flux). Gas-phase hydrogen can be produced by proton flux into an inert environment or a reducing environment. Similarly, gas-phase oxygen can be produced by vacancy production in an inert environment or an oxidizing environment. The reverse processes are also possible. The challenge is to develop quantitative measures to evaluate the gas-phase fluxes as functions of the defect fluxes and the gas-phase environments.

The algorithm for evaluating gas-phase fluxes is empirical, but is based upon physical considerations and respecting limiting behaviors. Only two defects, protons and oxygen vacancies, are directly responsible for mass transport. Electrons and holes significantly affect the transport processes and the defect chemistry, but do not directly transport mass. Charge neutrality at the membrane surface must be preserved (i.e., Eq. 11). Based on these considerations, the following expressions can be formulated to evaluate the gas-phase fluxes from the defect fluxes:

$$J_{\mathrm{H_2O}} = -J_{\mathrm{V}^{\bullet\bullet}} - \frac{1}{2} J_{\mathrm{h}^{\bullet}} \frac{p_{\mathrm{eq,O_2}}^{1/2}}{p_{\mathrm{eq,O_2}}^{1/2} + p_{\mathrm{eq,H_2}}}, \qquad [41]$$

$$J_{\mathrm{O_2}} = \frac{1}{4} J_{\mathrm{h}^{\bullet}} \frac{p_{\mathrm{eq,O_2}}^{1/2}}{p_{\mathrm{eq,O_2}}^{1/2} + p_{\mathrm{eq,H_2}}}, \qquad [42]$$

$$J_{\mathrm{H_2}} = -\frac{1}{2} J_{\mathrm{h}^{\bullet}} \frac{p_{\mathrm{eq,H_2}}}{p_{\mathrm{eq,O_2}}^{1/2} + p_{\mathrm{eq,H_2}}}. \qquad [43]$$

Further discussion and interpretation of Eqs. 41-43 may be found in Appendix B.

Examples and discussion

To illustrate the model performance, consider a 20 μm thick membrane, with an inner radius of 0.005 m (i.e., 1 cm diameter tube). Material properties are those for $BaZr_{0.8}Y_{0.2}O_{3-\delta}$ (BZY20) as detailed in Tables I and II. The results consider operation at atmospheric pressure and a nominal temperature of 750 °C. The initial examples are at open circuit. Then transient simulations are reported in which polarization is imposed using an external circuit that supplies current. The model predicts the transient response of the path between initial steady-state open-circuit behavior to a new steady-state behavior in the polarized condition.

Steady-state, open circuit, vary shell-side O_2.— Figure 4 illustrates a situation wherein the tube side gas is moist H_2 and the shell-side gas is dominantly Ar, with a trace of H_2O (10^{-6}) and varying levels of O_2 (10^{-5}, 10%, or 20%, respectively for the three cases presented). The flux charts show that in all three cases, protons transport through the membrane from the tube side to the shell side, with the proton flux

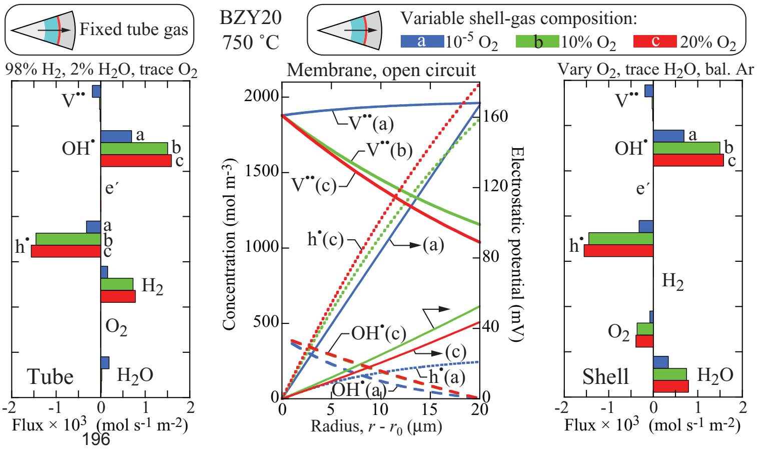

Figure 4. Composite representation of predictions with the bulk tube-side molar composition fixed at 98% H_2, 2% H_2O, and 10^{-6} O_2, but with varying O_2 on the shell side. The left-hand panel shows defect fluxes and gas-phase fluxes evaluated at the inner radius of the membrane (i.e., the tube side). A positive flux means radially outward. The center panel shows radial profiles of the defect concentrations and the electrostatic potential. The right-hand panel shows defect fluxes and gas-phase fluxes evaluated at the outer radius of the membrane (i.e., the shell side). The colors indicate the shell-side O_2 composition. The solid lines represent vacancy concentration, the short dashed lines represent hole concentration, and the long dashed lines represent proton concentration (the proton profiles for the 10% and 20% O_2 cases are overlapping). Additional solid lines, plotted with respect to the secondary y-axis, represent the electrostatic potential profile across the membrane.

Downloaded on 2013-08-19 to IP 129.240.152.19 address. Redistribution subject to ECS license or copyright; see ecsdl.org/site/terms_use

increasing as the O_2 level on the shell side increases. In all three cases, holes transport through the membrane from the shell side toward the tube side, again with the magnitude of the flux increasing as the shell-side O_2 increases. Under these conditions, the vacancy flux is from the shell side toward the tube side in all three cases, but with nearly negligible magnitude except at very low shell-side O_2 levels. Under all conditions considered in this paper, the electron concentrations and fluxes are negligible. Because the membrane is so thin compared to the tube radius (i.e., 20 μm versus 1 cm), the defect fluxes are nearly the same anywhere in the membrane. Thus, as illustrated in the left- and right-hand panels, the fluxes evaluated at the tube and shell surfaces are nearly indistinguishable—in other words, for the specific geometry considered here, a one-dimensional planar solution would provide nearly identical results as this radial solution.

The defect concentrations at the gas-membrane interfaces are determined via equilibrium with the gas environments. Thus, the tube-side defect boundary values are unaffected by the shell-side gas composition. The moist H_2 conditions lead to relatively high vacancy and proton concentrations on the tube side, but negligible hole concentrations. The O_2 concentrations on the shell side tend to fill oxygen vacancies, thus reducing the vacancy concentrations as the oxygen levels increase. As the shell-side O_2 increases, the hole concentrations increase greatly. The shell-side oxidizing environment renders the shell-side proton concentration to be negligible.

For all cases in Fig. 4 the internal electrostatic-potential gradients $\nabla\Phi$ are positive. At very low shell-side O_2 levels, the shell-side electrostatic potential is significantly higher (160 mV) than the tube-side. The electrostatic-potential difference between the shell-side and the tube-side *decreases* as the shell-side O_2 level increases. This occurs even though the Nernst Potential across the membrane (determined purely by the gas chemical potentials on the two sides of the membrane) *increases* as the shell-side O_2 level increases. This behavior is a result of the dramatic increase in the hole transport (and accompanying decrease in membrane resistance) enabled by the higher shell-side O_2 levels.

According to the Nernst–Planck relationship (cf., Eq. 6), defect fluxes are driven by both composition gradients (diffusion) and electrostatic-potential gradients (migration). Figure 4 shows that under most circumstances the direction of the defect fluxes are consistent with the diffusion (i.e., defects being transported down their respective concentration gradients). However, from the profiles in Fig. 4 alone, the migration contribution cannot be quantitatively discerned. In the case of holes, the diffusion and migration contributions are in the same direction and therefore combine additively. In the case of protons, diffusion and migration exert opposing forces. That is, migration tends to force the positively charged protons toward regions of lower electrostatic potential. Because the proton transport is toward the shell side, it is evident that diffusion is dominant over migration in the scenarios investigated here.

The vacancy transport shows evidence of so-called "uphill diffusion." At low shell-side O_2, both diffusion and migration contribute to vacancy transport from the shell side toward the tube side. However, as the shell-side O_2 concentration increases, the sign of the vacancy concentration gradient changes from positive to negative. In spite of this reversal, the direction of vacancy transport continues to be from shell side toward tube side (although the absolute magnitude of the vacancy flux is low). In other words, migration dominates over diffusion in these scenarios and the oxygen vacancies are transported up their concentration gradient. In mixed conductors with three or more charge-carrying defects, such "uphill" behavior can be expected.[41–43]

The apparent gas-phase fluxes reveal behaviors that at first may seem to be unusual. As is easily anticipated, a flux of gas-phase H_2 leaves the tube as protons are incorporated into the membrane. However, it is dominantly H_2O, not H_2, that appears to emerge from the membrane into the shell-side gas mixture. The protons arriving at the shell side react with oxygen, producing H_2O. As a consequence, there is an apparent flux of O_2 into the membrane on the shell side, representing the loss of O_2 by reaction with the protons to form H_2O. Because of this interplay between the defect fluxes and the gas-phase equilibria, one must be cautious not to make simple direct associations between defect fluxes and resulting gas-phase fluxes. Especially with mixed conductors, these behaviors potentially complicate the interpretation of membrane performance in the context of gas separations or membrane reactors.

Figure 4 shows an electrostatic potential difference of approximately 40 mV across the membrane, which is established to maintain charge neutrality. This electrostatic potential difference within the membrane should not be confused with the measurable open-circuit voltage. For the circumstances of the example in Fig. 4 (i.e., H_2 on the tube side and O_2 in the shell side), the open-circuit would be around 1.1 V. The Nernst potential is based upon the chemical potential associated with oxidizing the fuel. Interestingly, although the electrostatic potential difference of approximately 40 mV is physically present, it is not directly measurable. Only the electrode potentials are measurable (cf., Sect. 2.8).

Steady-state, open circuit, vary tube-side H_2O.— The results in Fig. 5 consider the tube-side gas to be dominantly H_2, but with varying low levels of H_2O. The shell-side gas is fixed as 10% O_2, 10^{-6} H_2O, and 90% Ar. As is the case in the previous example, protons and holes are the dominant charge carriers, with protons being transported toward the shell side and holes being transported toward the tube side.

As the H_2O level increases on the tube side, the sign of the electrostatic potential gradient changes. With essentially dry H_2 the shell-side

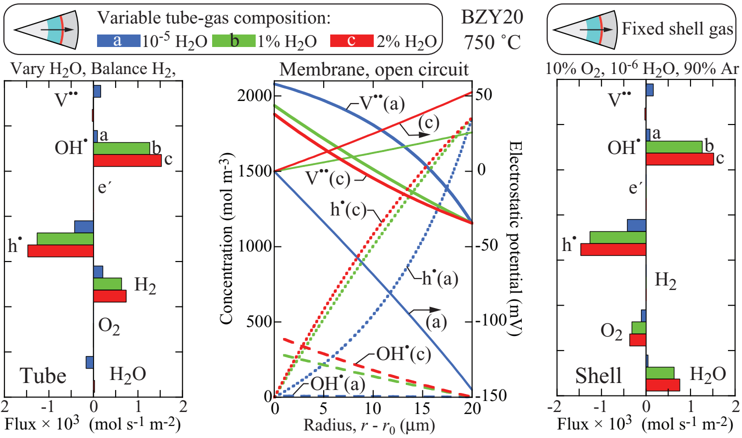

Figure 5. Composite representation of predictions with the tube side gas being dominantly H_2, but with varying H_2O levels. The shell-side molar composition is fixed at 10% O_2, 10^{-6} H_2O, and 90% Ar. See caption of Fig. 4 for more discussion about the three-panel layout.

Downloaded on 2013-08-19 to IP 129.240.152.19 address. Redistribution subject to ECS license or copyright; see ecsdl.org/site/terms_use

electrostatic potential is negative by approximately 150 mV relative to the tube-side reference potential. However, with the addition of only 1% H_2O to make moist H_2, the shell-side electrostatic potential reverses sign and becomes positive by approximately 25 mV relative to the tube-side reference potential and increases to approximately 50 mV positive for 2% H_2O. At low H_2O levels, the tube-side proton concentration is significantly suppressed. At the same time, the negative electrostatic-potential gradient at low H_2O levels significantly retards the hole flux. As a result, both the proton and hole fluxes are extremely low in this scenario and oxygen vacancies become an important component of the overall transport behavior. The significant oxygen vacancy transport at low H_2O levels results in the appearance of an appreciable water flux on the tube side of the membrane. With increasing H_2O levels in the tube-side H_2, the water production switches to the shell side. The proton flux from tube-side to shell-side increases significantly, even though the positive electrostatic-potential gradient that develops in these cases acts against the diffusive transport of the protons down their concentration gradient. For the holes, the positive electrostatic-potential gradient exerts a migration force that reinforces their diffusive transport toward the tube side. As is the case in the previous example, gas-phase H_2 leaves the tube side, but emerges into the oxidizing shell side as H_2O.

Steady-state, open circuit, vary temperature.— Figure 6 illustrates a situation in which the tube side gas is moist H_2 (2% H_2O) and the shell side gas is essentially dry Ar. Under these circumstances, there is vacancy and hole flux from the shell side toward the tube side, and proton flux from the tube side toward the shell side. The electrostatic-potential gradient is positive, with the shell side electrostatic potential predicted to be on the order of 200 mV above the tube-side reference potential. Migration assists the vacancy and hole transport, but opposes the proton transport. Both H_2 and H_2O leave the tube side gas, but the gas-phase flux into the shell side is dominantly in the form of H_2O. Qualitative behaviors are the same at all temperatures. The increasing mobilities of protons, oxygen vacancies, and holes with increasing temperatures leads to increasing fluxes of all three species. This occurs *despite* the fact that the proton, oxygen vacancy, and hole gradients all *decrease* as the temperature increases. An overall decrease in the proton concentrations and increase in the oxygen vacancy concentrations is observed with increasing temperature. This is an expected consequence of the dehydration experienced by proton conducting ceramics at higher temperatures (as driven by the negative entropy change associated with the Wagner hydration reaction depicted in Eq. 16). Interestingly, the hole concentrations also decrease with increasing temperature, a consequence of the reduction of the ceramic at higher temperatures as driven by the negative entropy change associated with the oxidation reaction depicted in Eq. 15.

Ambipolar interpretation of steady-state scenarios.— In almost every scenario investigated in the previous three sections, the internal electrostatic potential across the membrane sets up in such a way as to provide a boost to the hole transport but cause a drag on the proton transport. If transport in this system can be interpreted in terms of the classical limit of proton/hole ambipolar diffusion, this implies that the holes are the rate limiting species. In other words, for the membrane properties that we have chosen to simulate in these examples (where the parameters have been chosen to reflect the properties of BZY), protons and holes tend to determine the overall charge transport (with the oxygen vacancies typically playing only a minor role), and the product of the hole concentration times the hole mobility is smaller than the product of the proton concentration times the proton mobiliy. Under these conditions the internal electrostatic potential develops so as to accelerate the holes and decelerate the protons. Only the low H_2O scenario in Fig. 5 showed a different behavior, where the extremely dry gas environment led to very low proton concentrations, and hence protons rather than holes became the rate-limiting transport species. The conclusion that the holes are the rate-limiting species is reasonable for BZY, which is known as a relatively poor electronic (hole) conductor. However, the results of comparable case studies for an alternative MIEC membrane material could clearly be quite different. For example a material with higher hole conductivity could show proton-limited, rather than hole-limited transport behavior. Likewise, at higher temperatures and in drier conditions, oxygen vacancies could play a more meaningful role.

Transient simulation.— Consider a system that is initially operating in steady state at open-circuit conditions (i.e., no external current and no net current through the membrane). The operating temperature is 750 °C, the tube-side gas is fixed at 98% H_2, 2% H_2O, and 10^{-6} O_2, and the shell side gas is dominantly Ar with 10% O_2 (10^{-6} H_2O). With increasing the proton flux in mind, an external circuit is suddenly switched to provide a current density of 620 A m^{-2} to the shell side of the membrane. As illustrated in Fig. 7a, the external current achieves its new steady-state level in a fraction of a second. As the external current is applied, the shell-side electrostatic potential drops from around 50 mV above the tube side reference potential ($\Phi_t = 0$ V) to around 250 mV below the tube-side potential. The transient electrostatic potential reveals some interesting behaviors. The transient potential drops rapidly to a local minimum, then increases slightly. The initial undershoot is followed by a shallow local maximum, with a relatively slow decay toward a new steady state at around 60 s.

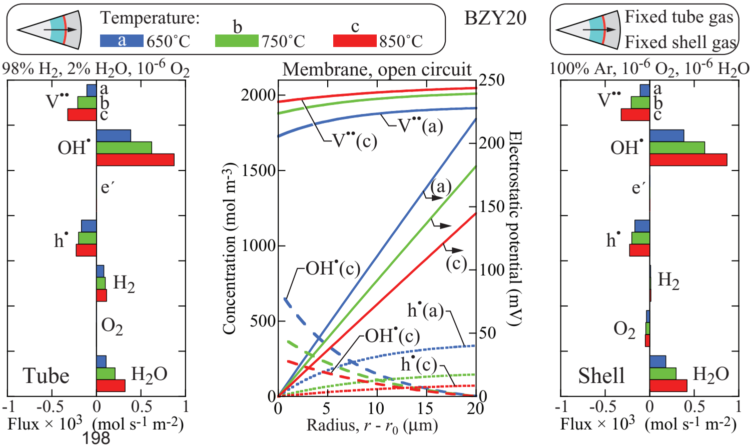

Figure 6. Composite representation of predictions with the tube side gas fixed as 98% H_2, 2% H_2O and 10^{-6} O_2. The shell-side molar composition is fixed as essentially pure Ar, with 10^{-6} O_2 and 10^{-6} H_2O. The three cases shown are for temperatures of 650 °C, 750 °C, 850 °C. See caption of Fig. 4 for more discussion about the three-panel layout.

Downloaded on 2013-08-19 to IP 129.240.152.19 address. Redistribution subject to ECS license or copyright; see ecsdl.org/site/terms_use

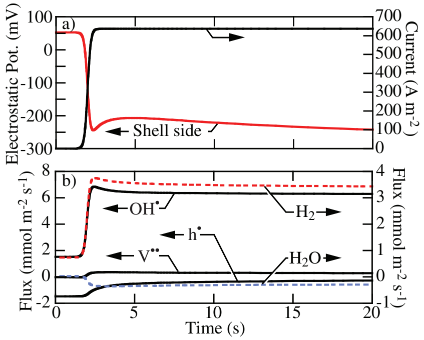

Figure 7. Transient profiles following the sudden polarization of a membrane. The tube-side gas is fixed at 98% H_2, 2% H_2O, and 10^{-6} O_2, and the shell-side gas is 10% O_2, 90% Ar, and 10^{-6} H_2O. Beginning with a steady-state solution at open circuit, an external circuit supplies current to the shell side of the membrane. (a) The top panel shows transient profiles of the electrostatic potential on the shell side of the membrane (relate to $\Phi = 0$ on the tube side) and the external current. (b) The lower panel shows transient profiles of defect and gas-phase fluxes evaluated on the tube-side gas-membrane interface.

Because of the large negative electrostatic-potential gradient under the polarized conditions, Fig. 7b shows that the proton flux is increased greatly by the increased migration contribution. The vacancy flux changes from slightly negative (i.e., toward the tube) to slightly positive (toward the shell). The hole flux remains negative, but with a slightly lower magnitude under the polarized conditions. The gas-phase H_2 flux leaving the tube through the membrane increases upon the high polarization conditions.

Figure 8 shows the tube- and shell-side fluxes as well as defect profiles at three times during the polarization transient. The first time is at the steady open-circuit operating conditions. The profiles at around $t = 2.3$ s correspond to the local minimum in the electrostatic potential transient (cf., Fig. 7). The results at around $t = 60$ s correspond to the near steady-state conditions under polarization. During the transient, the defect fluxes between the tube side and shell side can be very different, which is not the case in steady state. It is also interesting to note that hole flux on the shell side changes sign during the transient. These behaviors do not result in a departure from local electroneutrality during the transients.

It is clear that polarizing the membrane provides a means to greatly enhance migration, and hence greatly increase proton flux. The electrostatic-potential and flux profiles reveal relatively complex nonlinear phenomena during the transients. These behaviors are the result of the disparate mobilities of the charge-carrying defects in the mixed-conducting membrane.

Summary, conclusions, and future work

A new and very capable model has been developed and demonstrated. Although the model is capable of representing a wide range of mixed-conducting membranes, modeling particular systems requires material properties for defect mobilities and charge-transfer chemistry. Thus, there is a great need to measure properties, which will significantly improve the predictive value of the model.

The present model is based upon some important assumptions. As the model stands, the surface chemistry is assumed to be in equilibrium. At high temperatures and relatively low conductivities of the membrane, this assumption may be reasonable. However, it is certainly not assured for any particular membrane material and reactor design. Looking forward, there are significant benefits to formulating the surface chemistry in terms of finite-rate heterogeneous and charge-transfer chemical kinetics. Although the theory for doing so is reasonably clear, the actual reaction pathways and rate expressions are far from clear.[44–47]

The present model is implemented with hydrogen, oxygen, and steam in mind. However, most practical technology (e.g., membrane reactors) must be concerned with hydrocarbons and selective catalytic chemistry. Thus, as noted above, great benefits accrue by significantly extending the formulation and implementation of chemistry on the membrane surfaces. However, the defect transport within the membrane will remain essentially as it is currently implemented.

It is clear that polarizing the membrane can greatly increase defect fluxes, which may improve certain gas-separation or membrane reactor applications. However, because the ion conductivities for ceramic membranes are usually low, producing and maintaining the current through the external circuit comes with a cost. Models such as the present one can be applied to evaluate practical tradeoffs.

Acknowledgment

This research is supported by the Office of Naval Research via grant N00014-08-1-0539 and by the National Science Foundation MRSEC program under grant number DMR-0820518 at the Colorado School of Mines. We gratefully acknowledge numerous insightful discussions with Dr. Grover Coors (CoorsTek, Inc.). We also acknowledge close interactions with faculty and students in the Colorado Fuel Cell Center who are working on experimental aspects of the ceramic membrane development. These include Profs. Neal Sullivan and Sandrine Ricote,

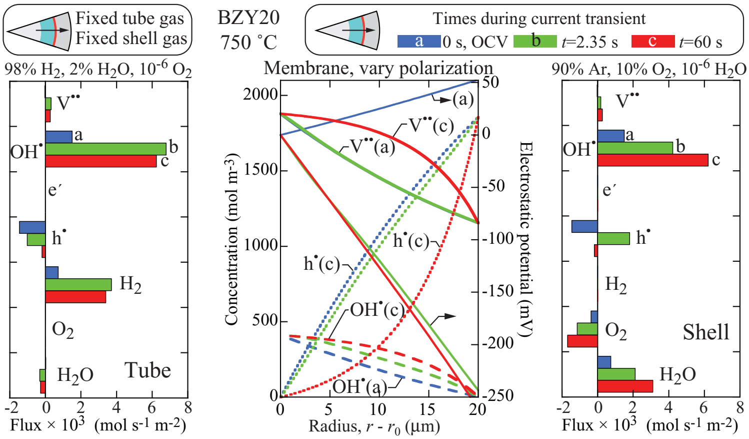

Figure 8. Performance predictions at three times during a transient example problem. The left-hand panel illustrates defect and gas fluxes at the tube boundary, the center panel shows spatial profiles of the defects and electrostatic-potentials, and the right-hand panel illustrates defect and gas fluxes at the shell boundary. The vacancy profiles at $t = 0$ s and $t = 2.35$ s are overlapping.

Downloaded on 2013-08-19 to IP 129.240.152.19 address. Redistribution subject to ECS license or copyright; see ecsdl.org/site/terms_use

and students Anthony Manerbino, Shay Robinson, Wade Rosensteel, and Sean Babiniec.

Appendix A

Material properties

Reported diffusion coefficients for the four charged defects are uncommon for proton-conducting ceramics, as are the defect-reaction thermodynamics (the exception being those for the Wagner hydration reaction). This necessitates a certain amount of interpretation of other measurements to formulate reasonable values.

The data contained in Table I originates in part from time-lag diffusivity experiments conducted in our laboratory, which enabled estimation of the proton, hole, and oxygen-vacancy diffusivities and activation energies for BZY20 from 750 °C to 1000 °C,[48] together with published defect diffusivities[49] and conductivities.[50] Further refinements to the diffusivity quantities were made using a previous iteration of the present model and experimental steady-state permeation flux results in order to ensure that observed trends in behavior were captured in the predictions. The diffusivity coefficients for electrons are estimated based on the hole diffusivity, however, their validity is unknown since there is almost no electron transport in barium zirconates under any conditions.

The sources of the thermodynamic quantities contained in Table II are more varied. The information for the formation of water from hydrogen and oxygen (Eq. 16) is ubiquitous, and, as mentioned above, the enthalpy and entropy of the Wagner hydration reaction (Eq. 16) is well studied.[49] None of the other reactions have been studied at length and there are no known reported values.

Conductivity activation energy is the sum of those for mobility and defect formation, so it should be possible to extract one of the component energies with knowledge of the other. Holes are known to behave as large polarons in similar perovskites,[51] so their mobility should have a weak temperature dependence and will likely contribute little to the overall conductivity activation energy. Therefore the activation energy for hole formation (Eq. 15) must be close to that of the observed activation energy for hole conductivity. Reported values for $\mathrm{BaZr_{0.93}Y_{0.07}O_{3-\delta}}$ and $\mathrm{BaCe_{0.9-\mathit{x}}Zr_{\mathit{x}}Y_{0.1}O_{3-\delta}}$ were taken as a starting point[52,53] and later refined to better reflect experimentally measured conductivity and permeation behavior of BZY20. The activation energy for electron/hole recombination (Eq. 17) was estimated by the calculated bandgap for BZY20.[54] Since the value of 5.3 eV is the optical bandgap rather than the conductivity bandgap[55] a lower value of 2.5 eV was originally chosen.[48] Later, the parameter was further increased to 2.75 eV. Finally, for the hydrogen and electron reaction (Eq. 14), since the given reactions are not independent, it was possible to take the four set values and calculate an enthalpy and entropy.

Appendix B

Gas-phase species fluxes

Equation 41 accommodates the fact that the flux of both oxygen vacancies and protons can contribute to gas-phase H_2O flux, $J_{\mathrm{H_2O}}$. The proton flux $J_{\mathrm{OH}_\mathrm{O}^{\bullet}}$ must be accompanied by a negative vacancy flux $-J_{\mathrm{V}_\mathrm{O}^{\bullet\bullet}}$ (i.e., a flux of oxygen) to directly produce a gas-phase H_2O flux by a defect-defect reaction. In other words,

$$J_{\mathrm{H_2O}}^{\mathrm{OH}_\mathrm{O}^{\bullet}} = -J_{\mathrm{V}_\mathrm{O}^{\bullet\bullet}}, \qquad [B1]$$

where the nomenclature $J_{\mathrm{H_2O}}^{\mathrm{OH}^{\bullet}}$ is used to indicate the H_2O flux that is specifically associated with protons. The flux of excess protons is the total proton flux minus the proton flux consumed by producing H_2O (i.e., Eq. B1). That is to say the flux of an as-yet-undetermined gas-phase species associated with excess protons can be expressed as

$$J_{?}^{\mathrm{OH}^{\bullet}} = J_{\mathrm{OH}_\mathrm{O}^{\bullet}} - 2J_{\mathrm{H_2O}}^{\mathrm{OH}_\mathrm{O}^{\bullet}}. \qquad [B2]$$

Substituting Eq. B1 into Eq. B2 yields

$$J_{?}^{\mathrm{OH}^{\bullet}} = J_{\mathrm{OH}_\mathrm{O}^{\bullet}} + 2J_{\mathrm{V}_\mathrm{O}^{\bullet\bullet}}, \qquad [B3]$$

which represents the flux of species other than H_2O that are associated with the proton flux. Continuing to assume an excess proton flux, $J_{\mathrm{OH}_\mathrm{O}^{\bullet}}$ represents the total proton flux and $2J_{\mathrm{V}_\mathrm{O}^{\bullet\bullet}}$ represents the vacancy flux that is consumed to produce the gas-phase water flux. Considering the preservation of charge neutrality (neglecting electrons, which are negligible for the materials considered here).

$$J_{\mathrm{OH}^{\bullet}} + 2J_{\mathrm{V}^{\bullet\bullet}} + J_{\mathrm{h}^{\bullet}} = 0, \qquad [B4]$$

the flux of excess protons (i.e., in excess of the flux that is used to form H_2O), can be written in terms of the hole flux as

$$J_{?}^{\mathrm{OH}^{\bullet}} = -J_{\mathrm{h}^{\bullet}}. \qquad [B5]$$

The gas-phase species that results from the excess proton flux depends upon the gas-phase environment. The strength of an oxidizing environment can be represented as

$$R_{\mathrm{ox}} = \frac{p_{\mathrm{O_2}}^{1/2}}{p_{\mathrm{O_2}}^{1/2} + p_{\mathrm{H_2}}}, \qquad [B6]$$

and the strength of a reducing environment can be represented as

$$R_{\mathrm{red}} = \frac{p_{\mathrm{H_2}}}{p_{\mathrm{O_2}}^{1/2} + p_{\mathrm{H_2}}}. \qquad [B7]$$

The net gas-phase H_2O flux must be the sum of the flux associated with the reaction of protons and oxygen vacancies and the contribution of excess protons reacting in an oxidizing environment, leading to

$$\begin{aligned} J_{\mathrm{H_2O}} &= J_{\mathrm{H_2O}}^{\mathrm{OH}_\mathrm{O}^{\bullet}} + \frac{1}{2} J_{?}^{\mathrm{OH}^{\bullet}} R_{\mathrm{ox}} \\ &= -J_{\mathrm{V}_\mathrm{O}^{\bullet\bullet}} - \frac{1}{2} J_{\mathrm{h}^{\bullet}} \frac{p_{\mathrm{O_2}}^{1/2}}{p_{\mathrm{O_2}}^{1/2} + p_{\mathrm{H_2}}}. \qquad [B8] \end{aligned}$$

For example, in a strongly reducing environment where no O_2 is available, the H_2O flux would depend entirely upon the negative of the vacancy flux (i.e, oxygen-ion flux). In a strongly oxidizing environment, the excess proton flux (i.e., as represented by the negative hole flux) contributes to producing additional H_2O. Gas-phase H_2O flux is proportional to the negative vacancy flux in any gas-phase environment. Of course, all the defect fluxes depend upon the gas-phase environments via boundary conditions for defect transport within the membrane.

Gas-phase oxygen can be produced by the reaction of holes with steam to strip hydrogen from water and form protonic defects (i.e., the sum of reactions 15 and 16) or oxygen can be consumed as the result of reaction with oxygen vacancies to form holes (i.e., reaction 15). Both of these processes can occur only in oxygen environments, and they depend exclusively on the production or consumption of holes. The oxygen flux follows as

$$J_{\mathrm{O_2}} = -\frac{1}{4} J_{?}^{\mathrm{OH}^{\bullet}} R_{\mathrm{ox}} = \frac{1}{4} J_{\mathrm{h}^{\bullet}} \frac{p_{\mathrm{O_2}}^{1/2}}{p_{\mathrm{O_2}}^{1/2} + p_{\mathrm{H_2}}}, \qquad [B9]$$

where R_{ox} measure the strength of the oxidizing environment.

Gas-phase hydrogen flux also depends upon the hole flux, but occurs only in reducing environments.

$$J_{\mathrm{H_2}} = \frac{1}{2} J_{?}^{\mathrm{OH}^{\bullet}} R_{\mathrm{red}} = -\frac{1}{2} J_{\mathrm{h}^{\bullet}} \frac{p_{\mathrm{H_2}}}{p_{\mathrm{O_2}}^{1/2} + p_{\mathrm{H_2}}}. \qquad [B10]$$

In reducing environments, hydrogen is formed from excess proton flux or the stripping of oxygen from water to fill oxygen vacancies.

References

1. L. Li and E. Iglesia, *Chem. Engr. Sci.*, **58**, 1977 (2007).
2. K. Li, *Ceramic membranes for separation and reaction*, Wiley, West Sussex, England, 2007.
3. M. Oishi, S. Akoshima, K. Yashiro, K. Sato, J. Mizusaki, and T. Kawada, *Solid State Ionics*, **179**, 2240 (2008).
4. M. Oishi, S. Akoshima, K. Yashiro, K. Sato, J. Mizusaki, and T. Kawada, *Solid State Ionics*, **180**, 127 (2009).
5. H.-I. Yoo, J.-K. Kim, and C.-E. Lee, *J. Electrochem. Soc.*, **156**, B66 (2009).
6. S. Ricote, N. Bonanos, H. J. Wang, and R. Haugsrud, *Solid State Ionics*, **185**, 11 (2011).
7. H. Cohen and J. W. Cooley, *Biophysical J.*, **5**, 145 (1965).
8. J. Bobacka, A. Ivaska, and A. Lewenstam, *Chem. Rev.*, **108**, 329 (2008).
9. J. J. Jasielec, T. Sokalski, R. Filipek, and A. Lewenstam, *Electrochimica Acta*, **55**, 6836 (2010).
10. B. Grysakowski, J. J. Jasielec, B. Wierzba, T. Sokalski, A. Lewenstam, and M. Danielewski, *J. Electroanalytical Chem.*, **662**, 143 (2011).
11. M. Z. Bazant, K. Thornton, and A. Ajdari, *Phys. Rev. E*, **70**, 021506 (2004).
12. M. Z. Bazant, K. T. Chu, and B. J. Bayly, *SIAM J. Appl. Math.*, **65**, 1463 (2005).
13. K. T. Chu and M. Z. Bazant, *Phys. Rev. E*, **74**, 011501 (2006).
14. P. M. Biesheuvel, M. van Soestbergen, and M. Z. Bazant, *Electrochimica Acta*, **54**, 4857 (2009).
15. L. H. Olesen, M. Z. Bazant, and H. Bruus, *Phys. Rev. E*, **82**, 011501 (2010).
16. Z. Chen, *J. Electrochem. Soc.*, **151**, A1576 (2004).
17. I. Riess, *J. Electrochem. Soc.*, **128**, 2077 (1981).
18. M. Liu, *J. Electrochem. Soc.*, **144**, 1813 (1997).
19. W. Lai and S. M. Haile, *Phys. Chem. Chem. Phys.*, **10**, 865 (2008).
20. S. Yuan and U. Pal, *J. Electrochem. Soc.*, **143**, 3214 (1996).
21. H. Näfe, *J. Electrochem. Soc.*, **144**, 3922 (1997).
22. M. Liu, *J. Electrochem. Soc.*, **145**, 142 (1998).
23. A. Virkar, *Int. J. Hydrogen Energy.*, **104**, 12609 (2004).
24. T. Norby and R. Haugsrud, Dense ceramic membranes for hydrogen separation. In A. F. Sammells and M. V. Mundschau, editors, *Nonporous inorganic membranes*, Wiley-VCH Verlag GmbH & Co., Weinheim, Germany, 2006.
25. T. Norby and Y. Larring, *Solid State Ionics*, **136-137**, 139 (2000).
26. Y. Liu, X. Tan, and K. Li, *Catal. Rev. Sci. Eng.*, **48**, 145 (2006).
27. K. D. Kreuer, E. Schönherr, and J. Maier, *Solid State Ionics*, **70-71**, 278 (1994).
28. A. V. Virkar and H. D. Baek, *J. Am. Ceram. Soc.*, **85**, 3059 (2002).
29. S. J. Song, E. D. Wachsman, S. E. Dorris, and U. Balachandran, *J. Electrochem. Soc.*, **156**, A790 (2003).

Downloaded on 2013-08-19 to IP 129.240.152.19 address. Redistribution subject to ECS license or copyright; see ecsdl.org/site/terms_use

30. S. J. Song, E. D. Wachsman, J. Rhodes, S. E. Dorris, and U. Balachandran, *Solid State Ionics*, **164**, 107 (2003).
31. M. Matsuka, R. D. Braddock, and I. E. Agranovski, *Solid State Ionics*, **178**, 1011 (2007).
32. M. Matsuka, R. D. Braddock, and I. E. Agranovski, *Math. Comput. Simul.*, **79**, 2713 (2009).
33. M. Matsuka, R. D. Braddock, H. Matsumoto, T. Sakai, I. E. Agranovski, and T. Ishihara, *Solid State Ionics*, **181**, 1328 (2010).
34. K. D. Kreuer, *Solid State Ionics*, **125**, 285 (1999).
35. K. D. Kreuer, *Annu. Rev. Mater. Res.*, **33**, 333 (2003).
36. D. G. Goodwin, H. Zhu, A. M. Colclasure, and R. J. Kee, *J. Electrochem. Soc.*, **156**, B1004 (2009).
37. C. J. Moyer, N. P. Sullivan, H. Zhu, and R. J. Kee, *J. Electrochem. Soc.*, **158**, B117 (2011).
38. A. M. Colclasure, K. A. Smith, and R. J. Kee, *Electrochimica Acta*, **58**, 33 (2011).
39. K. E. Brenan, S. L. Campbell, and L. R. Petzold, *Numerical solution of initial-value problems in differential algebraic equations*, SIAM, Philadelphia, PA, second edition, 1996.
40. U. M. Ascher and L. R. Petzold, *Computer methods for ordinary differential equations and differential-algebraic equations*, SIAM, Philadelphia, PA, 1998.
41. M. D. Sanders and R. P. O'Hayre, *J. Mater. Chem.*, **20**, 6271 (2010).
42. M. D. Sanders and R. P. O'Hayre, *J. Membrane Sci.*, **376**, 96 (2011).
43. A. Virkar, *Solid State Ionics*, **140**, 275 (2001).
44. W. C. Chueh and S. M. Haile, *Ann. Rev. Chem. Biomol. Eng.*, **3**(1), 313 (2012).
45. J. Fleig, *Phys. Chem. Chem. Phys.*, **7**, 2027 (2005).
46. R. A. DeSouza, *Phys. Chem. Chem. Phys.*, **8**, 890 (2006).
47. R. A. DeSouza, V. Metlenko, D. Park, and T. E. Weirich, *Phys. Rev. B*, **85**, 174109 (2012).
48. Michael Dale Sanders, Examining multi-species transport in BZY20 using water isotope permeation, Master's thesis, Colorado School of Mines, 2009.
49. K. D. Kreuer, St Adams, W. Münch, A. Fuchs, U. Klock, and J. Maier, *Solid State Ionics*, **145**(1-4), 295 (2001).
50. K. Nomura and H. Kageyama, *Solid State Ionics*, **178**(7-10), 661 (2007).
51. T. He, K. D. Kreuer, Yu. M. Baikov, and J. Maier, *Solid State Ionics*, **95**(3-4), 301 (1997).
52. W. Wang and A. V. Virkar, *J. Power Sources*, **142**(1-2), 1 (2005).
53. S. Ricote, N. Bonanos, and G. Caboche, *Solid State Ionics*, **180**(14-16), 990 (2009).
54. J. Robertson, Band offsets of wide-band-gap oxides and implications for future electronic devices, volume 18, pages 1785–1791, Raleigh, NC (USA), 2000. AVS.
55. T. Schober, W. Schilling, and H. Wenzl, *Solid State Ionics*, **86-88**, 653 (1996).

Downloaded on 2013-08-19 to IP **129.240.152.19** address. Redistribution subject to ECS license or copyright; see **ecsdl.org/site/terms_use**